Order Number 9417354

Human visual system modelling: Analysis of evoked potential dynamics

Hu, Zongqi, Ph.D.

New Jersey Institute of Technology, 1994

U·M·I
300 N. Zeeb Rd.
Ann Arbor, MI 48106

ABSTRACT

Human Visual System Modeling: Analysis of Evoked Potential Dynamics

by

Zongqi Hu

The visual evoked potential (VEP) reflects the electrical activity in the cerebral cortex due to visual stimulation. It contains information on signal processing in the visual pathways from the retina, through the lateral geniculate nucleus (LGN) to the cortical level. Although the VEP is generated by various sources in the multi-layer neural network, the functions of some neuronal mechanisms and the transfer characteristics of particular pathways can be revealed and analyzed by use of carefully designed stimuli (Zemon & Ratliff, 1984; Zemon, Victor & Ratliff, 1986). This dissertation focuses on studies of the visual evoked potential as a composite of neuronal activities such as direct-through excitation, local lateral inhibition and contrast gain control.

The work concentrates on the *sandwich model*, a three stage combination of linear-nonlinear-linear elements, introduced in 1970 by Spekreijse & Oosting, to represent signal flow in the visual pathways. Previous efforts to identify the three elements involved stimulation with contrast reversing spatial patterns using a two-sinusoid temporal signal (Spekreijse & Reits, 1982; Zemon & Ratliff, 1984; Zemon, Victor & Ratliff, 1986). Results of these studies are limited to amplitude and phase characteristics of the two linear elements in terms of sum and difference frequency components of the VEP.

In the current work, transfer functions were sought for the two linear elements in the original three-stage sandwich system in order to obtain an analytic description of the system. The goal was to represent the frequency responses, including those for sum and difference frequencies obtained from two-sinusoid stimulation, as well as transient responses elicited by step (square-wave) contrast reversals. Data from

ten normal subjects were analyzed. To fit the observed data collected from those subjects, it was found that the first linear element in the sandwich system must be a non-minimum phase function with zeros in the right half s-plane.

Based on prior investigations of single-cell responses in the cat retina (Shapley & Victor, 1978; 1981; Victor, 1981) and the VEPs in humans studied with a two-sinusoid contrast reversing pattern (Zemon, Victor & Ratliff, 1986; Zemon, Conte & Camisa, 1987), it appears that the amplitude-phase relation of the VEP frequency response to two-sinusoid stimulation depends on two inhibitory mechanisms, *contrast gain control* and *lateral interaction.* The phenomena of the inhibitory processes in the VEP were demonstrated in the current work by tests that included three-sinusoid stimulation, which enabled the investigation of direct-through excitatory and lateral inhibitory interactions simultaneously.

A new model has been proposed based on the sandwich system with emphasis on its physiological interpretation. This extended model incorporates contrast gain control and lateral inhibitory mechanisms in an inhibitory parallel path, which permits the analysis of separate excitatory and inhibitory processes. The effects of these inhibitory mechanisms are represented in terms of parameter control in the basic sandwich model. System identification procedures have been developed, and model parameter estimation and validation were performed for two individual subjects.

In the first modified model, the parameter control has been designed to represent steady-state operation. This model provides a good fit for the VEP frequency responses corresponding to the two-sinusoid and single sinusoid stimulation, but fails to represent the VEP transient response. Further modifications resulted in a second model incorporating dynamic parameter control. The second model provides a good fit for the VEP transient response; at the expense of somewhat poorer fit of the frequency responses.

HUMAN VISUAL SYSTEM MODELLING: ANALYSIS OF EVOKED POTENTIAL DYNAMICS

by
Zongqi Hu

A Dissertation
Submitted to the Faculty of
New Jersey Institute of Technology
in Partial Fulfillment of the Requirements for the Degree of
Doctor of Philosophy

Department of Electrical and Computer Engineering

January 1994

APPROVAL PAGE

Human Visual System Modeling:
Analysis of Evoked Potential Dynamics

Zongqi Hu

Dr. Andrew U. Meyer, Thesis Advisor Professor of Electrical and Computer Engineering, NJIT	Date
Dr. Vance Zemon, Co-Advisor Associate Professor of Ferkauf Graduate School of Psychology, Yeshiva University	Date
Dr. Rose A. Dios, Committee Member Associate Professor of Applied Mathematics, NJIT	Date
Dr. Peter Engler, Committee Member Associate Professor of Electrical and Computer Engineering, NJIT	Date
Dr. Edward Haupt, Committee Member Assistant Professor of Department of Ophthalmology, New Jersey Medical School, UMDNJ	Date
Dr. Stanley S. Reisman, Committee Member Associate Chair and Professor of Electrical and Computer Engineering, NJIT	Date

BIOGRAPHICAL SKETCH

Author: Zongqi Hu

Degree: Doctor of philosophy

Date: January 1994

Undergradute and Graduate Education:

- Doctor of Philosophy,
  New Jersey Institute of Technology, Newark, NJ, 1994
- Master of Science in Electrical Engineering,
  Shanghai University of Technology, Shanghai, China, 1986
- Diploma in Electrical Engineering,
  Shanghai United College of Shipbuilding Industry, Shanghai, China, 1982

Major: Electrical Engineering

Presentations and Publications:

[1] "Modeling of Human Visual System Dynamics Affecting the Visual Evoked Potential," *International Federation of Automatic Control, Symposium on Modeling and Control in Biomedical System*, March, 1994. Submitted.

[2] "Dynamic Model of Human Visual System Incorporating Excitatory and Inhibitory Processes: A VEP Study" *ARVO annual Conference*, May, 1994. Submitted.

[3] "Standard Sine-wave Generating Using Digital Method," *Electronics Technology, China.* October, 1986, 24–30.

This dissertation is dedicated to

my parents and Yumei

ACKNOWLEDGMENT

This work was the result cooperated with the Biophysics Laboratory, Rockefeller University. To all the people involved in this research, I want to express my gratitude for their friendly collaboration. In particular, I am deeply thankful to Prof. Andrew U. Meyer for his guidance of whole research project, and the dissertation writing with constant encouragement and friendly criticisms, to Dr. Vance Zemon who brought the basic idea of the project, as well as guidance of the work concerning neurophysiology and all the experimentation, to Dr. Edward Haupt for many important discussions and physiology expertise. to Dr. Rose Dios for her valuable suggestions on data statistical analysis.

I am specially indebted to the Biophysics Laboratory, Rockefeller University for providing the research environment and friendly assistance, to Eye Institute of New Jersey, UMDNJ for partially using the facilities, to NeuroScientific Corporation for their helpful information to use VENUS package and timely software modification. A special word of thanks should be also addressed to the people that anticipated in the experimentation with the results presented in the dissertation.

Furthermore, acknowledgement must be given to the committee members who provided useful comments for improvement of the dissertation.

Finally, I am most grateful to the Department of Electrical and Computer Engineering and Dr. Keith T. O'Brien in Industrial Engineering for their support in my academic years.

TABLE OF CONTENTS

TABLE OF CONTENTS
(Continued)

TABLE OF CONTENTS
(Continued)

LIST OF TABLES

LIST OF FIGURES

LIST OF FIGURES
(Continued)

LIST OF FIGURES
(Continued)

LIST OF ABBREVIATIONS

DFC—Difference frequency component

EEG—Electroencephalogram

LGN—Lateral geneculate nucleus

RMS—Root-mean squared value

SFC—Sum frequency component

VEP—Visual evoked potential

LIST OF SYMBOLS

(Including Page Number Where Introduced)

$L(t)$ ——— Stimulus luminance as a function of time (25)

L_m ——— Stimulus average luminance(25)

$s(t)$ ——— Temporal modulation signal used to describe stimulus luminance function (25)

C_w ——— Modulation depth of stimulus luminance (27)

f_1, f_2 ——— Frequency pair of two-sinusoidal stimulation (20)

$A_{\zeta DFC}$ ——— Amplitude of the second order difference frequency component in the signal $\zeta(t)$ (22)

$\varphi_{\zeta DFC}$ ——— Phase of the second order difference frequency component in the signal $\zeta(t)$ (22)

$A_{\zeta SFC}$ ——— Amplitude of the second order sum frequency component in the signal $\zeta(t)$ (22)

$\phi_{\zeta SFC}$ ——— Phase of the second order sum frequency component in the signal $\zeta(t)$ (22)

ΔT ——— Data sampling interval (28)

M ——— The number of record length contained in the entire test period (28)

N ——— The number of sampling points contained in one record length (28)

m ——— The number of repeated measurements (28)

$y_j(t)$ or $y_j(i\Delta T)$ ——— The jth measured evoked response (28)

$\overline{y}_j(t)$ or $\overline{y}_j(i\Delta T)$ ——— The jth averaged evoked response over M records (29)

$\overline{y}(t)$ or $\overline{y}(i\Delta T)$ ——— The mean response over m repeated measure of $\overline{y}_j(t)$ or $\overline{y}_j(i\Delta T)$ (29)

$e(t)$ ——— "True" evoked potential response (31)

$n_j(t)$ ——— noise in the jth evoked response (31)

$y(t)$ ——— "True" evoked response in one period due to periodic stimulation (132)

Y_j ——— A Fourier component in the jth evoked response (31)

LIST OF SYMBOLS
(Continued)

a_j ——— The real part of Y_j (29)

b_j ——— The imaginary part of Y_j (29)

Am_j ——— The amplitude of Y_j (30)

ψ_j ——— The phase of Y_j (230)

$\overline{Y}$ ——— The mean of a Fourier component Y_j (32)

$\overline{a}$ ——— The real part of $\overline{Y}$ (32)

$\overline{b}$ ——— The imaginary part of $\overline{Y}$ (32)

$\overline{Am}$ ——— The amplitude of $\overline{Y}$ (32)

$\overline{\psi}$ ——— The phase of $\overline{Y}$ (32)

Y ——— A "true" Fourier component in the evoked response (31)

a ——— The real part of Y (31)

b ——— The imaginary part of Y (31)

σ_a^2 ——— The variance of a_j (33)

σ_b^2 ——— The variance of b_j (33)

$Var(Y_j)$ ——— The variance of a Fourier component Y_j (33)

$Var(Y_j)_{est}$ ——— The estimate of the variance of a Fourier component Y_j (33)

$Var(\overline{Y})$ ——— The variance of the mean Fourier component $\overline{Y}$ (33)

$Var(\overline{Y})_{est}$ ——— The estimate of the variance of the mean Fourier component $\overline{Y}$ (34)

r_{circ} ——— The radius of *error circle*, defined as a root-mean squared value of $Var(\overline{Y})_{est}$ (34)

$\sigma_y(t)$ ——— Standard deviation of averaged evoked response $\overline{y}_j(t)$ (132)

$\varepsilon_y(t)$ ——— Expected error of the mean evoked response $\overline{y}(t)$ (132)

$\widehat{Y}$ ——— A Fourier component of model response (104)

R_n or R_N ——— Sum of residuals (104)

θ ——— Vector of the parameters in models (104)

W_i ——— Reliability weights assigned to the VEP data for curve fitting (106)

LIST OF SYMBOLS
(Continued)

W_A ——— Weight of frequency component amplitude (112)

W_ϕ ——— Weight of frequency component phase (112)

MS ——— Mean squared error (119)

df ——— Degrees of freedom (119)

CHAPTER 1
INTRODUCTION

Visual system research is one of the branches of neuroscience that involves studies of the electrical networks of the brain. The goal of this research is to learn about structure and function of the neuronal pathways in the brain, including its relation to learning and perception. One approach employed in visual system research is to examine the electric activity at different neural stages elicited by stimulation of the retina. The techniques used range from the microphysiological level, where the electric activity of a single neuron is recorded, to global level studies of electric activity from large populations of neurons recorded from the scalp, such as the electroencephalogram (EEG) or the visual evoked potential (VEP). The present study is concerned with the application of system analysis to characterize and model the primary visual pathway in humans that begins with photoreceptors in the retina of the eye and ends in the occipital cortex of the brain. The investigations are electrophysiological in nature and utilize the VEP as a noninvasive measure of cortical function.

1.1 Visual System: Anatomy and Physiology

The discussion of the visual system in this dissertation is limited to aspects directly related to our investigation. Well-documented reviews of the anatomy and physiology of the human visual system can be found in the basic visual literature, such as *Principles of Neural Science* by Kandel, Schwartz & Jessell (1991) and a standard text book *Adler's Physiology of the Eye* edited by Hart (1992).

1.1.1 Primary Visual Pathway

Basically, the primary visual pathway includes three stages, retina, lateral geniculate nucleus (LGN) and visual cortex (Figure 1.1). When a light image projects on the retina, it is converted to electrical activity by the photoreceptors (cones and rods) and mediated through the bipolar cells to the retinal ganglion cells. The axons of

the ganglion cells, totalling some 10^6 fibers, form the optic nerve, which transmit pulse-train signals to the visual cortex via the LGN. The total number of ganglion cells is about one hundredth lower than the total number of the receptors. On the average, one ganglion cell is connected to seven cones or to 320 rods, so that the initial set of signals must be compressed to a much smaller set prior to transmission via the optic nerves. The neural connections, however, are not homogeneous across the retina. The foveal area in the central retina, which is responsible for detailed form vision, has a $1:1$ or $1:2$ ratio of photoreceptors to bipolar and ganglion cells. This divergent connectivity is transformed into greater and greater convergence with increase in retinal eccentricity (in the present study, the foveal and parafoveal regions of retina are stimulated and therefore form the connections of interest).

The structure and processing properties of the retina have the effect of creating a discontinuous representation of the retina image by dividing it into small elements, which play a fundamental role in the perception of contrast and form.

The neural connections between each level are organized in a retinotopic fashion, that is, a given retinal point projects to a given region of the lateral geniculate, and then to a given region of the visual cortex. Even though the signals from many retinal photoreceptors may ultimately converge on a single ganglion cell, the signals from a single receptor may influence more than one ganglion cell, and the same principles of convergence and divergence apply to the connections at the geniculate and cortex, the principle of retinotopic organization is maintained in a general way.

1.1.2 Receptive Field Organization

One important feature of visual neurons is their *receptive field* property. A cell will only respond when visual stimuli appear in a particular part of the visual field. That part of the visual field that influences the firing of the neuron under study is called the cell's *receptive field.*

Kuffler (1952; 1953), recording from ganglion cells in the retina of the cat, discovered that the receptive field of the ganglion cells consists of a roughly circular

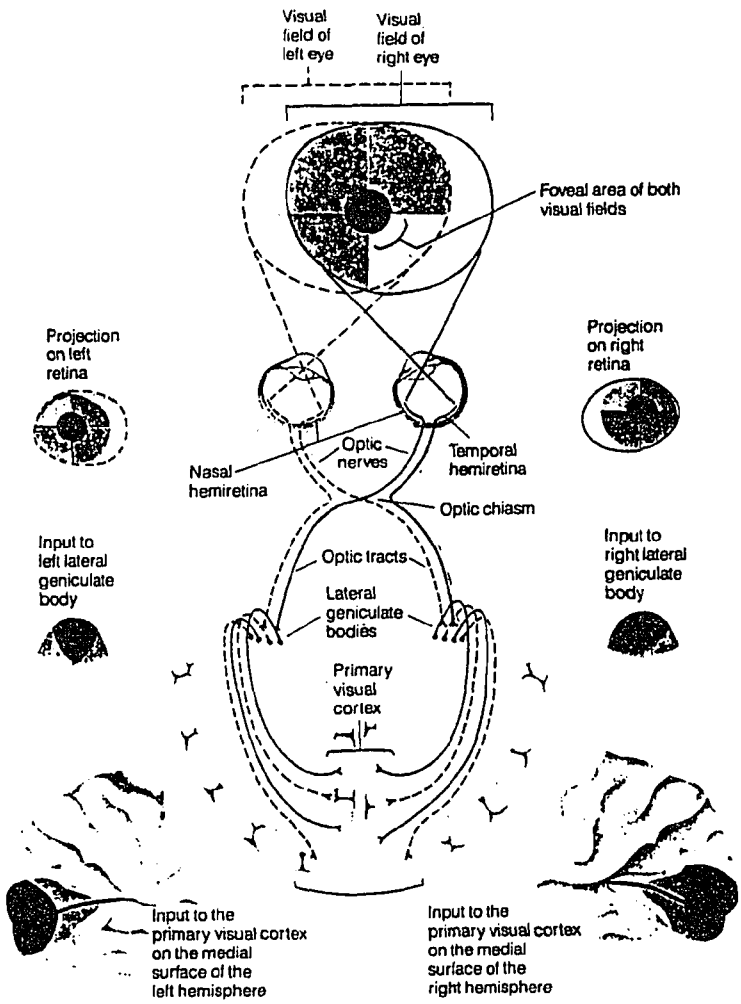

Figure 1.1 The primary visual pathway. (Adapted from Netter, F. H., "The Ciba Collection of Medical Illustrations," in *Nervous System*, Vol. 1, Ciba Pharmaceutical Products Co., Summit, N.J., 1953)

center, surrounded by a ring. A spot of light presented to the center field (center) produced a burst of unit activity. However, when the spot is moved to the surrounding field (surround), the cell ceases firing, but begins firing vigorously when the spot of light is turned off. The cells, responding in a center-on, surround-off manner, thus, are referred to as on-center cells. Another type of cell, responding in an antagonistic way, inhibition when the center is illuminated, and excitation when the surrounding field is illuminated, are called off-center cells. simultaneous representation of a stimulus to both center and surround of either type of the cell produces little or no response. These type of ganglion cells compare the brightness of the center spot with its surround, giving the greatest response when the contrast is maximal.

Enroth-Cugell and Robson (1966), studying the retina of the cat, found that not all retina ganglion cells show this cancellation effect. They classified those showing a null position (center + surround stimulation counterbalancing each other) as X cells, and those that did not as Y cells. The Y cell responds when either its receptive field stimulation is turned-on or turned-off. Further studies of the retina ganglion cells (Shapley, 1982) revealed that the X cell pathway is simple and involves linear summation of center and surround signals; The Y cell receives two inputs. One is a linear center-surround signal like that sent to the X cells. Another input to Y cells is the ensemble of excitatory subunits. The signals from those subunits have passed through a nonlinear process like a rectification, and thus form even order harmonics of the input frequency.

The lateral geniculate nucleus (LGN) on each side of the brain contains six layers of neurons. Each layer receives input from only one eye: layer 2, 3 and 5 from the ipsilateral eye, and layer 1, 4 and 6 from the contralateral eye. In the LGN, receptive fields are arranged in such a way that neighboring geniculate cells connect to the neighboring regions of the retina, so that the receptive fields of adjacent neurons overlap over most of their area. The concentric receptive fields of cells in LGN resemble those of ganglion cells in the retina, representing the types of X and Y (Kuffler & Nicholls, 1976).

The primary visual cortex consists of six principal layers (and several sublayers). arranged in bands parallel to the surface and separated by relatively cell-free zones containing primarily the dendritic and axonal processes of the cells. Axons from the lateral geniculate nucleus terminate for the most part on layer *IV*. The cortical cells, according to their receptive field property, are classified as *simple cells* and *complex cells* (Spitzer & Hochstein, 1985a; b). The simple cells have the same receptive field formation as that of the *X* ganglion cells, composed of a center and a surround. Complex cells have more than one subunit, and the receptive fields of these subunits overlap or scatter in the visual field.

1.1.3 Functional Pathways

In the visual system, neuronal connectivities can also be classified in terms of the functions they play. In addition to the "direct-through" pathways within the visual system, which transmit excitatory signals from one neural level to the next neural level, there exist lateral pathways (e.g. formed by horizontal cells in the retina), which transmit inhibitory signals within a neural level. It is also known that different types of cells and connections form separate (independent) parallel pathways that lead from the retina to the lateral geniculate nucleus of the thalamus (LGN), and then to the primary visual cortex in the occipital lobe of the brain (e.g. Shapley, 1990). One pair of parallel pathways, labeled "ON" and "OFF" based on their physiological properties, is thought to segregate brightness (positive-contrast) and darkness (negative-contrast) information respectively. Another pair of parallel pathways, labeled "magnocellular" and "parvocellular", process low and high contrast information differentially, as well as segregating other type of visual information (e.g. chromatic signals). This latter pair of pathways from the LGN is known to project to different layers of the visual cortex (Livingstone & Hubèl, 1988).

1.2 VEP: A Noninvasive Physiological Measure of Cortical Function

1.2.1 Electrogenesis and Features

In the cerebral cortex, one type of neuron, according to its dendritic (branch) arrangement, is called *stellate cells*, which can be further subdivided into those that have small spines arising from the dendrites and those that do not. The spiny stellate cells are restricted to cortical layer *IV* (Pearlman, 1975), which receives most of the lateral geniculate afferents, and project to pyramidal cells, located in layer *II, III, VI and VII* (Lund. 1973). The pyramidal cells have a cell body shaped something like a pyramid. The apex of the pyramid points toward the cortical surface; a single dendrite arises from it and is called the apical dendrite. Theoretical and empirical evidence has shown that the visual evoked potential (VEP), recorded at the cortical surface, mainly results from the sum of postsynaptic potentials occurring on apical dendrites of the pyramidal cells (Eccles, 1951; Purpura, 1959; Creutzfeldt & Kuhnt, 1973).

Although evoked potentials in humans have become accessible for about twenty years, the study of these brain phenomena was begun when it was discovered that a potential could be recorded on the occipital cortex in response to visual or electrical stimulation of the optic tract (Bartley & Bishop, 1933). After that discovery, significant progress in VEP research was achieved. This included the perfection of microelectrode recording from single cells in the cortex (cf. Purpura, 1959), a demonstration that the VEP can be recorded from man's scalp (Dawson, 1947), the adoption of statistical methods of signal analysis (Dawson, 1947, 1950) and the development of computer techniques to aid the recording and analysis of evoked potentials (e.g. Barlow, 1957).

Nowadays, the VEP is rapidly gaining an importance in neurophysiology, psychophysics and clinical neuro-ophthalmology, for the following reasons:

1. The visual evoked potentials (VEP) can be easily recorded from the scalp. It provides a noninvasive and risk-free means of investigating brain function.

2. The VEP contains information involving neuronal electrical activity in many functional structures and pharmacological pathways and may be capable of revealing a wide variety of neural abnormalities within the visual system. The VEP as a diagnostic tool has been discussed in a large number of publications (e.g. Cobb & Morocutti, 1967; Halliday, McDonald & Mushin, 1973; Asselman, Chadwick & Marsden, 1975; Myslobodsky, 1976; Bodis-Wollner & Onofrj, 1982; Ratliff & Zemon, 1984, Heckenlively & Arden, 1991).
3. There is a certain relation between the cortical surface potentials and the electric signals recorded from single cells. Like a newspaper photograph that is composed of a multitude of tiny dots, neural network activity is composed of the activities of whole populations of cells. Single-neuron recording reflects a view from a close range where we can see a few dots at any one time but cannot see the overall picture, while the evoked potential viewpoint is rather distant so that important features of the picture blur and merge. A judicious use of both techniques, therefore, might guide us towards the "correct distance" to view the brain's function (perception of shape, movement, direction, etc.) (Regan, 1989).
4. VEP responses measured under given test conditions are statistically reproducible (Elul, 1969; Regan, 1989).

1.2.2 Transient and Steady-State Responses

VEPs under study are classified as transient response and steady-state response. In both cases, periodic stimuli are applied.

For the transient VEP, the period between consecutive stimuli is sufficiently large so that the visual system returns its initial state before the next stimulus occurs. For example, low frequency equare-wave stimulation is used to obtain the VEP step response.

The steady-state VEP is measured at several stimulus frequencies. Here, the response to one stimulus has not died away before the next stimulus is delivered. The minimum stimulation rate for steady-state is usually that for which appreciable

overlap occurs between the response to one stimulus and the occurrence of the next stimulus.

A transient evoked potential is usually represented as a graph of voltage versus time. The evoked potential is commonly invisible in recordings taken directly from the scalp (i.e. the signal is buried in noise). The signal to noise ratio can be increased by breaking the response into several records in terms of the stimulation period, and then averaging the records to form an improved transient response.

Analysis of the transient response is commonly aimed at decomposing the waveform into elementary constituents of "components" in the hope that different components will indicate the activities of different functional subunits within the brain. For example, excitatory postsynaptic potentials occurring on apical dendrites near the cortical surface generate a superficial current sink and a corresponding deep current source, thus producing surface negativity. Inhibitory postsynaptic potentials occurring at similar sites generate a superficial source and corresponding deep sink, producing surface positivity (Eccles, 1951; Purpura, 1959; Creutzfeldt & Kuhnt, 1973).

The steady-state VEP is usually represented in terms of its frequency spectrum which includes information about transmission properties of visual neural pathways.

1.2.3 Nonlinear Properties

The visual pathways commonly show several types of temporal nonlinear behaviors. Two examples are: i) When successive responses run into each other, they may not sum linearly (Regan, 1982). In particular, the magnitude of the VEP does not increase as linearly with the stimulus contrast (Shapley & Victor, 1978; 1980). This nonlinear process is referred to as *contrast gain control* which will be discussed in Chapter 4. ii) For periodical stimulation, VEP response contains multi-harmonics and intermodulation components of the input frequencies (Spekreijse & Reits, 1982; Zemon, Conte, Jindra & Camisa, 1985). This type of nonlinear process, which can be modeled in terms of rectification, will be discussed in Chapter 2 and 3. The VEP modeling developed in this dissertation includes those two types of nonlinear mech-

anisms, as well as another nonlinear process, lateral interaction, to be discussed in Chapter 4.

1.3 Visual System Analysis and Modeling

Knowledge of the visual system (observation, structure, function, hypotheses, etc) can be linked together into a pattern–a mathematical model, which serves as a tool to quantitatively describe and predict the system spatial and/or temporal dynamics. Research in this area covers single cell unit (e.g. retina ganglion cells), as well as large populations of neurons (e.g. electroretinogram or evoked potential).

Single cell models closely related to the present study have been introduced in previous studies for: X type ganglion cell (Victor, 1987), Y type ganglion cell (Victor, 1988), cortical simple and complex cells (Spitzer & Hochstein, 1985b). These models, which provide insight onto the spatial and temporal properties of the cell units that constitute the visual pathways, will be discussed in the later chapters.

Early work on VEP modeling was done by Lopes Da Silva (1970), who collected a large amount of data from dogs and presented a model in his Ph.D. dissertation to characterize the dynamics of visual evoked potentials. He used sinusoidally modulated light as the stimulus and the fundamental component of the corresponding VEP response as the output to describe a linear model. That work did not consider the generation of harmonics, especially even harmonics, predominant in the VEP caused by periodic stimuli.

Spekreijse and Oosting proposed a three-stage model in 1970 for analyzing nerve sensory pathways. That model, shown in Figure 1.2, contains a static nonlinearity $N(v)$ sandwiched by two linear elements H_1 and H_2, which presents perhaps the simplest form among combinations of linear and nonlinear elements to present the nonlinear phenomena of the VEP. The existence of the nonlinear process in the model is supported by the fact that harmonic components can be found in the VEP responses elicited by the periodical stimulation. This generation of VEP harmonics has been found to be frequency-independent (Spekreijse, 1966), and can be characterized as a

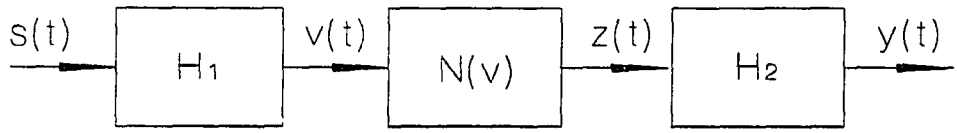

Figure 1.2 A sandwich model, two linear processes H_1 and H_2 are separated by a static nonlinearity N.

static nonlinearity in the form of a rectifier (the reasoning for this rectification model is discussed in the next Section).

In 1982, methods for identifying the sandwich model, including a two-sinusoid procedure to be used in the current research, were described by Spekreijse and Reits.

In 1984, Zemon analyzed direct-through excitation and lateral inhibition processes in the VEP using a contrast reversing spatial pattern stimulation. Based on the sandwich model, he explained those two distinct processes in terms of the observations. In 1985, Zemon and his co-workers (Zemon, Conte, Jindra & Camisa, 1985) provided physiological explanations for each element in the sandwich model based on microphysiological knowledge involving the pathways involved in the generation of the VEP.

1.4 Physiological Basis of Sandwich Model for the Visual Pathway

As shown in Figure 1.3, The path for VEP generation basically consist of three stages, retina, lateral geniculate nucleus (LGN) and cerebral cortex. In the retina, there are three neuron layers, namely, photoreceptors, biopolar cells and ganglion cells. Photoreceptors (cones and rods) sense the optical information on their receptive fields, and convert it into electrical signal for consequent transmission via the LGN to the cortex. The lateral geniculate fibers predominantly terminate on dendritic spines of stellate cells, and then project to the pyramidal cells. The postsynaptic potentials

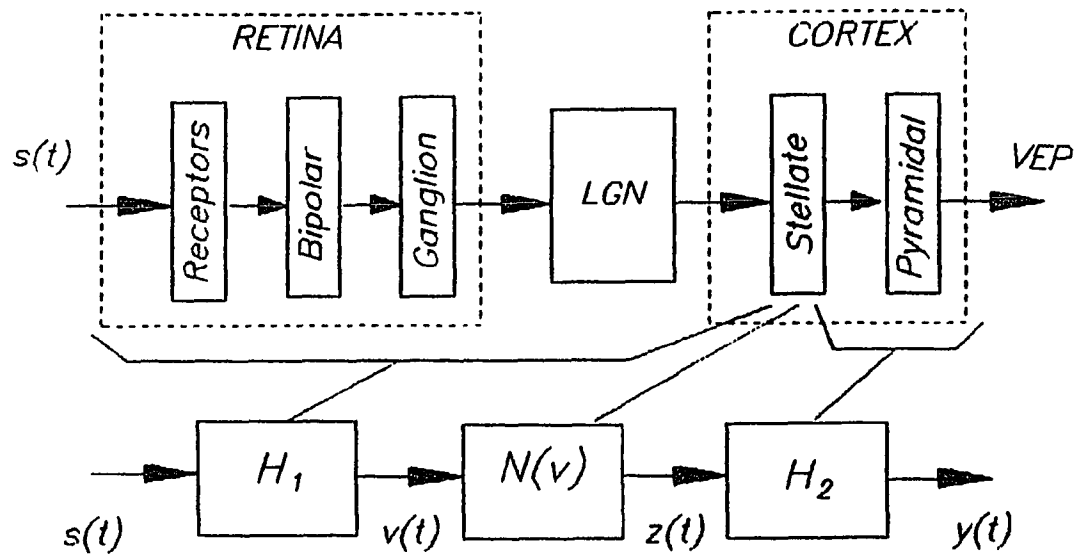

Figure 1.3 VEP pathway is basically composed of three stages. retina. lateral geniculate nucleus and cerebral cortex. The pathway characteristics. which depend on the various cells characteristics. can be simulated by a deterministic sandwich model.

of apical dendrites. characteristically arise from the body of the pyramidal cells and point toward the cortical surface. are the major source of the VEP recorded from the cortical skin.

1.4.1 Rectification Process

It has been observed that sinusoidal stimulation produces a VEP containing multiple harmonics and intermodulation components of the original frequency of the input (Spekreijse and Reits, 1982; Zemon, Conte, Jindra & Camisa, 1985). This phenomena implies that a nonlinear process exists in the VEP pathways (otherwise the VEP will only contain the frequency components of the input). The nonlinear process is perceived to be a kind of rectification (Spekreijse and Oosting, 1970; Regan, 1989),

which may result from the signal processing behavior at the front stage of the cortex. It was found that there is a large inhibitory activity involved in the signal processing within this neuron layer due to highly branched connection (Benevento, Creutzfeldt & Kuhnt, 1972; Creutzfeldt, Kuhnt & Benevento, 1974). A cell in this layer may receive many inhibitory signals from the local neighboring cells, resulting in cancellation of the incoming, or a portion of the incoming, excitatory signals from the lateral geniculate axons. Thus, the overall inhibitory signals a cell receives can be presented as a threshold for the excitatory signal to stimulate this cell. A rectifier with a threshold to represent such a cell input-output relation is illustrated in Figure 1.4. From a neural network point of view, since the stellate cell layer presents a large threshold to the incoming signals from the early neural layers, the rectification process in the visual pathway is thought to be essentially located in the front stage of the cortex (Zemon et al, 1985).

1.4.2 Linear Processing prior to the Rectification

The first linear element H_1 in the sandwich model represents a linear process in the early stage of the Visual neural pathways. This result comes from studies of single cell behaviors in both retina and lateral geniculate nucleus. Some relevant terms used in these studies will be introduced first.

Temporal linearity

A neuron has a *temporal linearity* if its response, in terms of its firing rate or dendrite potential, to a stimulus that is modulated sinusoidally in time has a sinusoidal time course (otherwise, the cell has *temporal nonlinearity*).

Spatial linearity

Dividing a neuron receptive field into several portions, if the neuron response to its receptive field stimulation is a linear summation of the responses which correspond to each partial field stimulation, the neuron has *spatial linearity* (otherwise, the neuron has *spatial nonlinearity*). In particular, when a cell unit formed by a group of cells has more than one separate receptive fields, the *spatial linearity* means that the unit

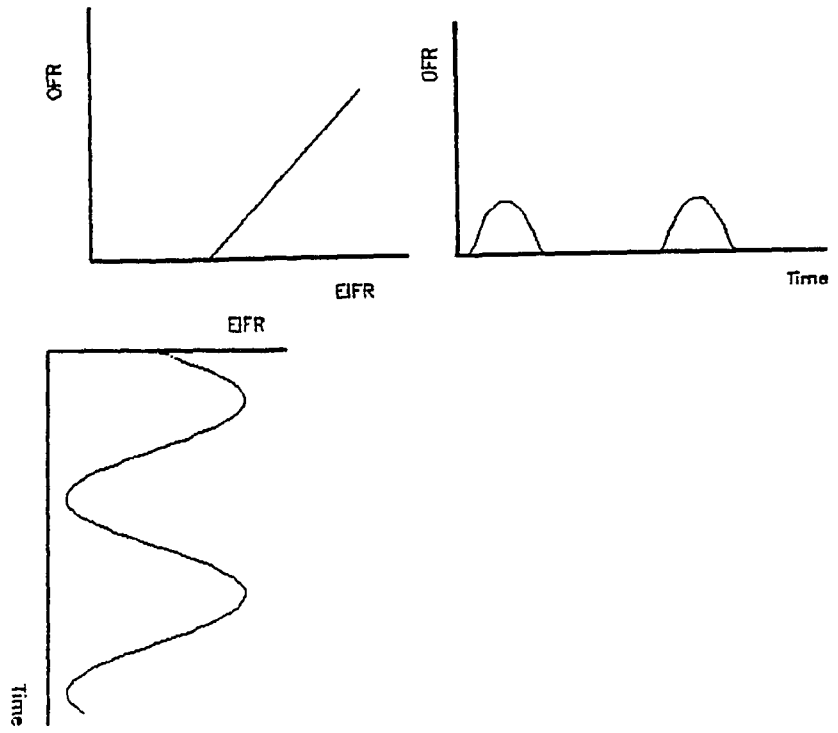

Figure 1.4 The output firing rate (OFR) of a cortical neuron as a function of the excitatory incoming firing rate (EIFR), modeled by a threshold rectifier.

response to its total receptive field stimulation is linearly summed from the responses corresponding to stimulation of each individual field. *Spatial nonlinearity* may result from nonlinear summation between spatially discrete or overlapping subregions.

Tranchina and his co-workers (1981) demonstrated, by recording intracellularly from horizontal cells in the turtle retina, that neural processing in the distal retina is highly linear over a wide range of spatial-temporal conditions. Furthermore, the ganglion cells in the retina and LGN can be broken down, by their property, into X cells which are spatially-temporally linear, and Y cells which are spatially-temporally nonlinear (Enroth-Cugell & Robson, 1966); or by their functions, into M cells which are more sensitive to luminance modulation, and P cells which are more sensitive to chromatic modulation (De Monasterio & Gouras, 1975; Lee et al, 1990). Researches showed that all P cells are X-like and approximately 75% of M cells are also X-

like; only 25% of M cells are Y-like (Shapley, Kaplan & Soodak, 1981; Blakemore & Vital-Durand, 1981; Kaplan & Shapley, 1982).

The investigations above lead to the conclusion that most of the cells in the early stage proceeding the cortex present linear processing behavior, which can be therefore represented by the first linear element H_1 in Figure 1.3.

1.4.3 Linear Processing Posterior to the Rectification

Spitzer and Hochstein (1985 a; b) classified cortical neurons in terms of their spatial-temporal behaviors as *simple cells* and *complex cells*, and reasoned that the response of a complex cell is a linear summation of rectified inputs. Since simple cells are found almost exclusively in layer IV, and complex cells are found above and below layer IV, but rarely in layer IV (Hubel & Wiesel, 1962; 1968), the conclusion by Spitzer and Hochstein suggests that pyramidal cells (not in layer IV, hence are complex cells) linearly process the rectified inputs projected from spiny stellate cells. This linear process in the last stage can be represented by the second linear element H_2 in the model.

1.5 Objective, Outline and Contribution

1.5.1 Objective

The sandwich system for VEP modeling was proposed many years ago, but a complete mathematical description of the model has not come out so far. It is thus the objective of this dissertation: *to develop a mathematical model and identification method for the human VEP, based on the sandwich system.*

Major benefits anticipated from such a model include the advancement of physiological knowledge on functional subsystems in the neural network and a better understanding of signal processing in the various stages of visual neuron pathways. In the clinical area, VEP models can be used as diagnostic tools. Diseases may affect the visual nerve system to generate different response wave forms in comparison with the normal ones. Such wave form modifications have been reported for

Alzheimer's disease (Trick, 1991), epilepsy (Ratliff & Zemon, 1984), multiple sclerosis (Halliday, McDonald & Mushin, 1973a; Zemon, 1984), neuron synaptic malfunction (Bodis-Wollner & Onofrj, 1982), retinitis pigmentosa (Berson, 1975), and visual acuity (Halliday, Mcdonald & Mushin, 1973b). Instead of describing those wave form changes in terms of "features" of recordings, they can be translated into modifications of a finite set of model parameter values which, in turn, may be associated with disease states and their physical location.

1.5.2 Outline of Work Conducted

This work focuses on VEP modeling based on the sandwich system. First, mathematical descriptions (including transfer functions) were sought for each element in the sandwich model. A two-sinusoid technique (to be discussed in Section 2.1) was selected for identifying the model. It composes a contrast reversing pattern stimulation, containing a luminance function temporally modulated by a sum of two sinusoids. Transfer functions of the two linear elements were identified in terms of the sum and difference frequency components elicited by this stimulation. According to the two-sinusoid strategy, we determined the nonlinearity in the model based on the nonlinear processing behavior in the VEP pathways before the linear element identification. Because even order harmonics were predominantly found in VEP due to periodical contrast reversing pattern stimulation, the nonlinearity selected was a full-wave linear rectifier, which is perhaps the simplest static nonlinear form for generating even harmonics. Since different nonlinearity selection might lead to a different result of the linear transfer function identification, methodology for selecting the nonlinearity was discussed, and the effect caused by a variety of selection for the nonlinearity was also analyzed in the dissertation.

We examined the VEP data measured from a group of ten adult human subjects to determine the transfer function formations. Mathematical analysis showed that, to fit the VEP sum and difference frequency components measured from those subjects, the transfer function formation of the first linear element has a non-minimum phase

characteristic with zeros on the right half s-plane. This result has not been shown in previous investigation of temporal characteristics of either single neurons or evoked potentials (Section 3.3).

Previous studies on electrical activities of single cells and global visual system (VEP) showed that there are two inhibitory mechanisms (to be described in detail in Chapter 4), contrast gain control located in both the retina and the cortex (Shapley & Victor, 1978, 1981; Zemon, Conte & Camisa, 1987), and lateral interaction mainly located in the cortex (Zemon, Victor & Ratliff, 1986), which modify both signal magnitude and phase in a nonlinear manner. It appears that the VEP intermodulation components due to two-sinusoid stimulation do not only depend on the forward processes before and in the cortex (which are represented by the first and second linear element in the sandwich system), but also depend on the effects of the inhibitory mechanisms. The phenomena of such inhibitory processes in the VEP are also demonstrated in the present work (Subsection 4.2.2, 4.3.2). A shunting inhibition model (Furman, 1965; Nabet & Pinter, 1991) is used to explain this type of nonlinear process.

In the present work, a new model structure based on the original sandwich system is introduced, which includes nonlinear processes in the inhibitory mechanisms. The model extension work emphasized that the modified sandwich system should not only satisfy the minimum complexity requirement for fitting the VEP data, but more importantly, should present a good interpretation of major neural generators of VEP.

Two models are presented in the current work. In the first model, the effects of the inhibitory mechanisms are expressed as steady-state control of parameters. This model can provide a good fit and prediction for the VEP frequency responses over the entire testing range (1.22–30 Hz), but fails to describe the VEP transient response.

The second model developed during this work has the same basic structure as the first one, but the parametric control is achieved dynamically. This model can provide a good fit for the VEP transient response. However, its frequency response match is poorer than that of the first model.

For each of the two models, parameter identification procedures have been developed and used for two human subjects.

1.5.3 Contributions

The essential contributions of the present research can be summarized as follows:

1. A new model structure has been proposed based on the sandwich system with consideration of incorporating lateral interaction and contrast gain control mechanisms. This extended model permits the analysis of separate excitatory and inhibitory processes (Section 5.1).
2. Mathematical equations and identification procedures have been introduced to describe and identify the model. This work advanced sandwich modeling for the human VEP in steady-state operation. Moreover, VEP modeling has been extended beyond the frequency domain consideration to the time domain consideration.

1.5.4 Organization of Dissertation

The dissertation contents are arranged as follows:

Chapter 2 (Section 2.1) begins with an introduction of the two-sinusoid stimulation method used for identifying the sandwich model. Later in that chapter, methods of VEP measurement and data processing are described.

Chapter 3 discusses sandwich model fitting for steady-state VEPs, which includes nonlinearity type selection, VEP intermodulation components due to the two-sinusoid stimulation, and transfer function formation. The chapter concludes with a discussion of model deficiencies.

Chapter 4 begins with a general introduction of inhibitory mechanisms (Section 4.1). Section 4.2 introduces the concept of contrast gain control and presents experimental results on the effect of stimulus contrast. Section 4.3 discusses lateral interaction, and presents a test protocol using three-sinusoid stimulation developed for the investigation of lateral inhibitory process. A shunting inhibition model is discussed in Section 4.4 to provide a physiological explanation for those inhibitory

processes and their effects in neuron signal transmission.

Chapter 5 contains the result of the model structure development for the first model. including its mathematical description, system identification procedure, and model validation.

Chapter 6 describes the VEP transient response, development of the second model, system identification procedure, and model fitting.

Chapter 7 presents a summary, discussion and conclusions on the present work as well as suggestions for future research.

CHAPTER 2
METHOD

2.1 Rationale for the Two-Sinusoid Approach

There are varieties of strategies to determine the transfer characteristics of the elements within the sandwich system. One of the popular approaches is the characterization of the nonlinear system in terms of Wiener kernels (Wiener, 1958), obtained from an analysis of the system response to Gaussian white noise input. These kernels can be calculated by polycorrelation of input and output signals (Lee & Schetzen, 1961), and can further be estimated by the Fourier transform of input and output signals (Kim, Wang, Powers & Roth, 1979). Its application to physiological systems can be found in the textbook by Marmarelis & Marmarelis (1978). Another alternative approach is to use an input with multiple sinusoids to approximate Gaussian white noise. This approach has been introduced to the visual neuron cell modeling by Victor and Shapley in 1980. One of the advantages of this method compared with Wiener Kernels is that the input is deterministic and thus easier to control. However, visual evoked potential recording, other than neuron cell firing rate is readily disturbed by noise. Tests in this laboratory showed that the frequency components of VEP, elicited by the random or "random-like" function stimulus, has low signal to noise ratio and is not suitable for use in VEP system modeling. Therefore, a two-sinusoid stimulation (a deterministic approach) was selected for the current research, which can elicit relatively reliable VEP response. The two-sinusoid technique has been used by Zemon and his co-workers for VEP researches, and was reported in several papers (e.g. Zemon, 1984; Zemon et al, 1985; 1986). The principle of the two-sinusoid technique is described as follows:

For an input containing two sinusoids at frequencies f_1 and f_2, a linear system produces two steady-state sinusoidal outputs of the same frequencies. In the sandwich system, however, nonlinear processing produces output components of intermodulation frequencies and harmonics of frequencies f_1 and f_2. The basic intermodulation components, sum frequency component (the component at the frequency $f_1 + f_2$) and

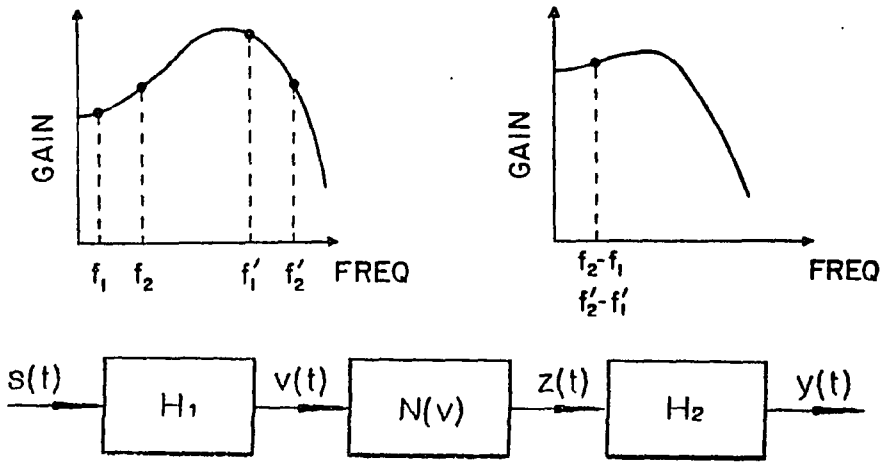

Figure 2.1 Demonstration of two-sinusoid approach for identifying the linear elements in the sandwich model.

difference frequency component (the component at the frequency $f_2 - f_1$), can be used to characterize the linear elements H_1 and H_2 if the frequency pair f_1 and f_2 is carefully chosen.

As shown in Figure 2.1, the output of H_1 due to the two-sinusoid input is also a two-sinusoids at frequencies f_1 and f_2 because of linearity of H_1. This signal is processed further by the nonlinearity $N(v)$ to produce components including a difference frequency component (DFC) and a sum frequency component (SFC). Now, if we change the input frequency pair f_1 and f_2, for example, to f_1' and f_2', but keep the difference as a constant, that is, $f_2 - f_1 = f_2' - f_1'$, each of the two sinusoids entering $N(v)$ will change in amplitude and phase according to the frequency characteristic of H_1. However, the DFCs produced from $N(v)$ still remain at the same frequency. Those difference frequency components with identical frequency will be identically filtered by the second linear filter H_2. In this way, H_2 merely offers a constant gain and phase shift to the DFC. The DFC response curve, obtained by using an entire set of frequency pairs with equal separation between frequencies in each pair, therefore

depends only on H_1 and $N(v)$. If the characteristic of $N(v)$ is known, it is possible to recover the characteristic of H_1 from the DFC response. In the following, we give a mathematical analysis of this issue, and show how the difference and sum frequency components can be used to determine the transfer function of the linear elements H_1 and H_2. This mathematical analysis is based on the paper by Spekreijse and Reits (1982).

First, for given a two-sinusoid input to the nonlinearity N, the equations for calculating the sum and difference frequency components in the output of N should be established. Suppose the input-output relation of the nonlinearity is given by

$$z(t) = N[v(t)] \tag{2.1}$$

where $v(t)$ and $z(t)$ is the value of input and output at time t respectively. The Fourier transform $F(ju)$ of the nonlinearity $N(v)$ is

$$F(ju) = \int_{-\infty}^{\infty} N(v)\epsilon^{-juv}dv \tag{2.2}$$

With the input as a sum of N sinusoids,

$$v(t) = \sum_{k=1}^{N} A_k \cos(\omega_k t + \phi_k) \tag{2.3}$$

one finds

$$\begin{aligned} z(t) = N[v(t)] &= \frac{1}{2\pi}\int_C F(ju)e^{juv(t)}du \\ &= \frac{1}{2\pi}\int_C F(ju)\exp\{ju\sum_{k=1}^{N} A_k\cos(\omega_k t + \phi_k)\}du \end{aligned} \tag{2.4}$$

where C is a contour extending from $-\infty$ to ∞ selected to exclude singularities.

According to the Jacobi-Anger formula (Gradshteyn & Ryzhik, 1980, page 973),

$$\exp[juA_k\cos(\omega_k t + \phi_k)] = \sum_{n=0}^{\infty} j^n \epsilon_n J_n(uA_k)\cos n(\omega_k t + \phi_k) \tag{2.5}$$

where ϵ_n is the Neumann factor that $\epsilon_0 = 1$ and $\epsilon_n = 2$ for $n \neq 0$, J_n is the Bessel function of the first kind,

$$z(t) = \frac{1}{2\pi}\int_C F(ju)\prod_{k=1}^{N}\sum_{n=0}^{\infty} j^n\epsilon_n J_n(uA_k)\cos n(\omega_k t + \phi_k)du \tag{2.6}$$

For $N = 2$ (two-sinusoid input),

$$z(t) = \frac{1}{2\pi}\int_C F(ju)\sum_{n=0}^{\infty} j^n \epsilon_n J_n(uA_1)\cos n(\omega_1 t + \phi_1)$$

$$\times \sum_{m=0}^{\infty} j^m \epsilon_m J_m(uA_2)\cos m(\omega_2 t + \phi_2)du$$

$$= \sum_{n=0}^{\infty}\sum_{m=0}^{\infty} B_{nm}\{\cos[(n\omega_1 - m\omega_2)t + n\phi_1 - m\phi_2]$$

$$+ \cos[(n\omega_1 + m\omega_2)t + n\phi_1 + m\phi_2]\} \tag{2.7a}$$

where

$$B_{nm} = \frac{1}{4\pi}\epsilon_n\epsilon_m j^{n+m}\int_C F(ju)J_n(uA_1)J_m(uA_2)du \tag{2.7b}$$

The difference frequency component (DFC) and sum frequency component (SFC) will be produced by the terms that $n = m = 1$ if ω_1 and ω_2 are selected such that there are no other intermodulation or harmonic components overlapping the DFC and SFC. In this case, the amplitudes of DFC and SFC are identical, and given by

$$A_{zDFC}(f_1, f_2) = A_{zSFC}(f_1, f_2) =$$

$$B_{11} = -\frac{1}{\pi}\int_C F(ju)J_1(uA_1)J_1(uA_2)du \tag{2.8}$$

The phase angle of DFC is given by

$$\phi_{zDFC}(f_1, f_2) = \phi_1 - \phi_2 \tag{2.9a}$$

and the phase angle of SFC is given by

$$\phi_{zSFC}(f_1, f_2) = \phi_1 + \phi_2 \tag{2.9b}$$

where ϕ_1 and ϕ_2 are the phase angles of two sinusoids in the input. Note, if sin rather than cos is used in all the equations above, the phase angle of DFC and SFC will be, respectively

$$\phi_{zDFC}(f_1, f_2) = \phi_1 - \phi_2 + \frac{\pi}{2} \tag{2.10a}$$

$$\phi_{zSFC}(f_1, f_2) = \phi_1 + \phi_2 - \frac{\pi}{2} \tag{2.10b}$$

Next, we set up the input-output relation for the entire system. We denote $|H_1(f)|$ and $\angle H_1(f)$ as the gain and phase characteristics of H_1 respectively; $|H_2(f)|$ and $\angle H_2(f)$ as the gain and phase characteristics of H_2 respectively. For a two-sinusoid system input

$$s(t) = C_w[\sin(2\pi f_1 t) + \sin(2\pi f_2 t)] \tag{2.11}$$

where C_w is the amplitude or the modulation depth of the two sinusoids, the steady-state output of H_1 is also a two-sinusoidal function with amplitudes:

$$A_v(f_1) = C_w|H_1(f_1)| \tag{2.12a}$$

$$A_v(f_2) = C_w|H_1(f_2)| \tag{2.12b}$$

and phases:

$$\phi_v(f_1) = \angle H_1(f_1) \tag{2.12c}$$

$$\phi_v(f_2) = \angle H_1(f_2) \tag{2.12d}$$

Substitute $A_v(f_1)$ and $A_v(f_2)$ for A_1 and A_2 respectively in (2.8), and $\phi_v(f_1)$ and $\phi_v(f_2)$ for ϕ_1 and ϕ_2 in(2.10a, b) respectively, one obtains the DFC and SFC in the output of the nonlinearity

Amplitude:

$$A_{zDFC}(f_1, f_2) = A_{zSFC}(f_1, f_2)$$
$$= -\frac{1}{\pi}\int_C F(ju)J_1(uC_w|H_1(f_1)|)J_1(uC_w|H_1(f_2)|)du \tag{2.13}$$

Phase angle:

$$\phi_{zDFC}(f_1, f_2) = \angle H_1(f_2) - \angle H_1(f_1) + \frac{\pi}{2} \tag{2.14a}$$

$$\phi_{zSFC}(f_1, f_2) = \angle H_1(f_1) + \angle H_1(f_2) - \frac{\pi}{2} \tag{2.14b}$$

Finally, after filtering of H_2, the DFC and SFC produced in the entire system output are

DFC amplitude:

$$A_{yDFC}(f_1, f_2) = -|H_2(f_2 - f_1)|\frac{1}{\pi}\int_C F(ju)J_1(uC_w|H_1(f_1)|)J_1(uC_w|H_1(f_2)|)du \tag{2.15a}$$

SFC amplitude:

$$A_{ySFC}(f_1, f_2) = -|H_2(f_1 + f_2)|\frac{1}{\pi}\int_C F(ju)J_1(uC_w|H_1(f_1)|)J_1(uC_w|H_1(f_2)|)du \tag{2.15b}$$

DFC phase angle:

$$\phi_{yDFC}(f_1, f_2) = \angle H_1(f_2) - \angle H_1(f_1) + \frac{\pi}{2} + \angle H_2(f_2 - f_1) \tag{2.16a}$$

SFC phase angle:

$$\phi_{ySFC}(f_1, f_2) = \angle H_1(f_1) + \angle H_1(f_2) - \frac{\pi}{2} + \angle H_2(f_1 + f_2) \tag{2.16b}$$

The above relations lead to the following conclusions:

If $f_2 - f_1$ is kept as constant as f_1 is changed. $|H_2(f_2 - f_1)|$ and $\angle H_2(f_2 - f_1)|$ also remain constant. For given nonlinearity $N(v)$ and system input (2.11),

1. The amplitudes of DFC and SFC produced from the nonlinearity $N(v)$ are identical ((2.8)).
2. The amplitude ratio of SFC and DFC is given by

$$\frac{A_{ySFC}(f_1, f_2)}{A_{yDFC}(f_1, f_2)} = \frac{|H_2(f_1 + f_2)|A_{zSFC}(f_1, f_2)}{|H_2(f_2 - f_1)|A_{zDFC}(f_1, f_2)} = \frac{|H_2(f_1 + f_2)|}{|H_2(f_2 - f_1)|} \tag{2.17}$$

   which is a normalized (by a constant $|H_2(f_2 - f_1)|$) gain characteristic of H_2. This property can be utilized for identifying H_2.
3. Theoretically, the relation between $|H_1(f)|$ and the amplitudes of DFC and SFC produced from the entire system are expressed by (2.15a) and (2.15b) respectively. However, if $A_{yDFC}(f_1, f_2)$, the VEP data of DFC amplitude, is given, finding $|H_1(f)|$ through (2.15a) is not practical in general. In Section 3.1, an approximate method will be used to set up an equation suitable for finding $|H_1(f)|$ by computer.
4. Except for a constant, the phase angle of DFC in the output $\phi_{yDFC}(f_1, f_2)$ is the difference between the phase angle of the two individual frequency components in the output of H_1 ((2.16a)).

5. Except for a constant, the phase angle of SFC in the output $\phi_{ySFC}(f_1, f_2)$ is the summation of the phase angle of the two individual frequency components in the output of H_1 and the phase angle of H_2 at frequency $f_1 + f_2$ ((2.16b)). Equations (2.16a) and (2.16b) can be combined to determine the phase characteristics of H_1 and H_2.

The above analysis demonstrates that these conclusions hold for any type of static nonlinearity $N(v)$, which will serve as an important analytic tool in system identification.

2.2 Stimuli

The stimulus. created as a dartboard pattern of 3 inches diameter (shown in Figure 2.2). is controlled by an 80386 microcomputer through the driver. The stimulus pattern is displayed on a Tektronix 608 oscilloscope (manufactured by Tektronix Inc., Beaverton, Oregon). The entire displaying area consists of a 256×256 pixel raster displayed at a frame rate (rate of refreshing a whole screen image) of 255.31 Hz. The luminance of each segment in the dartboard pattern is modulated temporally as

$$L(t) = L_m[1 + s(t)] \tag{2.18a}$$

for one set of segments (for example, white segments in Figure 2.2), and

$$L(t) = L_m[1 - s(t)] \tag{2.18b}$$

for the other set of alternate segments (for example, black segments in Figure 2.2), where $L_m = 150\ cd/m^2$, $L(t)$ is a luminance function, $s(t)$ is a temporally modulated signal. and $|s(t)| \leq 1$ for any t. During an experiment, when half of the displaying area increases in luminance at any time, the other half of the displaying area decrease by exactly the same amount. Thus the luminance of the stimulus pattern is of the contrast reversal type, such that the average luminance over the entire display area is always kept at a constant L_m. For the sake of modeling, either one of equations. (2.18a) or (2.18b) can be defined as the system input.

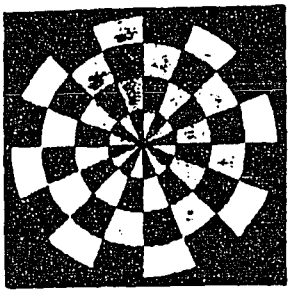

Figure 2.2 Contrast reversed stimulus pattern. When one set of segments increase in luminance. the other set of segments decrease. The mean luminance over all displaying area maintains a constant.

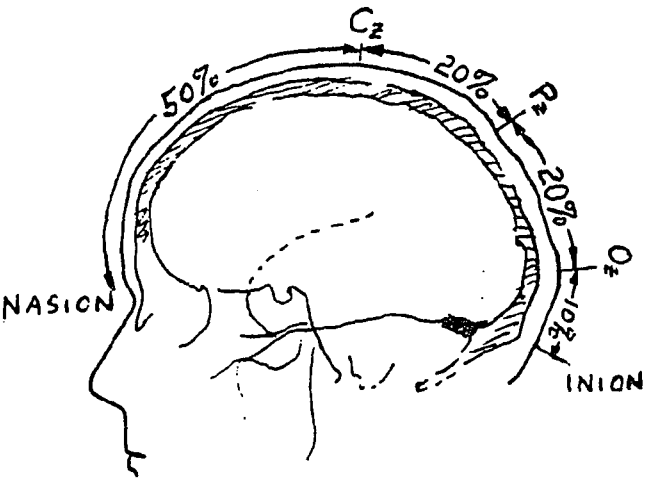

Figure 2.3 Lateral view of skull to show the method of measurement from nasion to inion at the midline. Electrodes are placed at the points O_z, P_z and C_z.

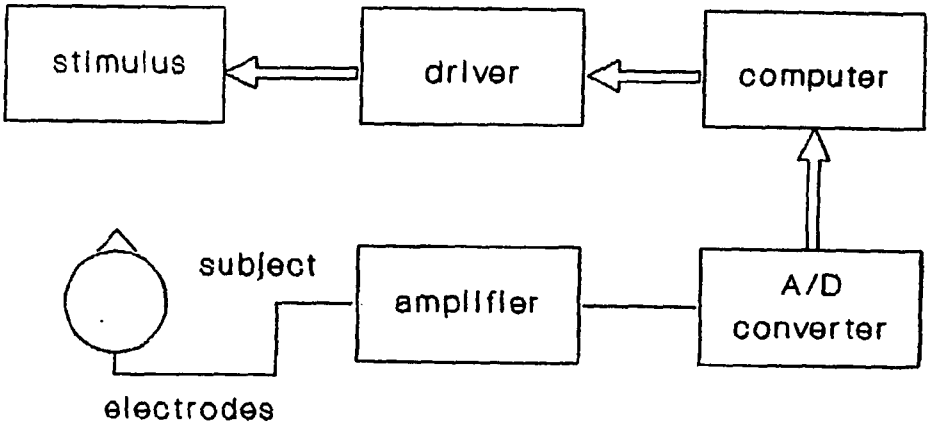

Figure 2.4 A system diagram for VEP measuring. A subject is set one meter from the stimulus displayed on a monitor. The stimulus can be controlled by the computer through the driver. VEP responses are picked up from the cortical surface with electrodes. and then amplified, filtered. A to D converted and stored in the computer for later analysis.

Two types of temporal stimuli, two-sinusoidal and square wave, were mainly used in this research. The responses due to two-sinusoidal stimulation were processed to obtain frequency spectra; square wave stimulation was done with low frequencies (not higher than 1 Hz) to obtain effective averaged transient responses. The temporal modulation signal $s(t)$, for two-sinusoidal stimulation, is given by (2.11), in which frequency f_i ranges from 1.22 to 30 Hz; for square wave stimulation, is given by:

$$s(t) = \begin{cases} C_w & nT < t \leq (n+1/2)T \\ -C_w & (n+1/2)T < t \leq (n+1)T \end{cases} \quad n = 0, 1, 2, \ldots \tag{2.19}$$

where T is a period set to 1 second in transient response test. In both equations (2.11) and (2.19). C_w is a modulation depth defined as the Weber contrast

$$C_w = |s(t)|_{max} = \frac{L(t)_{max} - L_m}{L_m} \tag{2.20}$$

When C_w is set. the peak luminance on the stimulus pattern is determined by (2.20). For example, if $L_m = 150\ cd/m^2$ and C_w is set to 30%, then

$$L(t)_{max} = C_w L_m + L_m = 195\ cd/m^2$$

2.3 VEP Recording

Three electrodes were placed along the midline of the head as described by Jasper (1958) and Zemon et al (1988). C_z (positive lead) at the middle point of nasion-inion distance was connected to the negative input of the amplifier as a reference, while the Q_z (negative lead), positioned 10 percent of nasion-inion distance above inion was connected to the positive input of the amplifier. The third point P_z, 50% of the distance between C_z and Q_z, served as floating ground. The diagram of electrode connection is shown in Figure 2.3. The Model 600 amplifier (manufactured by NeuroScientific Corp.) was set to AC mode with an amplification gain of 20k and a bandpass filter from 0.03 Hz–100 Hz. It is believed that this bandwidth essentially

covers most VEP frequency components because above 40 Hz, the VEP response reduces to noise level.

2.4 Procedure

The experiments for measurement of VEP were carried out in a dark room. The system, illustrated in Figure 2.4, consisted of a stimulus, driver, amplifier, A/D converter and a computer. The subjects were instructed to relax their muscles and fixate on the center of the stimulus pattern. Monocular stimulation was used in all the tests (one eye covered). The subject was placed one meter away from the screen. While the computer was controlling the stimulus display for the subject, it sampled the VEP response from the cortical surface through the electrodes, amplifier and A/D converter. During the test, the computer also analyzed the sampled data and displayed the results. Sampled data were stored in the computer for later studies. The entire test procedure (driving stimuli, sampling responses, displaying results and storing data) was monitored by VENUS software produced by NeuroScientific Corporation. Farmingdale, New York.

2.5 Data processing

Three data processing methods are used in this work, namely *data averaging*, *Fourier transform* and *digital filtering*. To demonstrate the processing procedures, we denote m as a total number of repeated measurements, ΔT as the sampling interval and $y_j(i\Delta T)$ as the jth response at time $i\Delta T$ ($i = 0, 1, 2, \cdots$; $j = 1, 2, \cdots, m$). For each response, the signal duration is broken up into M "*records*" to correspond to the periodic stimulus changes. Assemble averaging on these records is done to reduce noise. Each of the M records includes N samples. Thus, the total number of samples for the signal duration is NM.

Data average—square-wave stimulation test

In the square-wave stimulation test, a period of 1 second was used, producing 2 records per second corresponding to 2 contrast reversals. Stimuli ran a total of 64.17 second with refresh rate 255.31 Hz. During that time, a total number of $M = 128$ records were produced. With a sampling rate of 255.31 Hz, each record of 0.5 second length involved $N = 128$ samples. Thus, the total number of samples taken during a 64.17 second run was $MN = 128 \times 128 = 16,384$. The jth effective-averaged transient responses $\overline{y}_j$ is derived by averaging M=128 sets of periodic data

$$\overline{y}_j(i\Delta T) = \frac{1}{M}\sum_{k=0}^{M-1} y_j[(i+kN)\Delta T] \qquad i = 0.1.2,\cdots,N-1 = 127 \tag{2.21a}$$

The mean response over all m repeated measurements $\overline{y}_j$ is given by

$$\overline{y}(i\Delta T) = \frac{1}{m}\sum_{j=1}^{m} \overline{y}_j(i\Delta T) \qquad \begin{matrix} i = 0.1.2,\cdots,N-1 = 127 \\ j = 1.2,\cdots,m \end{matrix} \tag{2.21b}$$

Fourier Transform–two-sinusoidal stimulation test

In the two-sinusoidal stimulation test, the stimuli ran 32.08 seconds with refresh rate 255.31 Hz. The data sampling rate was chosen as twice the stimulus refresh rate, or 510.62 Hz, resulting in total samples during the measurement period of 32.08 seconds $NM = 32 \times 256 \times 2 = 16,354$. The frequency components of interest are derived by Fourier transform of the data recorded. By specifying record length N, The real and imaginary parts of the component in the jth response are calculated by, respectively:

$$a_j = \frac{2}{NM}\sum_{i=0}^{NM-1} y_j(i\Delta T)\cos\frac{2\pi i}{N} \qquad j = 1,2,\cdots,m \tag{2.22a}$$

$$b_j = \frac{2}{NM}\sum_{i=0}^{NM-1} y_j(i\Delta T)\sin\frac{2\pi i}{N} \qquad j = 1,2,\cdots,m \tag{2.22b}$$

This computation uses all M records. Fast computation can be obtained by using one averaged record length:

$$a_j = \frac{2}{N}\sum_{i=0}^{N-1} \overline{y}_j(i\Delta T)\cos\frac{2\pi i}{N} \qquad j = 1,2,\cdots,m \tag{2.23a}$$

$$b_j = \frac{2}{N}\sum_{i=0}^{N-1} \overline{y}_j(i\Delta T)\sin\frac{2\pi i}{N} \qquad j = 1,2,\cdots,m \tag{2.23b}$$

where $\overline{y}_j$ is the jth averaged response over M sets of periodic data obtained by (2.21a). The amplitude and phase angle of the component are, respectively:

$$Am_j = \sqrt{a_j^2 + b_j^2} \qquad j = 1, 2, \cdots, m \tag{2.24a}$$

$$\psi_j = \arctan\left(\frac{b_j}{a_j}\right) \qquad j = 1, 2, \cdots, m \tag{2.24b}$$

The calculation of mean values and variabilities of the amplitude and phase over m measurements is a little more complicated than that of the mean transient response. We will discuss this problem in the next section.

Digital filtering

Filtering process is carried out in such a way that first, each frequency component (fundamental and harmonics) is calculated by fast Fourier transform. The jth averaged response over M sets of periodic data $\overline{y}_j$ can then be expressed by a sum of Fourier components

$$\overline{y}_j(i\Delta T) = \sum_{n=1}^{\infty} A_{jn} \sin(\frac{2\pi in}{N} + \phi_{jn}) \qquad j = 1, 2, \cdots, m \tag{2.25}$$

The frequency components to be filtered are taken out from (2.25), and the remaining terms sum together to form a filtered average response. For example, a lowpass filtering to exclude the tenth and higher harmonics will give the jth averaged response

$$\overline{y}_j(i\Delta T) = \sum_{n=1}^{9} A_{jn} \sin(\frac{2\pi in}{N} + \phi_{jn}) \qquad j = 1, 2, \cdots, m \tag{2.26}$$

One advantage of this filtering process is that it will not produce a supplementary phase shift for each frequency component in the original signal.

2.6 Statistical Analysis of Steady-State VEP

In this section, we describe the method used to obtain i) an estimate of a VEP Fourier component from repeated measures; ii) the variability of the estimate of VEP Fourier component.

VEP frequency response can be characterized by the amplitude and phase, or the real and imaginary part, of Fourier component at one or more frequencies of

interest. An estimate of a Fourier component of evoked potential is obtained from several repeats of the measurement. Individual estimates of the Fourier component can, as vectors, form a cluster in the complex s-plane. The center of the cluster is a pooled estimate of the response, and the scatter of the cluster describes the reliability of that estimate. To give an estimate of the VEP Fourier components and their variability, a T^2_{circ} statistic (Victor and Mast, 1991) is used in this research, which is based on the assumption that i) the noise (i.e. the background electroencephalogram (EEG)) is a normal process (Elul. 1969), and ii) EEG noise and evoked potential signal combine additively and are independent (Mast & Victor, 1990). These two assumptions provide a sufficient condition that the real and imaginary parts of Fourier components are equal variances and zero covariance (Mast & Victor, 1990), which is the critical requirement for the derivation of the T^2_{circ} statistic.

Now we denote a set of m measures of evoked responses as $y_1(t)$, $y_2(t)$, $\cdots$, $y_m(t)$, and their Fourier components as Y_1, Y_2, $\cdots$, Y_m, whose decompositions into real and imaginary parts are $Y_j = a_j + ib_j$ $(j = 1, 2 \cdots, m)$. We define the Fourier component of the "true" evoked response as $Y = a + ib$. We assume that the signal $y_j(t)$ is a sum of two components: an evoked response, $e(t)$, and ongoing "noise" unrelated to the stimulus, $n_j(t)$:

$$y_j(t) = e(t) + n_j(t) \tag{2.27}$$

$n_j(t)$ represents not only endogenous EEG, but also exogenous sources of variability, such as signals generated by head movement. The expected value of the "noise" is assumed to be equal to zero. The "true" evoked response $e(t)$ is assumed to be a periodic function with period of the stimulus and to have no intrinsic variability. Thus, the expected value of the real part and imaginary part of Fourier component is given by, respectively

$$E(a_j) = E\{\frac{2}{T}\int_0^T [e(t) + n_j(t)] \cos \omega_n t dt\}$$

$$= \frac{2}{T}\int_0^T \{E[e(t)] + E[n_j(t)]\} \cos \omega_n t dt$$

$$= \frac{2}{T}\int_0^T e(t)\cos\omega_n t dt = a \tag{2.28}$$

and

$$E(b_j) = E\{\frac{2}{T}\int_0^T [e(t) + n_j(t)]\sin\omega_n t dt\}$$

$$= \frac{2}{T}\int_0^T \{E[e(t)] + E[n_j(t)]\}\sin\omega_n t dt$$

$$= \frac{2}{T}\int_0^T e(t)\sin\omega_n t dt = b \tag{2.29}$$

Therefore, the empirical mean value of Y_j, $\overline{Y}$, given by

$$\overline{Y} = \frac{\sum_{j=1}^m Y_j}{m} = \frac{\sum_{j=1}^m a_j}{m} + i\frac{\sum_{j=1}^m b_j}{m} = \overline{a} + i\overline{b} \tag{2.30}$$

is the estimate of the "true" component $Y = a + ib$. Note: i) Here, $\overline{Y}$ is a vector average from the m measurements. As m increases to infinity, $\overline{Y}$ approaches Y. If $y_j(t)$ satisfies normal distribution with mean $e(t)$, $\overline{a}$ and $\overline{b}$ also satisfy normal distribution with mean a and b respectively. ii) The Fourier component can also be expressed by amplitude and phase, but the amplitude of the "true" component can not be estimated by the amplitude average from the m measurements since

$$E(|Y_j|) = E(\sqrt{a_j^2 + b_j^2}) \neq \sqrt{E^2(a_j) + E^2(b_j)} = \sqrt{a^2 + b^2} = |Y| \tag{2.31}$$

Similarly, the phase angle of the "true" component can not be estimated by the phase angle average from m measurements.

Thus, the empirical mean values of amplitude and phase corresponding to $\overline{Y}$ are given by, respectively

$$\overline{Am} = |\overline{Y}| = \sqrt{\overline{a}^2 + \overline{b}^2} \tag{2.32a}$$

$$\overline{\psi} = \arctan\left(\frac{\overline{b}}{\overline{a}}\right) \tag{2.32b}$$

Next, we consider the estimate of variance of $\overline{Y}$ about the "true" component Y. Since T^2_{circ} statistic assumes that the variance of the real and imaginary parts of the component are equal and their covariance is zero, the cluster of Y_j is circularly symmetrical about Y, and the radius of the cluster is derived from the two deviations,

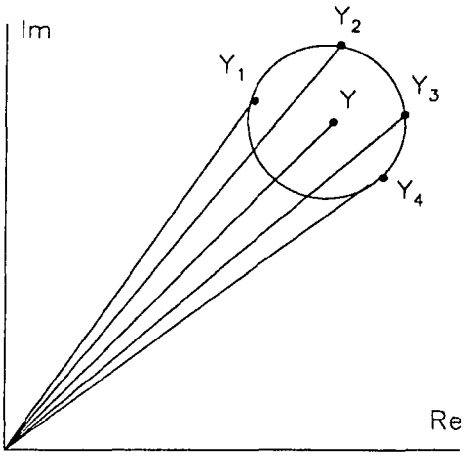

Figure 2.5 Geographical expression of T^2_{circ} statistic. The cluster of individual measure Y_j is circularly symmetrical about the "true" component Y. Thus, the standard deviation of Y_j is a circle centered by Y on the s-plane. The radius of the circle is estimated by the square root of (2.34).

$a_j - a$ and $b_j - b$. Suppose the variance of a_j and b_j are σ_a^2 and σ_b^2 respectively, the variance of Y_j is given by

$$Var(Y_j) = E[|Y_j - Y|^2] = E[(a_j - a)^2 + (b_j - b)^2] = \sigma_a^2 + \sigma_b^2 \tag{2.33}$$

The estimate of this variance from m measurements is derived by

$$Var(Y_j)_{est} = \frac{\sum_{j=1}^{m}(a_j - \overline{a})^2 + \sum_{j=1}^{m}(b_j - \overline{b})^2}{m-1} \tag{2.34}$$

One can prove that $E[Var(Y_j)_{est}] = Var(Y_j)$. The radius of the cluster is the square root value of $Var(Y_j)$. Figure 2.5 demonstrates such variability, in which, Y is the "true" component in s-plane; the expected deviation of Y_j forms a circle around Y with radius estimated by the square root of (2.34).

The variance of the mean, $\overline{Y}$, is then derived by

$$Var(\overline{Y}) = Var\left(\frac{\sum_{j=1}^{m} Y_j}{m}\right) = \frac{1}{m^2}\sum_{j=1}^{m} Var(Y_j)$$

$$= \frac{1}{m} Var(Y_j) = \frac{\sigma_a^2 + \sigma_b^2}{m} \tag{2.35}$$

According to (2.34), the estimate of this variance is given by

$$Var(\overline{Y})_{est} = \frac{\sum_{j=1}^{m}(a_j - \overline{a})^2 + \sum_{j=1}^{m}(b_j - \overline{b})^2}{m(m-1)} \tag{2.36}$$

Since the variance of Y_j represents the variability of the individual measurement, but the variance of $\overline{Y}$ represents the accuracy of the estimate for the "true" component Y, we have more interest in the latter one. We call the circle, representing the circular deviation of $\overline{Y}$ around Y, the "*error circle of the mean*", and denote the radius of the *error circle* as r_{circ}, which is estimated by

$$r_{circ} = \sqrt{Var(\overline{Y})_{est}} = \sqrt{\frac{\sum_{j=1}^{m}(a_j - \overline{a})^2 + \sum_{j=1}^{m}(b_j - \overline{b})^2}{m(m-1)}} \tag{2.37}$$

(2.30) and (2.37) give the estimate of VEP Fourier component and deviation in the s-plane.

When the Fourier component (individual or mean) is expressed in amplitude and phase (Bode plot), its deviations in amplitude and phase can not be obtained directly due to complicated integration forms. However, we can give a range for such deviations.

For the amplitude, since expected distance between $\overline{Y}$ and Y in s-plane is r_{circ}, $\overline{Y}$ can be considered as a component located on the *error circle* around Y. In this case, the amplitude of $\overline{Y}$ and Y have a maximum deviation, r_{circ}, when $\overline{Y}$ and Y have a same phase angle. Since $\overline{Y}$ has an equal probability to be at any point on the *error circle*, the expected deviation between the amplitude of $\overline{Y}$ and Y is less than r_{circ}, that is,

$$\sqrt{E(|\overline{Y}| - |Y|)^2} < r_{circ} \tag{2.38}$$

For the phase, when the radius of the *error circle* is less than the amplitude of Y, $\overline{Y}$ on the circle has a maximum phase deviation, $\arctan(r_{circ}/\sqrt{|Y|^2 - r_{circ}^2})$, when it is tangent on the circle (see Figure 2.6). For similar reason, Since $\overline{Y}$ has an equal probability to be at any point on the *error circle*, the expected phase deviation of $\overline{Y}$ is less than $\arctan(r_{circ}/\sqrt{|Y|^2 - r_{circ}^2})$, which is estimated by $\arctan(r_{circ}/\sqrt{|\overline{Y}|^2 - r_{circ}^2})$.

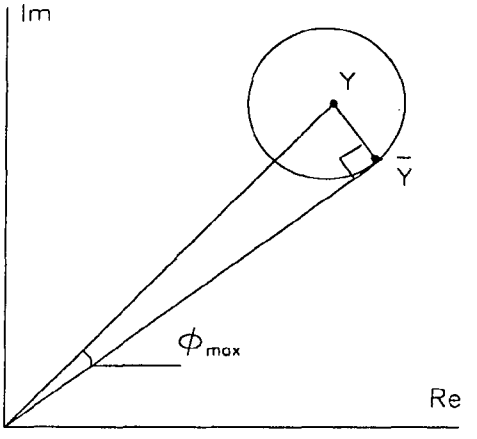

Figure 2.6 $\overline{Y}$ on the *error circle* has a maximum phase deviation, $\phi_{max} = \arctan(r_{circ}/\sqrt{|Y|^2 - r_{circ}^2})$, when it is tangent on the circle.

That is

$$\sqrt{E(\angle\overline{Y} - \angle Y)^2} < \arctan \frac{r_{circ}}{\sqrt{|\overline{Y}|^2 - r_{circ}^2}} \tag{2.39}$$

In the current work, the estimate of the VEP frequency component, $\overline{Y}$, obtained in terms of (2.30), the radius of *error circle*, r_{circ}, calculated from (2.37), and the error range of phase, estimated by (2.39) will be presented for each steady-state VEP test.

When $r_{circ} > |Y|$ or $r_{circ} > |\overline{Y}|$, the signal to noise ratio is small. In that case, the phase angle of $\overline{Y}$ is not a reliable estimate for the phase angle of Y, and will not be plotted in the figure.

CHAPTER 3

ANALYSIS OF SANDWICH MODEL FIT FOR STEADY-STATE VEPs

In this chapter, the sandwich system modeling for the VEP pathway will be discussed using the two-sinusoid technique. This work includes: i) establishment of a mathematical description for the model including the nonlinearity selection, ii) examination of the VEP frequency responses (sum and difference frequency components) elicited by the two-sinusoid stimulation to determine the types of linear filters in the model, iii) discussion of the model fits and the relation between the model functions form and the prior knowledge of temporal characteristics of the visual system.

3.1 Nonlinearity Selection

In terms of two-sinusoid method, the nonlinear element in the model should be determined before the identification of the linear transfer functions. The choice of the nonlinearity type is guided by the following consideration: i) The nonlinearity should, to some extent, be "explainable" in terms of the signal processing behavior in the retina-cortex system. ii) It should be as simple as possible. iii) The resultant model should represent the temporal characteristics of the VEP pathway.

In this work, the nonlinearity chosen is a full-wave rectifier with input-output relation

$$z(t) = N[v(t)] = |v(t)| \tag{3.1}$$

where $v(t)$ and $z(t)$ are the input and output of the nonlinearity respectively. The reasons for the choice of this rectifier, that is i) symmetrical full-wave, ii) nonthreshold, and iii) "linear" rectification, will now be discussed separately.

1. Symmetrical full-wave rectification

The predominance of even order harmonics in the VEP response, elicited by a contrast reversing pattern stimulation, demonstrates the full-wave rectification behavior in the VEP pathways (Zemon, 1984; Zemon et al, 1985). As an example, VEP

responses, measured from two adult subjects (subject A and B), using square-wave stimulation, are depicted in Figure 3.1. These two subjects had normal or corrected to normal visual acuity, and no known ophthalmic disorder. Stimulus was a contrast reversing pattern with frequency 1 Hz and modulation depth $C_w = 50\%$. Response curves were obtained by averaging 64 records, which are depicted in the top row of the figure with the stimulus temporal function. Those averaged responses are further filtered by a digital lowpass filter with a cut-off frequency of 40 Hz. Then the even order harmonics with respect to the fundamental frequency 1 Hz were extracted by means of fast Fourier transform, and summed together to form "even order signals", which are depicted in the middle row. The "odd order signals" formed by the odd order harmonics are plotted in the third row.

It is seen that the signals formed by the even order harmonics present strong evoked potentials, while the signals formed by the odd order harmonics appear to be noise, which demonstrates that the VEP due to the stimulation of a contrast reversing pattern predominantly contains even order harmonics.

The rectification behavior can be attributed to spatial-temporal properties of the neural organization. Light information from the stimulus pattern is sensed by photoreceptors according to their receptive fields, and transmitted to the brain through parallel channels. For a contrast reversing pattern shown in Figure 2.2, the neurons contained in the network can be primarily divided into two groups which process the light information from the two sets of alternate segments. The stimulus pattern is radially symmetric so that it approximately matches the radially symmetric retina (Kandel, Schwartz & Jessell, 1991). The two parallel paths formed by these two groups of cells can be considered identical. During the periodic stimulation, each group of cells sense the same luminance function from the corresponding stimulus segments. Since one set of stimulus segments have a half-period time shift with respect to the other set. The responses generated from these two parallel paths are identical except for a half-period time shift. Since the nonlinear process exists in each pathway, the response produced in each pathway contains even order harmon-

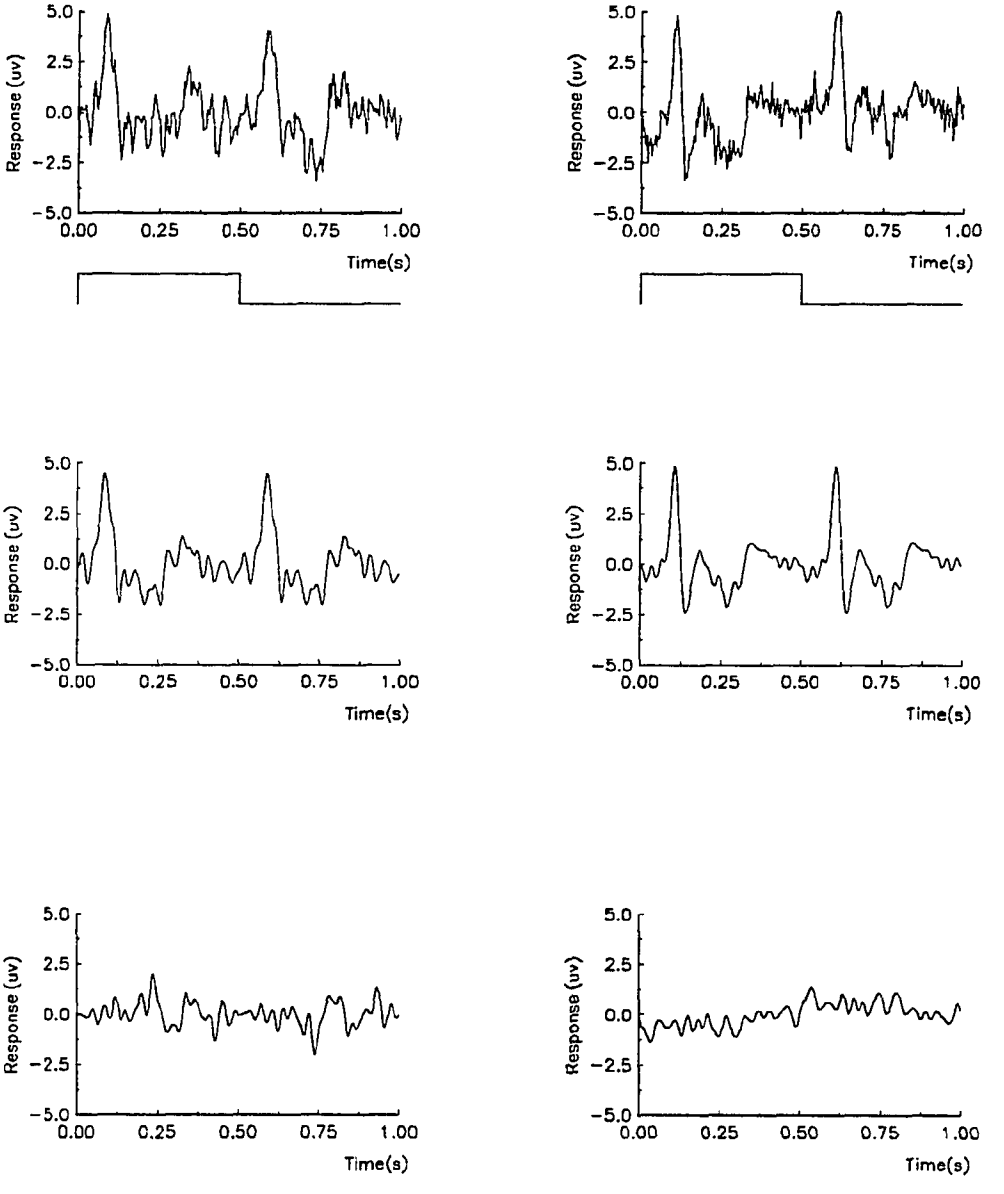

Figure 3.1 Square-wave responses recorded from subject A (left) and subject B (right). A stimulus of contrast reversed pattern with frequency 1 Hz and modulation depth $C_w = 50\%$ was used to elicit the VEP. Responses, obtained by averaging 64 records, are depicted in the top row. Those averaged responses are further filtered by a digital lowpass filter with cut–off frequency 40 Hz, and decomposed into two signals containing only even order harmonics (the middle row) and odd order harmonics (the bottom row) respectively. The result shows that the "even order signals" contain strong evoked potentials, while "odd order signals" appear as noise.

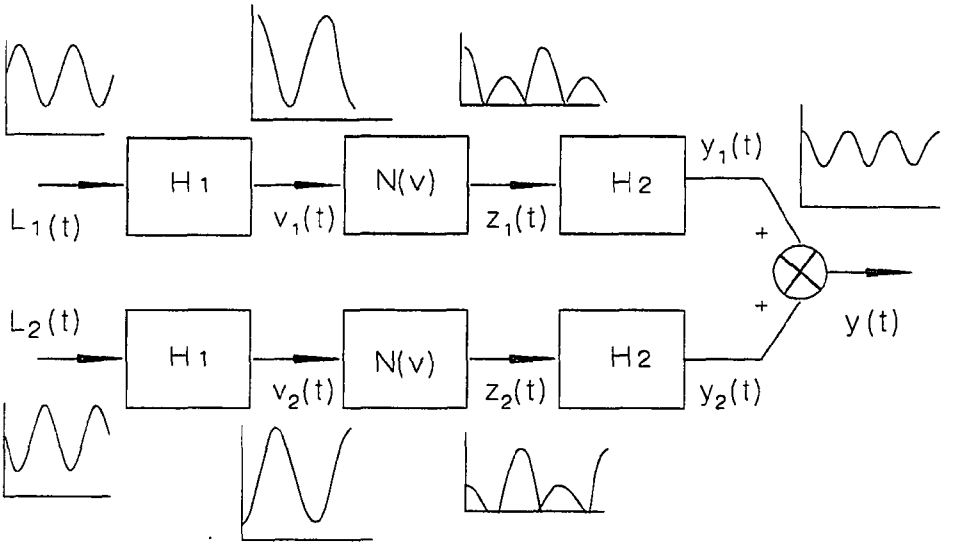

Figure 3.2 Demonstration of neuron message processing in the VEP pathways. Two groups of cells form two identical parallel paths to conduct the signals from the retina to the cortex, resulting an even order harmonic response. In the diagram, $N(v)$ can be any type of rectifier (e.g. symmetrical or asymmetrical, threshold or nonthreshold), which is responsible for generating harmonics.

ics. Those responses sum together in the cortex to form the VEP, in which, the even order harmonics sum up and the odd order harmonics cancel each other due to their half-period time shift. The VEP, therefore, presents an identical wave form in each half-period. A simple example of such neuronal processing procedure is illustrated in Figure 3.2.

In this example, each parallel path is simulated with a sandwich system; $L_1(t)$ and $L_2(t)$ are the luminance functions on the stimulus pattern, which, for demonstration purpose, are the sinusoids with 180 degree phase difference; $y(t)$ is the output of the system, and $y_1(t)$ and $y_2(t)$ are the outputs from the two identical parallel paths respectively; $N(v)$ can be any type of rectifier which produces even order harmonics. Since the sandwich system is time-invariant, $y_1(t)$ and $y_2(t)$ have a relative time shift of half period due to the time shift of the inputs. The output $y(t)$, summed from $y_1(t)$ and $y_2(t)$, contains only even order harmonics.

Because the two parallel pathways in Figure 3.2 are identical, they can be simply

combined into a single sandwich system with the input either defined by $L_1(t)$ or $L_2(t)$. The symmetrical full-wave rectification appears, therefore, to be a proper form of the nonlinear element in the sandwich system to produce even order harmonics.

On the other hand, from a system (other than physiological explanation) point of view, we would like to ask, if a asymmetrical full-wave rectifier is chosen, what effect will it cause on the identification of the linear elements H_1 and H_2? To analyze this issue, we expand the rectifier $N(v)$ into a series

$$N(v) = \sum_{k=0}^{\infty} a_k v^k \tag{3.2}$$

If the rectifier is asymmetric, the series above contains odd terms. One can prove (see Appendix A-I), odd terms will not produce sum and difference frequency components due to the two-sinusoid input, only even terms in the series (symmetrical portion) are capable of generating such intermodulation components. Since the identification goal is to find H_1 and H_2 for the model to fit the VEP sum and difference frequency component data, the choice of symmetric or asymmetric rectifier will have the same identification result.

2. Nonthreshold rectification

We mentioned in Section 1.4 that the major rectification process, located at the front stage of the cortex, results from large excitatory signal requirement to fire the stellate cells due to the inhibitory activity within the stellate cell layer. This process is simulated by a half-wave rectifier with a threshold as shown in Figure 1.3. As a cell's model, the threshold of each cell may differ from each other, which depends on the total inhibitory signals a cell receives. Since we desire to use a simply deterministic element to approximate the rectification behavior of overall network, we do the following treatment: We substitute the half-wave rectifier in Figure 1.3 for the nonlinearity $N(v)$ in Figure 3.2, and assume that the threshold of the rectifier V_T equals the average value of the input V_0 (see Figure 3.3.a). The scheme with identical parallel pathways can then be equivalently replaced by a single sandwich system with a nonthreshold full-wave rectifier depicted in Figure 3.3.b. The luminance function

$L(t)$, by definition, can be either $L_1(t)$ or $L_2(t)$ (we select $L(t) = L_1(t)$). Instead of the threshold to eliminate signal DC component, a block DC eliminator is placed at the beginning of the system to extract the input signal contrast.

The simplification above is based on the hypothesis that the mean value V_0 in the rectifier input matches the threshold V_T. The purpose of this treatment is merely to obtain a nonthreshold rectifier in the sandwich model, which is more convenient for analysis than a threshold rectifier. Indeed, the rectifier selection is not unique, A threshold rectifier can also be considered. However, since we lack any idea of how much the threshold should be to provide a better fit for the VEP data, such consideration is put into lower priority. In fact, previous research showed that a low contrast stimulus (2% contrast) can still elicit a detectable VEP response with even order harmonics (Zemon, Conte & Camisa 1986), which suggests that the rectification threshold may closely match signal average value. Therefore, if the stimulus used for the modeling is set with high contrast (say 30%), a tiny effect of the rectification threshold (if it exists) on the comparatively large signal contrast can be neglected.

3. Linear rectification

The quadratic function $z = v^2$ is the simplest form of the full-wave rectifier. Previous research found that the VEP response, elicited by a stimulus with luminance temporally modulated by a single sinusoid, contains second, fourth, and higher harmonics (Zemon et al, 1985). This finding suggests that the nonlinearity $N(v)$ in the VEP pathways can not be simply expressed as a quadratic function (a mechanism that squares the single sinusoid input merely generates the second harmonics). It must contain high power terms if expanded in a polynomial. The linear full-wave rectifier $z = |v|$ can be expanded in a high order series, and also is convenient for analysis in the time domain.

4. Other considerations

In Section 2.1, the sandwich model was described by a set of equations ((2.15), (2.16), (2.17)) under the general condition of a yet unspecified nonlinearity $z = N(v)$. These equations express the VEP sum and difference amplitudes and phase angles in

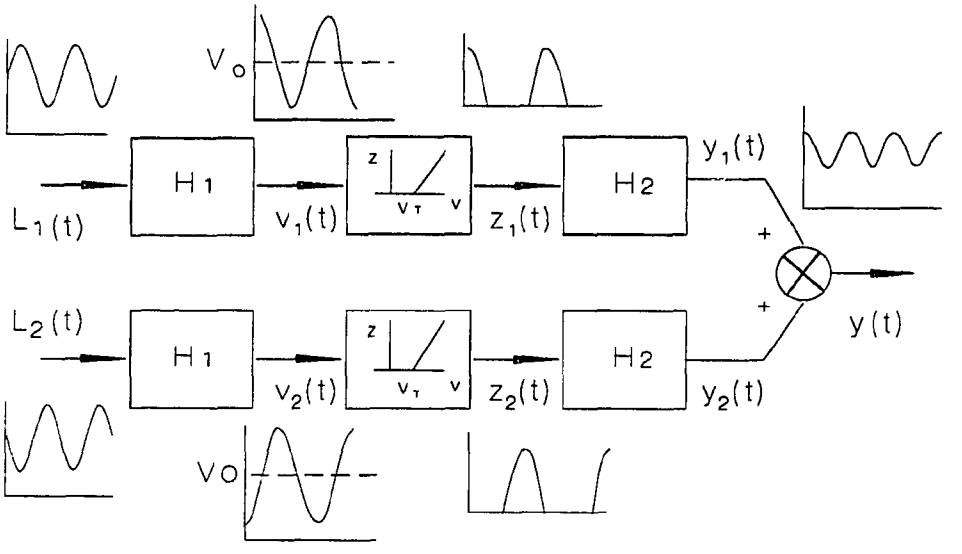

(a)

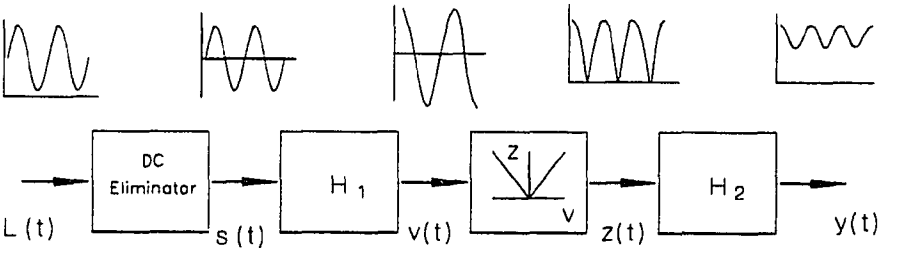

(b)

Figure 3.3 a: Two identical parallel pathways in the visual system sense the contrast reversed inputs, and results a summed output containing even order harmonics. **b:** Simplified diagram for the signal processing in (a) when $V_0 = V_T$.

terms of the linear transfer functions H_1 and H_2. The identification problem involves inversion of this set of equations to obtain H_1 and H_2 in terms of the VEP sum and difference amplitude and phase angles, for a given nonlinear function.

As discussed in Subsection 2.1.2, $|H_2|$, $\angle H_2$ and $\angle H_1$ can be obtained from (2.16) and (2.17), neither of which depend on the nonlinearity. Gain $|H_1|$ can be derived from (2.15a) which, however, does depend on the nonlinearity*. Thus, the choice of the nonlinearity affects only the identification of the gain characteristic of H_1.

Even though there is no proof that the linear full-wave rectifier is the best representation for the rectification mechanism involved in generating VEP, it can, at least, serve as a starting point for the system modeling.

Next, we note, equation (2.15a), describing the relation of DFC amplitude and the gain characteristic of H_1, is rather complicated. Identifying the transfer function of H_1 by using this equation is usually not practical. We, therefore, set up an approximate formula instead of (3.15a) to solve this problem.

$N(v)$ is expanded in a sixth order polynomial

$$N(v) = |v| \approx \sum_{k=0}^{6} a_k v^k \tag{3.3}$$

where a_k is a constant coefficient of the kth order term. Since the full-wave rectification is symmetrical about the vertical ordinate, the polynomial contains only even order terms. Least-square fitting yields $a_0 = 0.085$, $a_2 = 2.307$, $a_4 = -2.820$, $a_6 = 1.466$ for $|v| \leq 1$. The approximation diagram is illustrated in Figure 3.4.

For a given input of two sinusoids with amplitudes $A_v(f_1)$ and $A_v(f_2)$ to the rectifier, one can prove (see Appendix A-II) that the amplitude of difference frequency component and sum frequency component is†

$$\begin{aligned} A_{zDFC}(f_1, f_2) &= A_{zSFC}(f_1, f_2) = \Gamma[A_v(f_1), A_v(f_2)] \\ &\approx a_2 \frac{A_v(f_1)A_v(f_2)}{A_v(f_1) + A_v(f_2)} + \frac{3}{2} a_4 \frac{A_v^3(f_1)A_v(f_2) + A_v(f_1)A_v^3(f_2)}{(A_v(f_1) + A_v(f_2))^3} \\ &+ \frac{15}{8} a_6 \left[\frac{A_v^5(f_1)A_v(f_2) + A_v(f_1)A_v^5(f_2) + 3A_v^3(f_1)A_v^3(f_2)}{(A_v(f_1) + A_v(f_2))^5} \right] \end{aligned} \tag{3.4}$$

*(2.15) contains the term $F(ju)$ which is the Fourier transform of the nonlinear function $N(v)$.

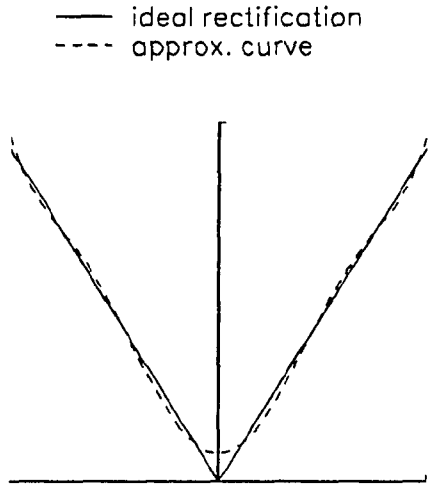

Figure 3.4 Approximation of full-wave linear rectifier by a sixth order polynomial

Table 1 Comparison of the DFC amplitude calculated from approximating method and from numerical method.

amplitudes $A_v(f_1) : A_v(f_2)$	results from polynomial approximation	results from numerical method	error
9 : 1	0.638	0.626	2%
8 : 2	1.236	1.250	-1%
7 : 3	1.889	1.832	3%
6 : 4	2.422	2.362	2.5%
5 : 5	2.628	2.694	-2.5%

To ensure that the error caused by the sixth order polynomial approximation is within a tolerable range for modeling purpose, amplitude of difference frequency component, obtained from the polynomial approximation (calculated by (3.4)) and from the actual full-wave rectifier (calculated by numerical method[‡]) were compared. The results are listed in Table 1. Five pairs of two-sinusoids with different amplitude

[†]To obtain (3.4), the input to the rectifier has been normalized to ensure that the magnitude of the signal entering the rectifier is not greater than one.

[‡]The numerical calculation for the intermodulation components was carried out by taking the Fourier transform for the rectifier response due to the two-sinusoid input. The procedure was implemented by computer.

ratio applied to the rectifier. The first column in the table lists the amplitudes of the two sinusoids. the second column lists the results calculated from equation (3.4), the numerical solutions are listed in column three, the relative errors with respect to the data obtained by numerical method are listed in the fourth column. The maximum error of 3% suggests that the sixth order polynomial approximation most likely satisfies the accuracy requirement of VEP modelling.

According to (3.4), for a given two-sinusoid input with amplitude C_w to the system, we have $A_v(f_1) = C_w|H_1(f_1)|$ and $A_v(f_2) = C_w|H_1(f_2)|$. It gives

$$A_{zDFC}(f_1, f_2) = A_{zSFC}(f_1, f_2) = \Gamma[C_w|H_1(f_1)|, C_w|H_1(f_2)|]$$

$$\begin{aligned} &= C_w\Gamma[|H_1(f_1)|, |H_1(f_2)|] \\ &\approx C_w\left\{a_2\frac{|H_1(f_1)||H_1(f_2)|}{|H_1(f_1)| + |H_1(f_2)|} + \frac{3}{2}a_4\frac{|H_1(f_1)|^3|H_1(f_2)| + |H_1(f_1)||H_1(f_2)|^3}{(|H_1(f_1)| + |H_1(f_2)|)^3}\right. \\ &\quad \left. +\frac{15}{8}a_6\left[\frac{|H_1(f_1)|^5|H_1(f_2)| + |H_1(f_1)||H_1(f_2)|^5 + 3|H_1(f_1)|^3|H_1(f_2)|^3}{(|H_1(f_1)| + |H_1(f_2)|)^5}\right]\right\} \end{aligned} \quad (3.5)$$

The amplitude of difference and sum frequency components from the entire system are, respectively

$$A_{yDFC}(f_1, f_2) = |H_2(f_2 - f_1)|\Gamma[C_w|H_1(f_1)|, C_w|H_1(f_2)|] \quad (3.6a)$$

$$A_{ySFC}(f_1, f_2) = |H_2(f_1 + f_2)|\Gamma[C_w|H_1(f_1)|, C_w|H_1(f_2)|] \quad (3.6b)$$

Equations (3.5), (3.6a) and (3.6b) can be used to calculate the amplitude of the intermodulation components. Those equations, together with (2.16) and (2.17), form a set of basic equations to identify the transfer functions of the linear elements H_1 and H_2.

3.2 Intermodulation Components in VEP

To find appropriate equation forms for the transfer functions, a sample of ten normal adult subjects was utilized to obtain VEP difference and sum frequency components

(DFC and SFC). The "normal" means the subject had normal or corrected to normal acuity and no known ophthalmic disorder. An experiment was carried out under the conditions mentioned in Section 2.2. Two-sinusoid stimulation was used. The frequency separation $f_2 - f_1$ was maintained at 1.99 Hz for each test. A total of eight pairs of frequencies were used, among which, f_1 ranged from 1.22 Hz to 29.92 Hz. The frequency pairs were selected such that there were no other frequency components that overlapped the difference frequency components (DFC) and sum frequency frequency components (SFC). The mean luminance of the stimuli was maintained at 150 cd/m^2, and the peak contrast of each sinusoid was set to 30%. Each test ran 32.08 seconds with 16.384 sampling points. Two subjects A and B were tested in this work. DFC and SFC data are obtained by Fourier transform applied to the VEP recording. Data averaged over four tests, together with the radii of *error circles* and error range of phase (see description in Section 2.4), are plotted in Figure 3.5.1 (for subject A) and 3.5.2 (for subject B).

In each figure, The top left is amplitude of the DFC versus f_1, the bottom left is phase angle of the DFC versus f_1, the top right is amplitude of the SFC and amplitude ratios of the SFC and the DFC versus $f_1 + f_2$, and the bottom right is phase angle of the SFC versus $f_1 + f_2$. Data from other eight subjects, measured previously at the Biophysics Laboratory, Rockefeller University, are also plotted in Figure 3.6.1 (amplitude of DFC), 3.6.2 (phase angle of DFC), 3.6.3 (amplitude ratio of DFC and SFC), and 3.6.4 (phase angle of SFC). Each test for collecting those data run one minute with a total of 16384 sampling points. Other test conditions were the same as those mentioned above except for different number of frequency pairs used.

Although the data in Figure 3.6 were obtained by measuring the responses from each subject only once for each condition, tests in this laboratory showed that the sum and difference frequency components, derived from the Fourier transform for the data recorded over the period of one minute, can be effectively recovered from noise, and are repeatable in the sense of response curve shape. Therefore, the data in Figure 3.6, at least, can qualitatively reflect some features of the VEP frequency responses.

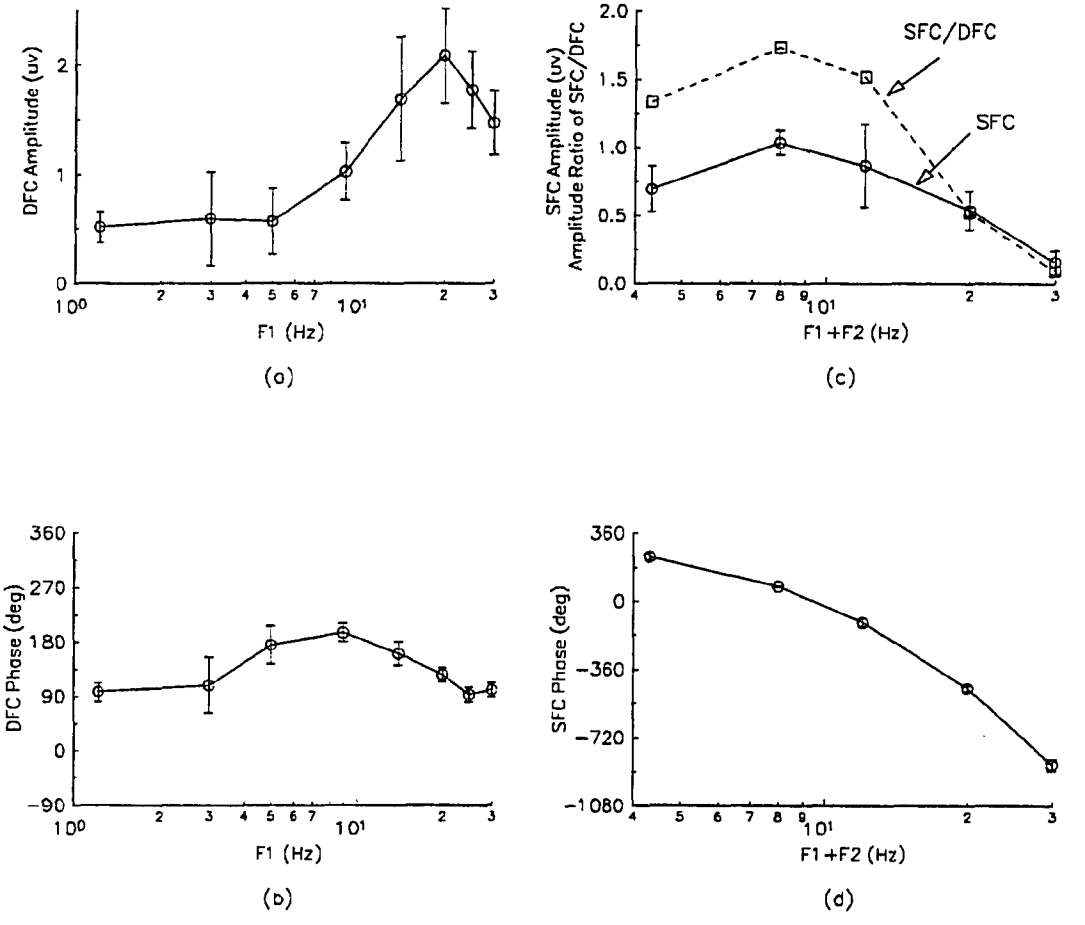

Figure 3.5.1 Tests of two-sinusoid stimuli for subject A. The difference between f_1 and f_2 was kept at 1.99 Hz. The sampling frequencies f_1 were set to 1.22, 2.99, 4.99, 8.98, 13.96, 19.95, 24.93 and 29.92 Hz. The test was carried out at two different times. Each time, the test was repeated twice. The stimuli were first presented in ascending order from low sampling frequency to high sampling frequency, and then in descending order. The data collected from four measures are averaged. Amplitudes are plotted with the radii of *error circles*, phases are plotted with their error ranges. (a)–amplitude of DFC, (b)–phase angle of DFC, (c)–amplitude of SFC (marked by circles) and amplitude ratio of SFC and DFC (marked by boxes), and (d)–phase angle of SFC.

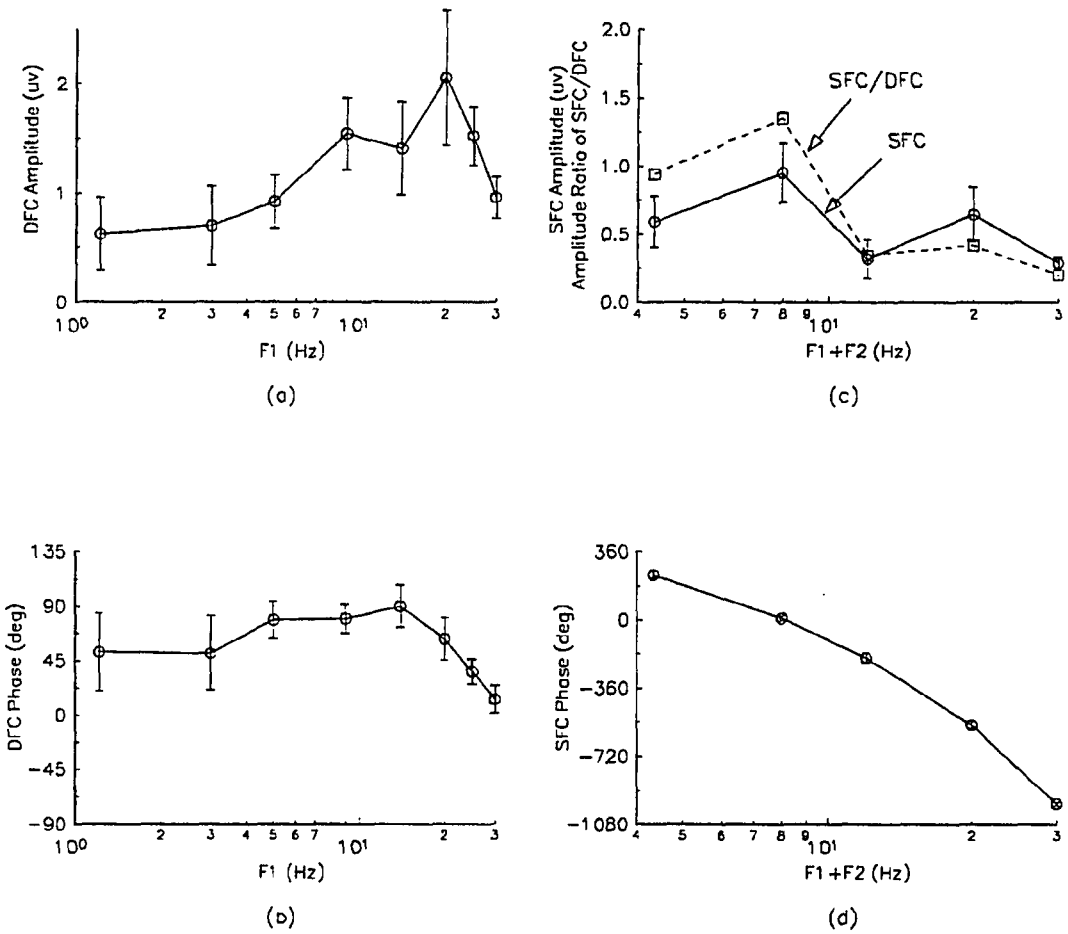

Figure 3.5.2 Tests of two-sinusoid stimuli for subject B. The difference between f_1 and f_2 was kept at 1.99 Hz. The sampling frequencies f_1 were set to 1.22, 2.99, 4.99, 8.98, 13.96, 19.95, 24.93 and 29.92 Hz. The test was carried out at two different times. Each time, the test was repeated twice. The stimuli were first presented in ascending order from low sampling frequency to high sampling frequency, and then in descending order. The data collected from four measures are averaged. Amplitudes are plotted with the radii of *error circles*, phases are plotted with their error ranges. (a)–amplitude of DFC, (b)–phase angle of DFC, (c)–amplitude of SFC (marked by circles) and amplitude ratio of SFC and DFC (marked by boxes), and (d)–phase angle of SFC.

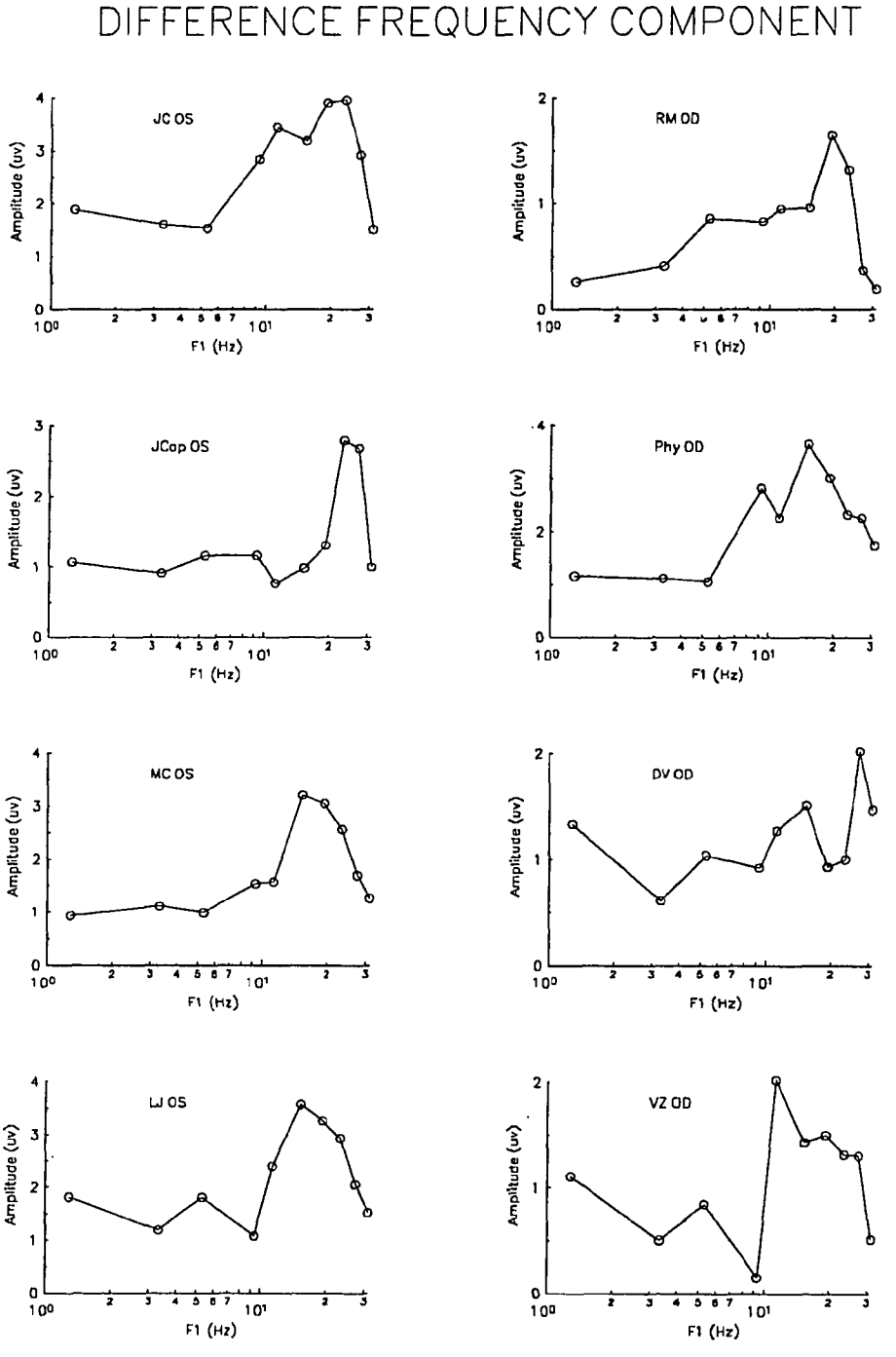

Figure 3.6.1 VEP amplitude of difference frequency components, collected from eight normal adult subjects using two-sinusoid stimuli. The frequency sampling points were set to f_1=1.29, 3.30, 5.31, 9.31, 11.29, 15.31, 19.30, 23.30, 27.29 and 31.32 Hz. The separation between f_1 and f_2 was maintained at 1.99 Hz. Data are plotted versus f_1.

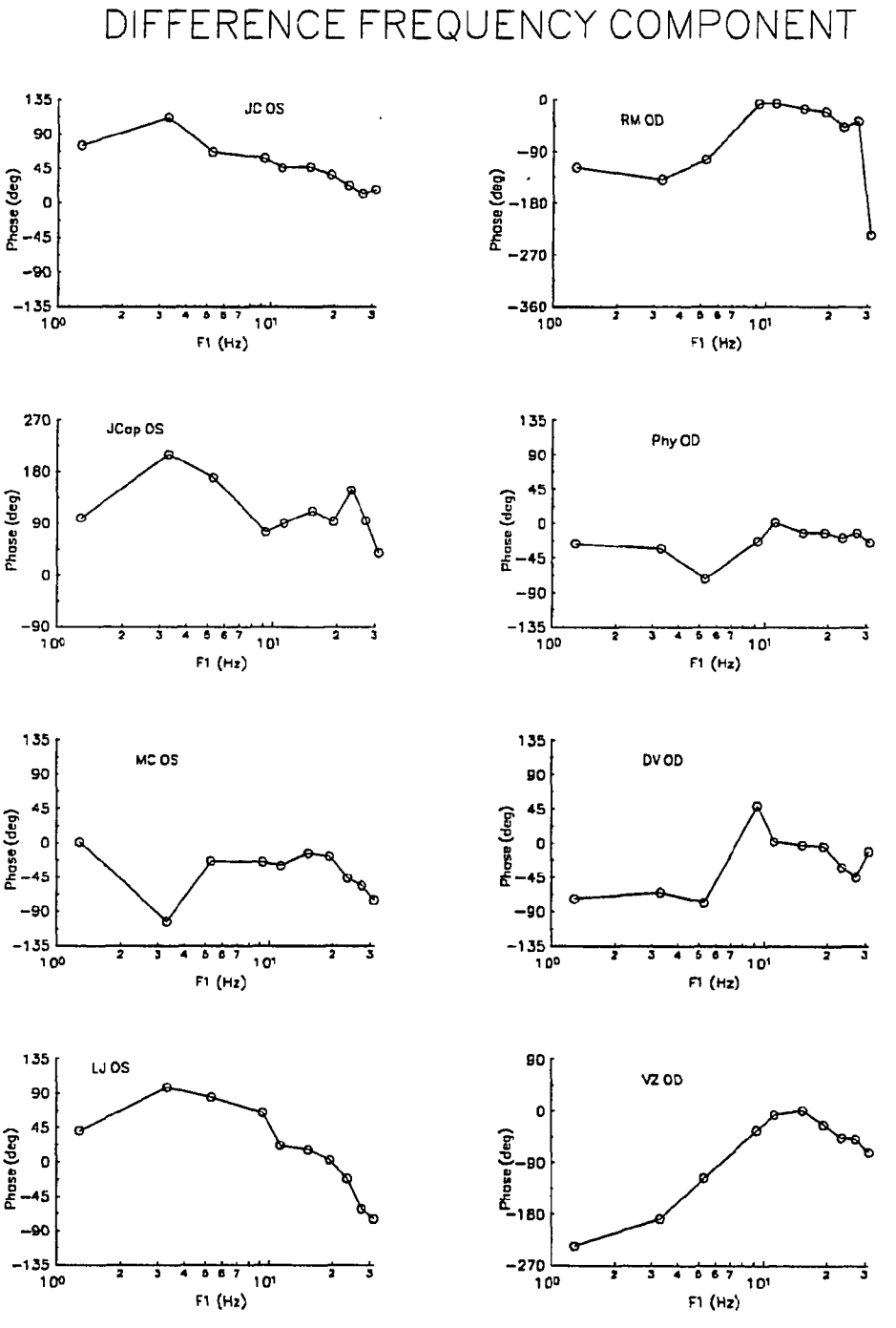

Figure 3.6.2 VEP phase angle of difference frequency components, collected from eight normal adult subjects using two-sinusoid stimuli. The frequency sampling points were set to f_1=1.29, 3.30, 5.31, 9.31, 11.29, 15.31, 19.30, 23.30, 27.29 and 31.32 Hz. The separation between f_1 and f_2 was maintained at 1.99 Hz. Data are plotted versus f_1.

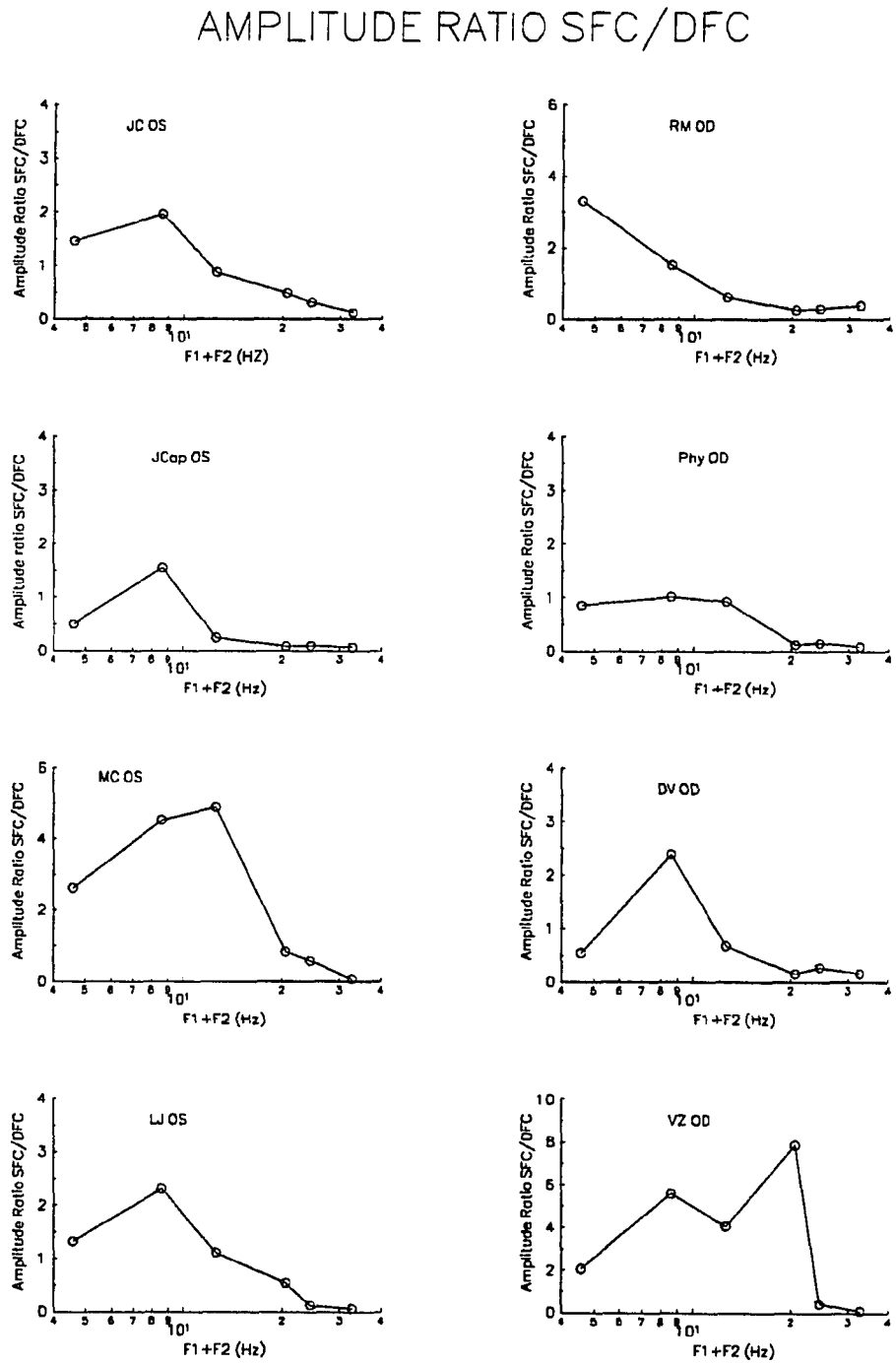

Figure 3.6.3 VEP amplitude ratio of sum frequency components and difference frequency components, collected from eight normal adult subjects using two-sinusoid stimuli. The frequency sampling points were set to f_1=1.29, 3.30, 5.31, 9.31, 11.29, 15.31 Hz. The separation between f_1 and f_2 was maintained at 1.99 Hz. Data are plotted versus $f_1 + f_2$.

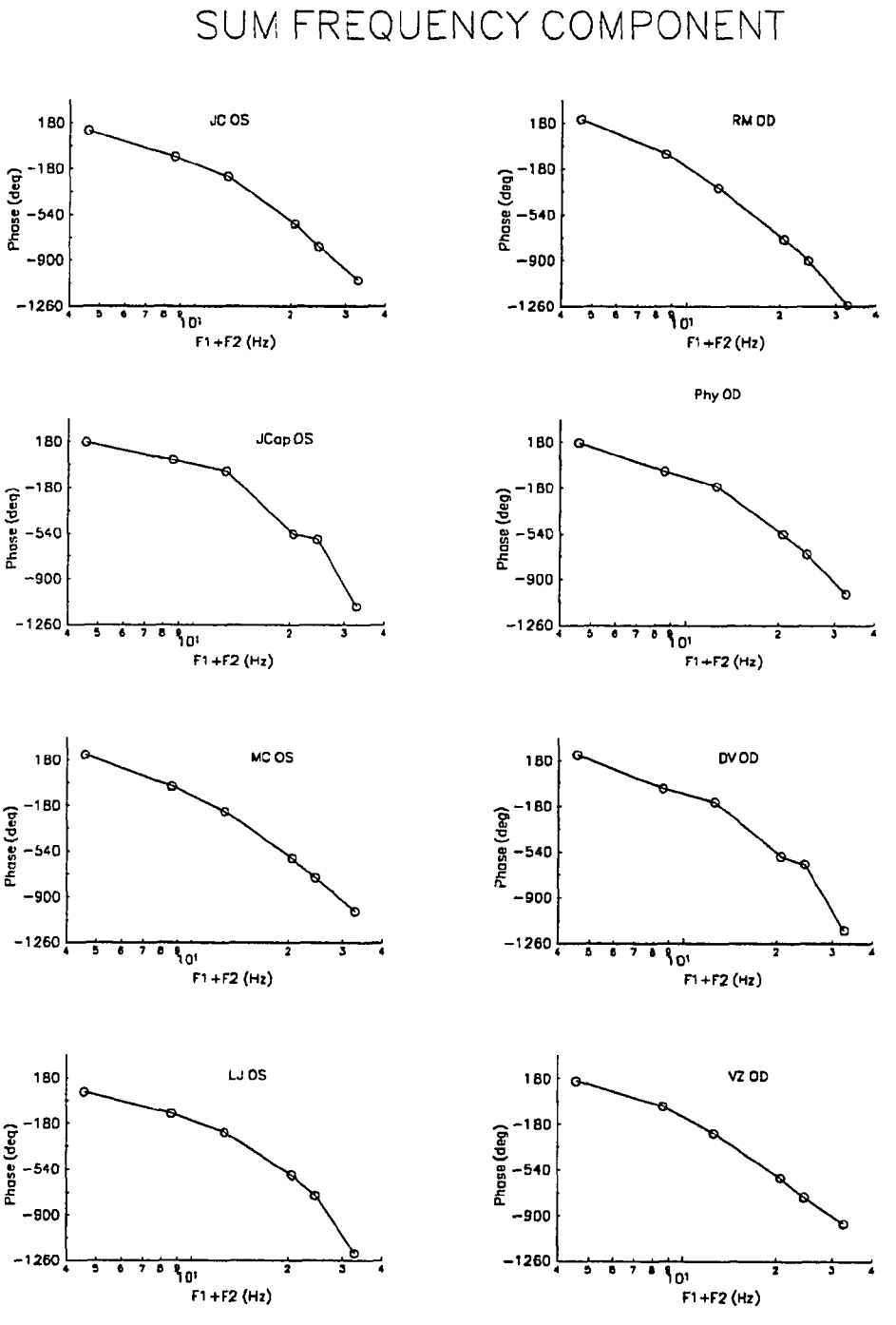

Figure 3.6.4 VEP phase angle of sum frequency components, collected from eight normal adult subjects using two-sinusoid stimuli. The frequency sampling points were set to f_1=1.29, 3.30, 5.31, 9.31, 11.29, 15.31 Hz. The separation between f_1 and f_2 was maintained at 1.99 Hz. Data are plotted versus $f_1 + f_2$.

The data in Figure 3.5 and 3.6 essentially present the following features:

1. The amplitude response of the DFC has relatively large values at frequencies above 10 Hz in comparison with the values at frequencies below 10 Hz. It has a peak around $f_1 = 20$ Hz, and decreases rapidly as f_1 increases beyond this point.

2. For the phase of the DFC, although differences exist among the subjects, a consistency is found in the high frequency region for most subjects. The phase angle essentially decreases as f_1 increases for the frequencies higher than 15 Hz.

3. The amplitude ratios of the SFC to the DFC, representing the normalized gain characteristic of H_2, present a comparatively large gain around 9 Hz, and a rapid decrease when the frequency $f_1 + f_2$ is higher than this turning point.

4. The phase function of the SFC exhibits a negative, steep slope, representing the sum of phase shifts contributed from both H_1 and H_2.

The above description for the VEP responses will be used to determine the type of transfer function. Although there are some quantitative differences between each individual subject's data, the major qualitative features described above exist in most subjects' VEP responses. For the phase data, all the phase responses of the SFC match our description; two subjects (JCap OS and VZ OD) have phase response of the DFC not consistent with the description above, one has a narrow frequency region above 20 Hz on which the decrease occurs, the other has a large increase at frequency 30 Hz. With regard to the amplitude data, two subject (DV OD and VZ OD) have significant differences in DFC amplitude, one presents two peaks in the high frequency region, the other has a large value in the low frequency region; two subjects (RM OD and VZ OD) have amplitude responses of the SFC departing from the description above, one has no peak and the other has a peak far from 9 Hz. Those deviations may result from large noise, or from specific characteristics of the individual visual system.

The above description is based on the data collected from a group of ten subjects. which contain a total of 464 measures (sum and difference frequency components, amplitude and phase angle). Those ten subjects responses can be utilized for prediction of large population's VEP. Statistical analysis presented in Appendix B-I gives 95% confidence that the VEP responses (DFC and SFC) collected from at least 53% normal population possess the features described above.

3.3 Discussion of Sandwich Model Fits

In this section, we discuss i) the type of transfer function for the linear elements H_1 and H_2, ii) the comparison of the function type with prior investigation of temporal characteristics of the visual system. and iii) the reason to improve the sandwich model.

3.3.1 Types of Transfer Functions

We have collected the VEP data and established the system equations. Now they can serve as a rule to assess the sandwich model.

Because the separation of the frequency pair f_1 and f_2 is small (only 2 Hz), two sinusoids will be almost identically filtered by H_1 when f_1 and f_2 are sufficiently high (say higher than 15 Hz). In this case, for the input containing two sinusoids with same amplitude and phase, the output of H_1 also contains two sinusoids with nearly identical amplitude and phase. According to (3.4), the amplitude of DFC produced from the rectifier

$$\begin{aligned} A_{zDFC}(f_1, f_2) &= \Gamma[A_v(f_1), A_v(f_2)] \approx \Gamma[A_v(f_1), A_v(f_1)] \\ &\approx \frac{1}{2}a_2 A_v(f_1) + \frac{3}{2}a_4 \frac{2A_v^4(f_1)}{8A_v^3(f_1)} + \frac{15}{8}a_6 \frac{5A_v^6(f_1)}{32A_v^5(f_1)} \\ &= 0.525A_v(f_1) = 0.525C_w|H_1(f_1)| \end{aligned} \tag{3.7a}$$

The amplitude of the DFC produced from the entire system then becomes

$$A_{yDFC}(f_1, f_2) = A_{zDFC}(f_1, f_2)|H_2(f_2 - f_1)|$$

$$\approx 0.525 C_w |H_1(f_1)||H_2(f_2 - f_1)| \tag{3.7b}$$

Because the second linearity H_2 only offers a constant gain and phase to the difference frequency components when $f_2 - f_1$ is a constant, equation (3.7) indicates that the DFC produced from the sandwich system is approximately proportional to the gain characteristic of H_1. Thus, the DFC components, presenting a peak in amplitude around 20 Hz, implies that H_1 is a bandpass filter with maximum gain around 20 Hz.

The gain characteristic of H_2, reflected by the amplitude ratios of SFC and DFC, presents a bandpass character with maximum gain around 9 Hz.

The phase response of DFC only depends on the first linear filter H_1 with the dependence (from equation (2.16a))

$$\phi_{yDFC}(f_1, f_2) = \angle H_1(f_2) - \angle H_1(f_1) + \text{constant} \tag{3.8}$$

Because the phase response results from the difference, rather than the sum, of $\angle H_1(f_1)$ and $\angle H_1(f_2)$, one can expect that the DFC phase variation is much smaller than that of SFC, which is the sum of phase shift of $\angle H_1(f_1)$, $\angle H_1(f_2)$ and $\angle H_2(f_1+f_2)$. This expectation is consistent with the data shown in Figure 3.5 and 3.6. On the other hand, as mentioned above, the two sinusoids produced by H_1 are nearly identical when f_1 and f_2 are reasonably high. In that case, one may expect that $\angle H_1(f_1)$ and $\angle H_1(f_2$ in (3.8) become close to each other, and the phase response of DFC from the entire system will approach a constant. However, the phase response curve of the DFC, presenting a negative slope in the high frequency region, conflicts with this expectation.

To examine this problem, we consider below, separately, three different types of transfer functions of H_1, namely, i) H_1 is a minimum phase function, ii) H_1 contains time-delay term, and iii) H_1 is a non-minimum phase function containing zeros in the right half s-plane.

1. H_1 is a minimum phase function which contains neither poles nor zeros in the right half s-plane. In this case, there is a unique relationship between the gain

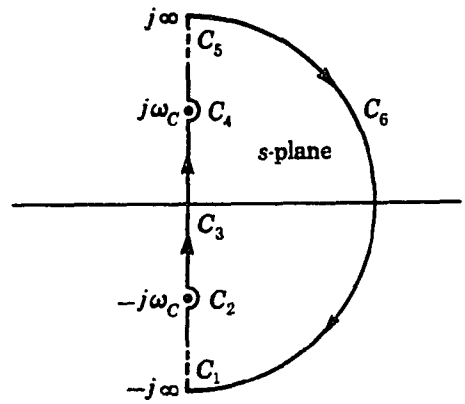

Figure 3.7 The integration contour in the s-plane for determination of the relation between gain and phase of a transfer function.

and phase characteristics (Bode, 1945). This relation can be obtained by integrating $\frac{\ln H_1(s)-\ln|H_1(j\omega_c)|}{s^2+\omega_c^2}$ around the right-hand half-plane as indicated in Figure 3.7, which yields*

$$\angle H_1(j\omega_c) = \frac{2\omega_c}{\pi}\int_0^\infty \frac{\ln|H_1(j\omega)| - \ln|H_1(j\omega_c)|}{\omega^2-\omega_c^2}d\omega \tag{3.9}$$

This equation gives the phase of $H_1(j\omega)$ at an any arbitrary frequency ω_c in terms of the integral of $\ln|H_1(j\omega)|$ over the range of all positive real frequencies.

If we define

$$A \doteq \ln|H_1(j\omega)| \tag{3.10a}$$

and

$$u \doteq \ln\frac{\omega}{\omega_c} \tag{3.10b}$$

then, the expression (3.9) can be transformed to (Bode, 1945)

$$\angle H_1(j\omega_c) = \frac{\pi}{2}\left(\frac{dA}{du}\right)_{\omega=\omega_c} + \frac{1}{\pi}\int_{-\infty}^{+\infty}\left[\frac{dA}{du} - \left(\frac{dA}{du}\right)_{\omega=\omega_c}\right]\ln\coth\left|\frac{u}{2}\right|du \tag{3.11}$$

Thus, it is seen that the phase shift at any frequency is composed of two parts. The first contribution to the phase is directly proportional to the slope of the gain

*Note that the integral on the right-hand side of (3.9) is the Cauchy principal value of the integral (i.e. the limit of the sum of the integrals around C_1, C_3 and C_5 in Figure 3.7 as the radii of C_2 and C_4 approach zero and C_6 approaches infinity).

characteristic at the frequency at which the phase is sought, and the second contribution is proportional to the weighted integral of the difference in slope of the gain characteristic from the value of this slope at the desired frequency. The weighting factor

$$\ln \coth \left|\frac{u}{2}\right| = \ln \frac{e^{|u|/2} + e^{-|u|/2}}{e^{|u|/2} - e^{-|u|/2}} = \ln \left|\frac{\omega + \omega_c}{\omega - \omega_c}\right| \tag{3.12}$$

has a large value when ω closes to ω_c, and approaches zero when ω goes away from ω_c. For this reason, if the slope of the gain characteristic is fairly constant over a rather limited range of frequencies about ω_c, a good approximation to the phase $\angle H_1(j\omega)$ is $(\pi/2)(dA/du)$ radians.

The above result provides a theoretical basis for examining the possibility of fit for H_1 within the minimum phase function category. Because the amplitude response of the DFC above 10 Hz essentially resembles the gain characteristic of H_1 (see (3.7)), and below 10 Hz. its rather flat curve implies the flat gain characteristic of H_1 in that low frequency region, hence, instead of the gain characteristic of H_1, the amplitude response curve of the DFC can be used to determine the phase characteristic of H_1 in terms of (3.11). If the phase characteristic of H_1 determined by such a method can result in $\angle H_1(f_2) - \angle H_1(f_1)$ matching the phase data of DFC, which presents a negative slope in the high frequency region, one may find a minimum phase transfer function $H_1(s)$ which fits both amplitude and phase of the DFC at same time, otherwise, there is no minimum phase function existing for H_1.

The amplitude data of the DFC recorded from subjects A and B, displayed in the top row of Figure 3.8, have been smoothed by a local-weighted regression curve using Axum*(TriMetrix, Inc., Seattle, WA). The corresponding phase characteristic $\angle H_1(f)$ derived by (3.11) is presented by dotted curve in the second row of Figure 3.8. Since we concentrate on the analysis of the phase characteristic in the high frequency region, only the curves above 9 Hz are displayed. The integral in (3.11) is carried out over the frequency region from 1.22 Hz to 200 Hz. Since near the

*This is not curve fitting for searching the transfer function, it is merely a signal curve fitting to obtain an approximating gain characteristic curve of H_1, which will be utilized to determine the phase characteristic of H_1

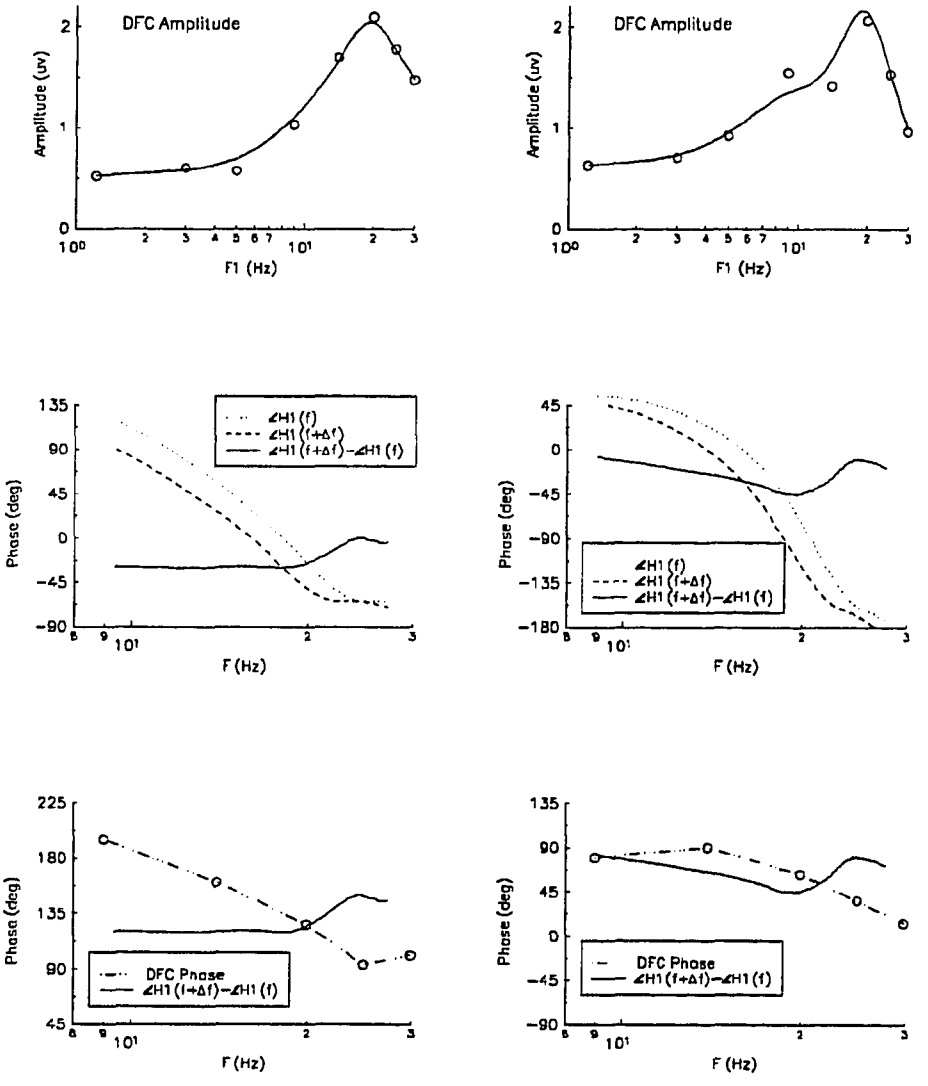

Figure 3.8 Phase characteristic of H_1 determined from its gain characteristic by relation (3.11). The left column is for subject A, and the right column is for subject B. The top row shows the VEP amplitude response of the DFC and their local-weighted regression fitting curves which approximate the gain characteristics of H_1. The second row shows the phase characteristic $\angle H_1(f)$ in dots and $\angle H_1(f+\Delta f)$ in dash (Δf =2 Hz). These phase curves are determined by (3.11) from the regression fitting curves in the top row. The difference curves $\phi_{yDFC}(f, f+\Delta f) = \angle H_1(f+\Delta f) - \angle H_1(f)$ are also shown in the second row in solid. The third row shows the difference curve $\phi_{yDFC}(f, f+\Delta f)$ with the phase data of the DFC for comparison.

frequency 30 Hz, the gain slope of H_1 nearly reaches a constant, the slope dA/du above 30 Hz are assigned the value of dA/du at 30 Hz. As mentioned before, the frequencies below 1.22 Hz and above 200 Hz are remote from the frequency region we are considering, the contributions of the integration from those regions can be neglected due to small weighting factor $\ln \coth |\frac{u}{2}|$. In the second row of Figure 3.8, phase curves $\angle H_1(f + \Delta f)$ (Δf =2 Hz) are displayed in dashes, and the difference curves $\phi_{yDFC}(f, f + \Delta f) = \angle H_1(f + \Delta f) - \angle H_1(f)$ are in solid. These difference curves are also plotted in the third row of the figure together with the phase data of the DFC measured from subjects A and B. For easier comparison, $\phi_{yDFC}(f, f + \Delta f)$ in the third row are vertically shifted to superimpose the VEP phase data.

The result in the third row of Figure 3.8 shows that the difference curves $\phi_{yDFC}(f, f + \Delta f)$ (solid) do not match the phase responses of the DFC in shape, recorded from either of the two subjects. Similar result is expected from the data measured from the other eight subjects due to their similar features that the DFC amplitude has a peak around 20 Hz and the phase decreases as the frequency increases in the region above 15 Hz. An apparent reason of this unfitness is: For a small separation between f_1 and f_2, the variation of the DFC phase response $\phi_{yDFC}(f_1, f_2) = \angle H_1(f_2) - \angle H_1(f_1)$ is small as f_1 and f_2 change, which is shown about 45^0 in the second row of Figure 3.8. The DFC phase data measured from most of the subjects, however, have a variation range about 90^0 in the region above 10 Hz. Therefore, we conclude that a minimum phase function can not fit the DFC amplitude and phase data.

2. H_1 contains a constant time delay. The time-delay term $\exp^{-sT}$ in H_1, according to (3.8), will add a constant term to the phase response of DFC

$$\Delta\phi_{yDFC}(f_1, f_2) = -2\pi f_2 T + 2\pi f_1 T = -2\pi T(f_2 - f_1) \tag{3.13}$$

which does not contribute a negative slope in $\phi_{yDFC}(f_1, f_2)$. Therefore, the constant time delay in the transfer function will not give any help to fit the DFC phase data.

3. H_1 is a non-minimum phase function. To satisfy the stability requirement,

H_1 must have no poles in the right half s-plane. If H_1 contains zeros in the right half s-plane, then the transfer function can be expressed as

$$H_1(s) = \frac{\prod_{i=1}^{M}(s-b_i)N(s)}{D(s)} = \frac{\prod_{i=1}^{M}(s+b_i)N(s)}{D(s)} \frac{\prod_{i=1}^{M}(s-b_i)}{\prod_{i=1}^{M}(s+b_i)} = H_{11}(s)H_{12}(s) \quad (3.14)$$

In the above equation, b_i are the zeros in the right half s-plane, M is the number of those zeros, $N(s)$ and $D(s)$ are the numerator polynomial and denominator polynomial respectively, and

$$H_{11}(s) = \frac{\prod_{i=1}^{M}(s+b_i)N(s)}{D(s)} \quad (3.15a)$$

$$H_{12}(s) = \frac{\prod_{i=1}^{M}(s-b_i)}{\prod_{i=1}^{N}(s+b_i)} \quad (3.15b)$$

It is seen that $H_1(s)$ is composed of two parts, H_{11} and H_{12}. H_{11} is a minimum phase function which fits the DFC amplitude data, but is not able to fit the DFC phase data. H_{12} has a unit gain characteristic, and only offers a phase shift to the system. Thus, H_{12} serves as a phase compensator which provides a possibility to fit the DFC phase data.

Now, if H_1, a non-minimum phase function can fit the DFC data, what the phase characteristic of H_1 should look like? Since the phase compensator H_{12} decreases in phase as the frequency increases, the phase characteristic of H_{11}, a minimum phase function, has a negative slope in the region above 15 Hz (see the middle row plots in Figure 3.8), the phase characteristic of H_1, which is a combination from the phase characteristic of H_{11} and H_{12}, thus, has a negative slope in the region above 15 Hz.

Now, if we substitute $f_1 + \Delta f$ for f_2 in equation (3.8), and take the derivative of the equation with respect to f_1, we obtain

$$\frac{d\phi_{yDFC}(f_1, f_1+\Delta f)}{df_1} = \frac{d\angle H_1(f_1+\Delta f)}{df_1} - \frac{d\angle H_1(f_1)}{df_1} \quad (3.16)$$

Since the plot of $\phi_{yDFC}(f_1, f_1+\Delta f)$ versus f_1 essentially presents a negative slope in the high f_1 region, so $\frac{d\phi_{yDFC}(f_1,f_1+\Delta f)}{df_1}$ is negative, and

$$\frac{d\angle H_1(f_1+\Delta f)}{df_1} - \frac{d\angle H_1(f_1)}{df_1} < 0 \qquad \text{for a reasonably large } f_1 \quad (3.17)$$

Because phase slope $\frac{d\angle H_1(f_1)}{df_1}$ and $\frac{d\angle H_1(f_1+\Delta f)}{df_1}$ are negative. One can obtain from equation (3.17) that the absolute value of $\frac{d\angle H_1(f_1+\Delta f)}{df_1}$ is bigger than that of $\frac{d\angle H_1(f_1)}{df_1}$, or, in other words, the phase slope of H_1 at $f_1 + \Delta f$ is steeper than the slope at f_1.

The discussion above leads to a conclusion: *To fit the DFC components measured from the ten subjects, the transfer function of H_1 must contain zeros in the right half s-plane. Its amplitude characteristic is a bandpass with maximum gain around 20 Hz, and its phase characteristic has such a property that the slope becomes steeper as the frequency increases in the region above 15 Hz.*

How is the conclusion above affected if another type of nonlinearity, $N(v)$, is chosen for the sandwich model?

We note that the above conclusion is derived based on equations (3.7) and (3.8). Equation (3.8). the relation between the phase characteristic H_1 and phase response of DFC observed from the system, holds for any static nonlinearity, while equation (3.7). the relation between the gain characteristic of H_1 and the amplitude of DFC produced from the rectifier, was obtained under the condition that the rectifier is full-wave. Equation (3.7) indicates: The full-wave rectifier has a property such that, when the two sinusoids applied to the rectifier have identical amplitude, the amplitude of DFC produced by the rectifier or observed for the entire system is proportional to the amplitude of the rectifier input, and thus, proportional to the gain characteristic of H_1.

This property of the full-wave rectifier can be observed in the VEP test using two-sinusoid stimulation with variable contrast. As mentioned before, for a reasonably high frequency pair, f_1 and f_2, the two sinusoids in the rectifier input, which have been nearly identically filtered by H_1, have nearly identical amplitude, and this amplitude is proportional to the stimulus contrast. Previous research (Zemon, Conte & Camisa, 1987) and the experiment conducted in the current work (Section 4.2) showed that, when the frequency is above 20 Hz, the amplitude of the DFC elicited by two-sinusoid stimulation monotonically increases as stimulus contrast increases. Therefore, if another type of rectifier is selected (e.g. threshold or nonlinear rectifier),

to match the physiological phenomena, it must also possess the property that, for the input containing two sinusoids with identical amplitude, the amplitude of the DFC produced by that rectifier is proportional to the amplitude of the rectifier input (we call this "physiological-evidence based selection"). If this condition is satisfied, the amplitude of the DFC elicited by two-sinusoid stimulation resembles the gain characteristic of H_1 in the high frequency region. Therefore, physiologica-evidence based selection for the type of nonlinearity will not substantially affect the above conclusion.

3.3.2 Linear Process before the Cortex–Minimum Phase or Non-Minimum Phase Function?

Prior investigation of temporal characteristics of visual system included single neuron and VEP studies. Victor (1987; 1988) and Purpura et al (1990) showed that the ganglion cells in the retina, except for a constant delay, have a minimum phase temporal character, which does not have a phase slope that becomes steeper as the frequency increases in all the test region from 0.23 to 50 Hz. The ganglion cells in the lateral geniculate nucleus (LGN) essentially have similar spatial-temporal properties as those in the retina (So & Shapley, 1979; Shapley, 1982), it is reasonably to assume that the temporal characteristics of the ganglion cells in LGN do not differ much from those of the ganglion cells in the retina. As shown in the last subsection, the linear element H_1, representing the constitution of the single cells in the early stage up to cortex, however, appears to be a large difference in the temporal characteristic as that of the single cells in the retina and LGN. If this finding is true, one possibility is that the linear process in the cortex before the rectification differs much from the linear process in the retina and LGN.

The clarification of the above issue may be sought by microphysiological studies on the temporal behavior of single cells in the front stage of the cortex. However, the transfer function form, obtained in the last subsection, is not consistent with the previous investigation of temporal character of the VEP pathways. The relevant work is referred to Lopes Da Silva's model proposed in 1970. The stimulation he

used was a sinusoidal modulated light rather than the contrast reversing pattern. In the test, all the neuron receptors sensed the same light function on their receptive fields, and mediate the signals to the cortex. According to the discussion in Section 2.1 and 3.1, the path for signal process can be represented by a sandwich model with non-symmetrical rectifier as shown in Figure 3.9.a. Because the asymmetrical rectification produces both odd and even order harmonics in the cortex, Lopes Da Silva used fundamental component of VEP as a system output for modeling, which essentially characterized linear process of retina-cortex system. The rationale lies in the fact that the asymmetrical rectifier N can be decomposed into an even order rectifier (symmetrical) and an odd order rectifier, and hence, the sandwich system in Figure 3.9.a can be decomposed into two parallel paths which contain the even order rectifier and the odd order rectifier respectively. The scheme for such decomposition is illustrated in Figure 3.9.b. In the figure,

$$N_1(v) = \frac{N(v) + N(-v)}{2} \tag{3.18a}$$

which is an even order rectifier symmetrical about vertical axis, and

$$N_2(v) = \frac{N(v) - N(-v)}{2} \tag{3.18b}$$

which is odd order rectifier symmetrical about original point. If $N_2(v)$ is approximately linear within a certain range of v, The fundamental component, produced only through $N_2(v)$ due to the sinusoid input, characterizes the consequent linear process of H_1 and H_2.

Lopes Da Silva showed that this linear process in the VEP pathways, except for a constant delay, can be described by a transfer function of minimum phase.

Comparing with the above result, we would like to ask: Does the linear process before the cortex have minimum phase or non-minimum phase characteristic? This question is equivalent to: Does the phase characteristic of the neural pathway before the cortex have such a feature that its slope becomes steeper as the frequency increases?

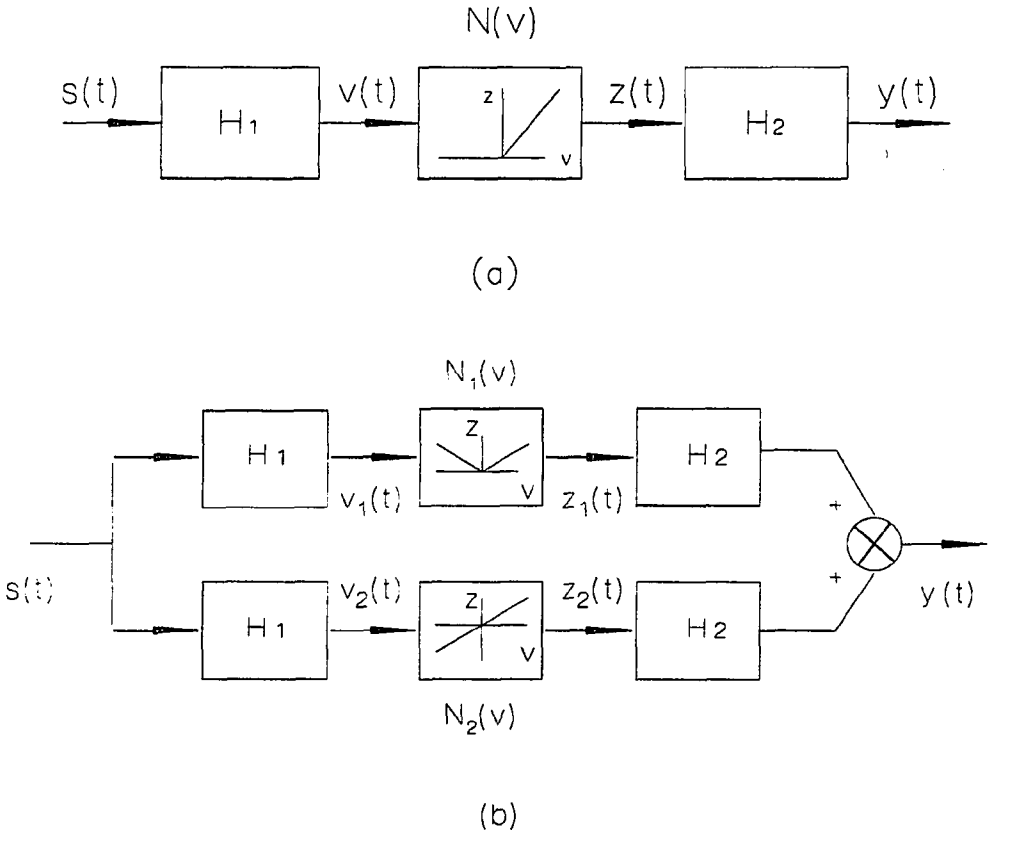

Figure 3.9 a: Neuron signal process due to sinusoidal modulated light is simulated by a sandwich model with an asymmetrical rectifier. **b:** The model in (a) is decomposed into two parallel paths containing an even order rectifier and an odd order rectifier respectively.

To examine this problem, let us suppose that the argument, the slope of the phase characteristic in the early stage of the visual pathway (H_1) becomes steeper as the frequency increases, is true, which means the phase slope at $f_1 + \Delta f$ is steeper than the phase slope at f_1. Then the absolute value of $\frac{d\angle H_1(f_1+\Delta f)}{df_1}$ increases as Δf increases. From equation (3.16), one obtains, for a given f_1, that the absolute value of $\frac{d\phi_{vDFC}(f,f+\Delta f)}{df_1}$ increases with Δf, that is, the slope of the DFC phase response from the entire system increases with the separation of the frequency pair. This outcome indicates that the examination of the argument is accessible by using the two-sinusoid

stimulation technique with different separations between the frequencies within each pair.

The experiment for this examination was performed. Stimuli were constructed with two sinusoids as before, but the separation between f_1 and f_2 was kept as a constant of 1.99 Hz, 3.99 Hz, and 7.98 Hz respectively for each test. If the phase slope of the VEP difference frequency components in the high frequency region becomes steeper as the frequency separation increases, the argument above holds, otherwise the argument fails. The same two subjects A and B were tested in this experiment. Difference frequency components of the VEP, together with their radii of *error circles* and phase error ranges, are depicted in Figure 3.10.1 for subject A and in Figure 3.10.2 for subject B. All data are plotted versus frequency f_1 in linear scale in order to compare the phase slope in the high frequency region.

For the amplitude response, when the separation of Δf becomes larger, the magnitude tends to decrease, and the peak position shifts left along the f_1 axis. For the phase response, an increased phase lag is obtained as Δf increases, which may result from the phase characteristic of H_2. However, the phenomenon that the phase slope becomes steeper with increased frequency separation in the high frequency region is not observed. This finding conflicts with the argument given above and suggests that, for these two subjects, the DFC phase decrease in the high frequency region does not appear to depend on H_1.

3.3.3 Summary and Discussions of This Section

We examined the VEP sum and difference frequency components from ten normal subjects to search for the transfer functions of the sandwich model. We found that, to fit those subjects data, the first linear element in the model must be a non-minimum phase function with zeros in the right half s-plane. This result has not been shown in the literatures concerning temporal characteristics of the visual neural system.

We designed an experiment, using two-sinusoid stimulation with variable separation between the frequency pairs, to investigate the linear processing characteristics

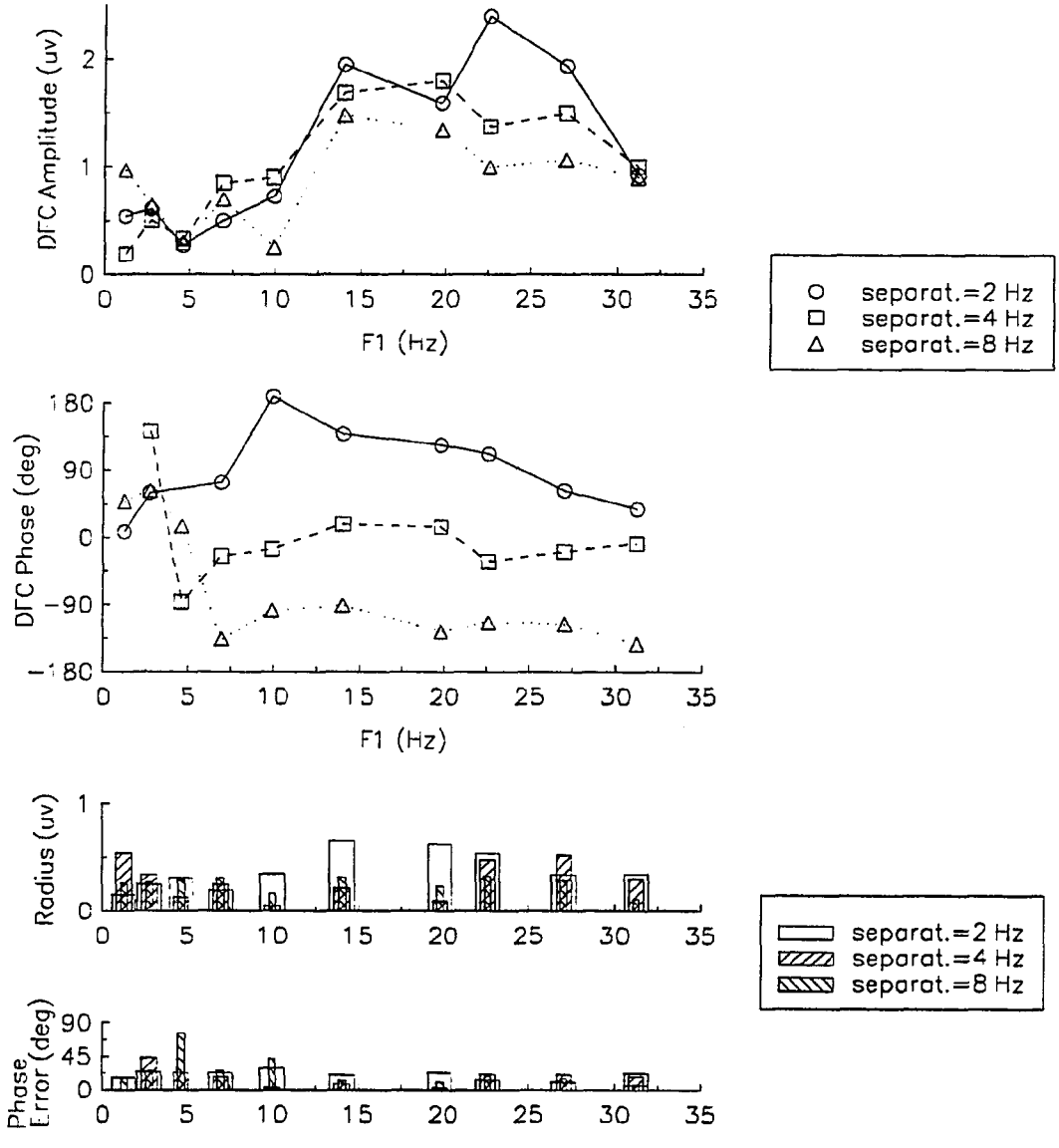

Figure 3.10.1 Experiment of two-sinusoid stimuli with different separation between the frequency pair. Data are collected from subject A and plotted vs. f_1. The top and second rows are the DFC amplitude and phase respectively. The bottom two rows show the radius of error circle and phase error ranges respectively. f_1 were selected as 1.22, 2.75, 4.64, 6.98, 9.97, 14.05, 19.79, 22.59, 27.05, 31.24 Hz. The data corresponding to the separation of 1.99 Hz are marked by circles, 3.99 Hz marked by boxes and 7.98 Hz marked by triangles.

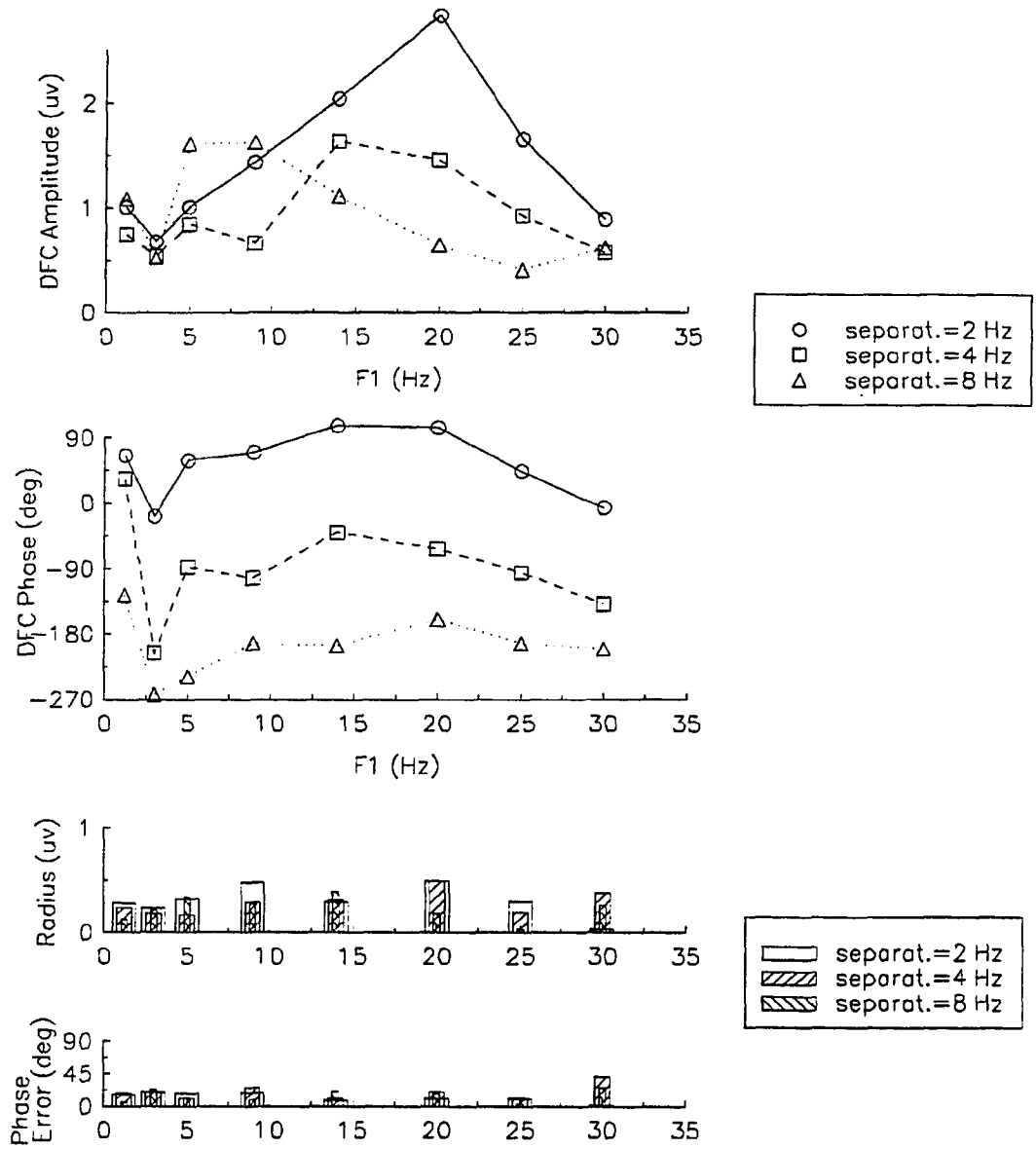

Figure 3.10.2 Experiment of two-sinusoid stimuli with different separation between the frequency pair. Data are collected from subject B and plotted vs. f_1. The top and second rows are the DFC amplitude and phase respectively. The bottom two rows show the radius of *error circles* and phase error ranges respectively. f_1 were selected as 1.22, 2.99, 4.99, 8.98, 13.96, 19.95, 24.93 and 29.92 Hz. The data corresponding to the separation of 1.99 Hz are marked by circles, 3.99 Hz are marked by boxes and 7.98 Hz are marked by triangles.

before the cortex (which is simulated by the first linear element, H_1, in the sandwich model). Result from two subjects showed that the DFC phase response, used to identify the phase characteristic of H_1, did not only depend on H_1.

If our finding does hold for large populations, there is a question: Where is the functional subsystem, other than H_1, modifying the VEP difference frequency components?

Previous studies on the signal processing behavior of neural system found that two inhibitory mechanisms, *contrast gain control* and *lateral interaction* (e.g. Zemon, 1984; Zemon, Victor and Ratliff, 1986; Zemon, Conte & Camisa, 1987), play an important role in neural signal processing, modifying both amplitude and phase of the signal transmitted in the direct-through pathways. In the two-sinusoid stimulation tests, such an inhibitory process, which appears to exist in the cortex, may modify the rectified signal from an earlier stage to cause extra phase shift in the VEP.

Indeed, a transfer function of non-minimum phase in the model may provide a fit for the difference frequency component data of VEP. We emphasize in this work, however, that the model should not only satisfy the input-output relation of the entire VEP system, but also, each element in the model should be interpretable physiologically, that is, the mathematical description of each element should, as close as possible, match the temporal characteristic of the subsystem it represents. From this point, it is worthy to modify the sandwich model to include some important functional mechanisms. This work not only narrows the gap between the model's behavior and that of the real system, but also, it allows quantitative analysis of such mechanisms' activities and their interactions.

CHAPTER 4
INHIBITORY MECHANISM

4.1 General Introduction

Photoreceptors in the retina sense the light information in their receptive fields and transmit such information to the brain. However, this neural message is not a simple transduction of the optical image. The image in the visual system is transformed by spatial interactions between neurons, and decoded in the brain to recover what the eye has seen. The spatial interaction can be classified into two types: One type that nerve cells triggering impulses (action potential) in other cells is considered to be excitation and forms a primary direct-through pathway, which mediates signals from earlier to later neuronal layers. Another type that nerve cells preventing impulses from arising in other cells is inhibition and mediates signals in local synaptic areas. A cell receives many excitatory and inhibitory inputs from other cells and in turn supplies many others. The process whereby a cell adds together all the incoming signals that excite and inhibit it is known as integration which essentially determines a cell's ability to excite the next cells in the pathway (Kuffler & Nicholls, 1976).

The functions of inhibitory mechanisms are very important. The image information in the neuronal system is carried by impulses in nerve fibers, but the information capacity of a neural pathway depends not only on the number of fibers, but also upon the mean rate of nerve impulses in the fibers. Barlow (1969) pointed out that this mean rate of impulses should be able to vary adaptively to maintain the "economy" situation, which means the genetically determined patterns of synaptic connections should enable the animal's typical sensory environment to be represented by low average activity in sensory centers. If the environment changes, the average activity should change correspondingly, but such change in those synaptic connections should again enable the new environment to be represented economically, that is, the low mean firing rate of the nerve cells should be restored. Barlow pointed out further that the neural inhibition may function as a mechanism that reduces the flow of impulses in nerve fibers to achieve such adaptive reduction redundant information.

The other important role that neural inhibition may play is in "form perception" (Ratliff. 1965). In the initial stage of the neural pathway, the photoreceptors process the optical information corresponding to their receptive fields, which is relatively separate and localized. In the cortex, neural messages interact on their way from distal stage to high levels of processing; more lateral interaction is involved due to highly branched dendritic connections that link the spatially localized messages together (Benevento, Creutzfeldt & Kuhnt, 1972; Creutzfeldt, Kuhnt & Benevento, 1974). Physiological evidence has been obtained to show that, in the visual cortex. most cells become more selective in their receptive field properties (Maffei & Fiorentini. 1973): They acquire binocularity and exhibit greater selectivity to orientation and direction of movement than the cells at lower levels of the visual system (Hubel & Wiesel. 1962).

Two inhibitory mechanisms are of interest in the current research, one is a *contrast gain control* mechanism which is activated by stimulus contrast change (Enroth-Cugell & Robson, 1966; Shapley & Victor, 1978; Zemon, Conte & Camisa, 1987), the other is *lateral interaction* activated by neural lateral connections within the local neighboring area (Nabet & Pinter,1991; Zemon & Ratliff, 1984). Since both mechanisms have effects on excitatory signal transmission, for the sake of modeling. it is necessary to investigate the roles that both mechanisms play in generating the VEP.

4.2 Contrast Gain Control Mechanism

4.2.1 Prior Studies on Contrast Mechanism

Early studies of contrast gain control that closely relate to the present modeling have involved physiological investigations of ganglion cells in the cat retina (e.g. Shapley & Victor, 1978; 1980). Those researchers used a contrast reversing stimulus that consisted of an eight-sinusoid temporal modulation of a grating pattern. The X type ganglion cells, due to their linear character, were studied based on the response of their fundamental frequency components; the Y type cells, due to their nonlinear

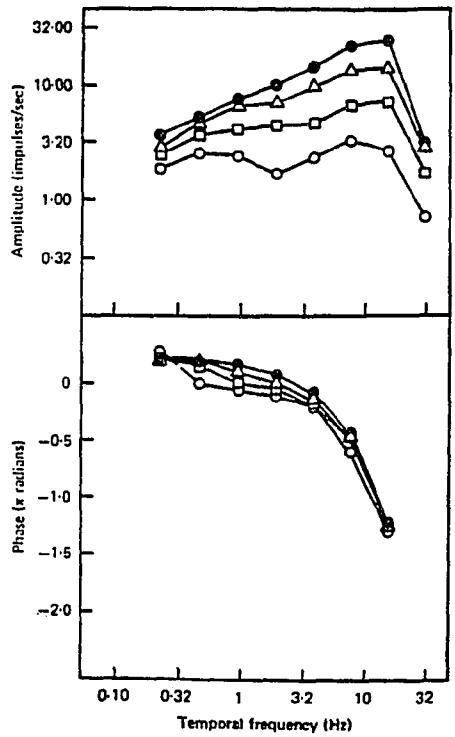

Figure 4.1 Fundamental frequency components of an on-center X cell, elicited by an eight-sinusoid grating pattern stimulation. Modulation depth per sinusoid in the pattern was set at different levels: circle, 1.25%; box, 2.5%; triangle, 5% and Filled circle, 10%. The mean luminance was 20 cd/m^2. Source: Shapley & Victor, 1978.

character*, were studied based on the response of second order (i.e., sum and difference) frequency components†. The studies demonstrated a nonlinear effect of stimulus contrast on the temporal tuning characteristics of both X and Y cells. For X type cells, as Figure 4.1 shows, the responses of fundamental frequency components grow much less than linearly with input contrast when the input temporal frequency is below 2 Hz; the responses grow nearly proportionally to input contrast when the frequency is above 8 Hz. On the other hand, the phases of the fundamental frequency components advance as contrast increases over nearly the entire frequency range from 0.32 Hz to 15 Hz. For Y type cells, shown in Figure 4.2.a, the sum frequen-

*Y type ganglion cells predominantly produce even order harmonics, which is evidence that a nonlinear process exists in the Y cell path.

†Sum and difference frequency components are those at the frequencies $f_{i+1} \pm f_i$ $(i = 1, 2, \cdots, 7)$, elicited by the eight-sinusoid stimulation.

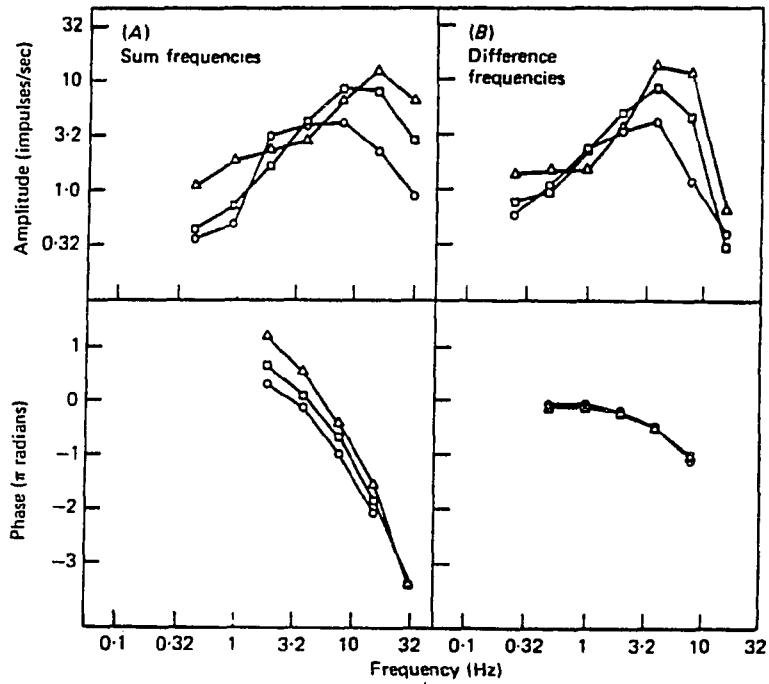

Figure 4.2 Amplitudes and phases of the second-order frequency components, elicited by an eight-sinusoid grating pattern stimulation, as a function of a contrast in an on-center Y cell. The three levels of contrast are indicated by the symbols: ○, 2.5%; □, 5%; △, 10%. The mean luminance was 20 cd/mm^2. In A (left), amplitudes and phases of the second order harmonics are plotted versus $2f_i$. In B (right), amplitudes and phases of the difference frequency components are plotted versus $f_{i+1} - f_i$.
Source: Shapley & Victor, 1980.

cy responses in the region above 10 Hz increase more rapidly with contrast than do the responses to lower frequencies; the phase responses have a larger advance as the stimulus contrast increases at the lower frequencies than at the higher frequencies.

The above outcome suggests that the retina's temporal characteristic is not linear, but has parametric nonlinear dependence on contrast. The mechanism that adjusts the signal transmission characteristic in terms of the signal contrast is called *contrast gain control* or *contrast mechanism.* The formation of the contrast gain control in the retina may be a feedback signal from amacrine cells to bipolar cells that modifies information processing in the bipolar cells (Levick, 1975; Kolb, Famiglietti & Nelson, 1976).

Another interesting investigation by Shapley and Victor (1980) showed that the difference frequency component (DFC) of Y type ganglion cells elicited by an eight-sinusoid stimulus essentially does not exhibit a phase shift with stimulus contrast change. The DFC amplitude responses, however, present a similar dependence on contrast as the sum frequency component do (see Figure 4.2.b).

The effect of contrast gain control on the VEP was investigated by Zemon and his co-workers in 1987. They found that the difference frequency components (DFC) of the VEP, measured from human scalp using the two-sinusoid stimulation, have a significant increase in phase with increase of stimulus contrast in the high frequency region above 20 Hz (Zemon, Conte & Camisa, 1987). According to the findings by Shapley and Victor, difference frequency components produced in the retinal Y cells do not have a phase shift with stimulus contrast. Therefore, the phase shift of the DFC in the VEP may result from the phase shift of fundamental frequency components produced in the initial linear stage. However, since the separation between the input frequency pairs was small (2 Hz), in the high frequency region above 20 Hz, the phase shifts in the fundamental frequency components, caused by the contrast mechanism in the initial stage, can be expected to be nearly identical. According to (3.8), the phase change of the DFC in the VEP is the difference between the phase changes of the individual fundamental frequency components in the early stage before the rectification. Thus, nearly identical phase changes of the fundamental frequency components will not result in significant phase changes in the DFC recorded from the cortex. From this point, Zemon et al. (1987) suggested that there might be another contrast mechanism in the cortical area following the rectifier, which is responsible for the phase change in the VEP difference frequency components. Recently, the existence of the contrast gain control in the cortex has also been reported by Geisler and Albrecht (1992).

The investigation above leads to the important conclusion that the nonlinear process exists in both H_1 and H_2 in the sandwich model. In the following section, we will discuss the VEP experimental result obtained using contrast varying of the

two-sinusoid stimulus to seek the rules of inhibitory processing for the contrast mechanism in the cortex.

4.2.2 Demonstration of Contrast Gain Control in the VEP

The experiment to demonstrate the effects of the contrast mechanism is similar to that done by Zemon et al. in 1987. The stimulus contained two superimposed sinusoids. The separation between the two frequencies in a pair was fixed at 1.99 Hz. The sampling frequency points were set to f_1 =2.99, 4.99, 8.98, 13.96, 19.95,24.93, 29.92 Hz. The contrast of the stimulus was set to 10%, 20%, 30% and 40% for each test. Other conditions were the same as described before. Difference frequency components (DFC) were obtained by Fourier analysis on the recorded VEP data.

Two subjects, A and B as mentioned before, were tested in this work. The results, which are shown in Figure 4.3.1 for subject A and Figure 4.3.2 for subject B, are qualitatively consistent with those reported by Zemon et al. (1987). In the left column of Figure 4.3, data are plotted versus f_1 in solid, long dash, dash and dots, corresponding to the stimulus contrast of 10%, 20%, 30% and 40% respectively. In the right column of Figure 4.3, data are plotted versus stimulus contrast, but only those data in high frequency region above 20 Hz are displayed. At zero contrast (null input), we set all the amplitudes of DFC to zero. The accuracy of the measurement is expressed by the radius of *error circle* and phase error range calculated from (2.37) and (2.39) respectively. When the amplitude of DFC is smaller than the radius of *error circle*, the phase data is not a reliable measurement, and is not displayed in the figure.

It is seen, when the frequency is above 20 Hz, that both amplitude and phase of the DFC increase monotonically with contrast. However, the data curves in the right column of Figure 4.3 show that the amplitude does not increase linearly with contrast, but its slope decreases as the contrast increases. This means the signal transfer gain is inversely related to signal contrast. In the low frequency region, the result is not clear. At some frequency points, the amplitude and phase responses

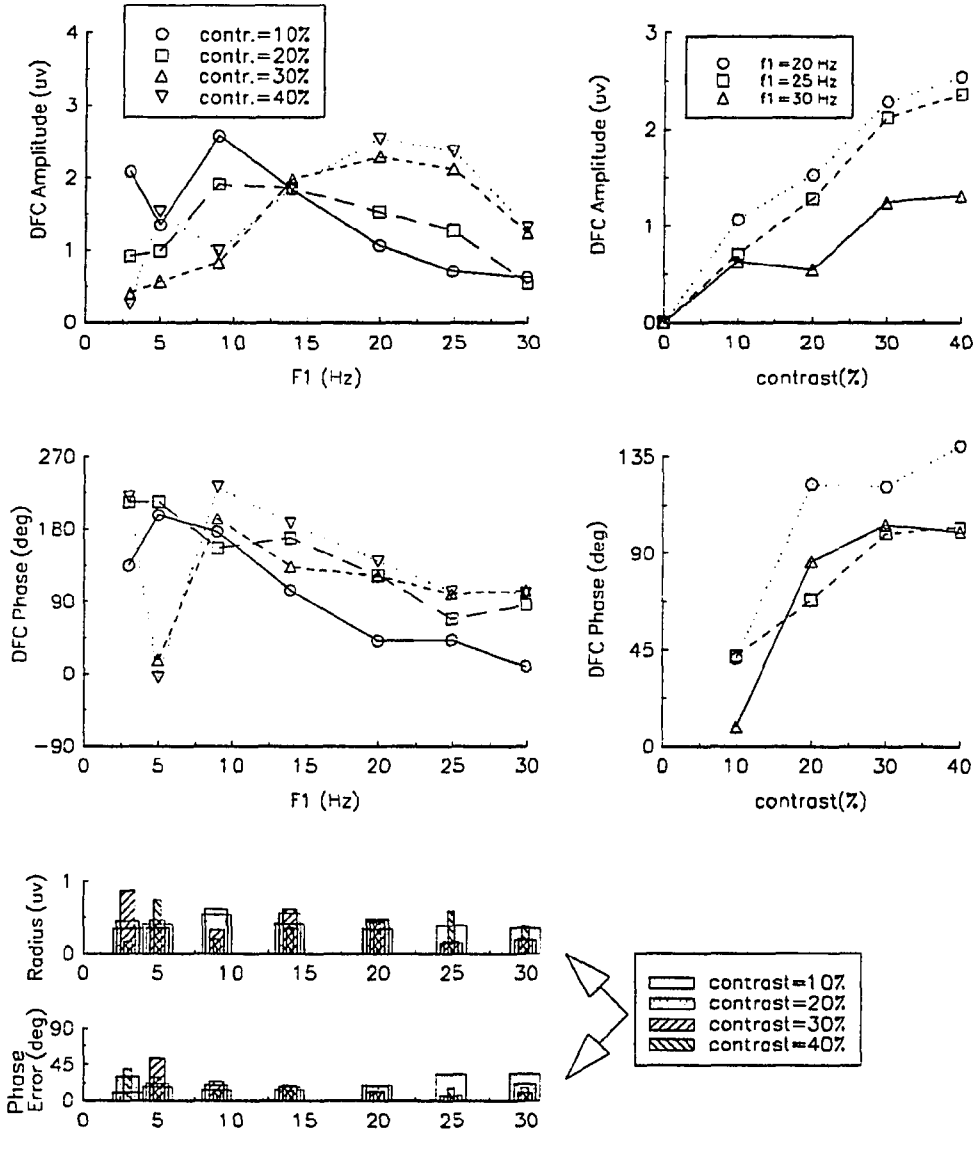

Figure 4.3.1 Experiment for observing the effect of contrast gain control on the VEP. DFC data were measured from subject A. Two-sinusoid stimuli with different contrast and frequency pairs were used. The separation between the frequency pairs was kept at 1.99 Hz in each test. Vector averaged components, the radii of *error circles* and phase error ranges are obtained from four repeated measurements. In the left column, DFC data are plotted versus f_1 in linear scale to display the results in more detail in high frequency region. In the right column, DFC data are plotted versus stimulus contrast, but only those data corresponding to f_1 =19.95, 24.93, 19.92 Hz are displayed; amplitude corresponding to zero contrast stimulus (null input) is set to zero. When the radius of *error circle* is bigger than the amplitude of DFC, the phase data is not a reliable measurement, and is not dispalyed in the figure.

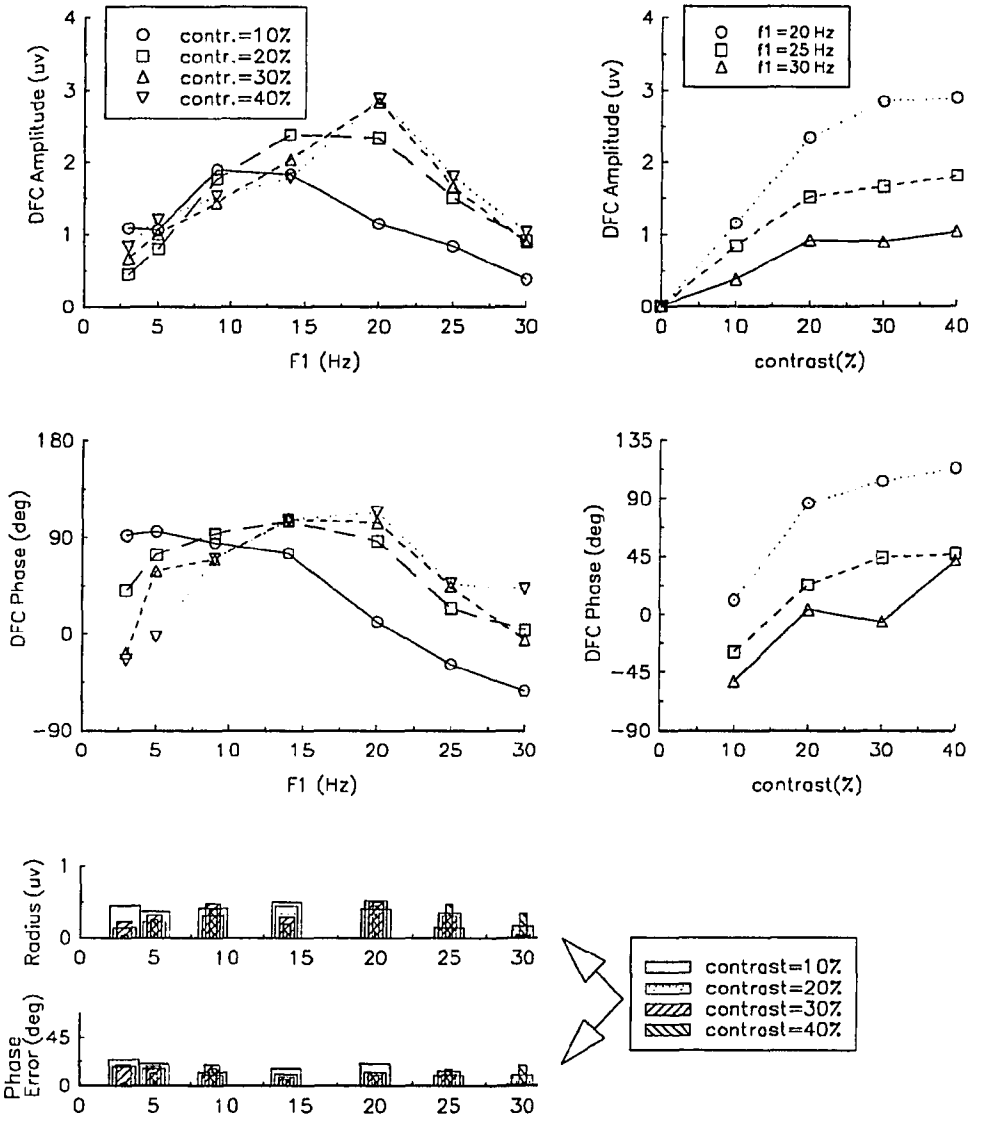

Figure 4.3.2 Experiment for observing the effect of contrast gain control on the VEP. DFC data were measured from subject B. Two-sinusoid stimuli with different contrast and frequency pairs were used. The separation between the frequency pairs was kept at 1.99 Hz in each test. Vector averaged components, the radii of *error circles* and phase error ranges are obtained from four repeated measurements. In the left column, DFC data are plotted versus f_1 in linear scale to display the results in more detail in high frequency region. In the right column, DFC data are plotted versus stimulus contrast, but only those data corresponding to f_1 =19.95, 24.93, 19.92 Hz are displayed; amplitude corresponding to zero contrast stimulus (null input) is set to zero. When the radius of *error circle* is bigger than the amplitude of DFC, the phase data is not a reliable measurement, and is not dispalyed in the figure.

corresponding to the high contrast stimulus are even lower or more lagging than the responses corresponding to the low contrast stimulus.

We suggest that it is the contrast gain control in the cortex that makes the above response curves change shape. There are three reasons for this suggestion:

1. The response dependence on contrast is not the consequence of a static saturation. In the case of such a nonlinearity, a phase shift in the DFC due to stimulus contrast change would not occur (according to (3.8)).

2. The activity appearing in the high frequency region during the above experiment rules out the possibility of lateral interaction, because the lateral inhibitory mechanism (to be discussed in the next section) has little effect in the frequency region above 20 Hz.

3. A phase shift in the DFC rules out the possibility of the contrast mechanism in the retina accounting for the results (as explained before in this chapter).

Therefore, the changes in the response of the DFC with different stimulus contrasts appears to reflect the behavior of contrast gain control at the cortical level.

Although the knowledge of the anatomic structure of the neural circuitry, which is responsible for such modification, is lacking at the current time, a model, proposed by Shapley and Victor in 1978 for the contrast gain control of retinal ganglion cells, is presented here in Figure 4.4 to account for the nonlinear process of the contrast mechanism in the cortex. Except for some different interpretations for the elements, this model is still valid for explaining the contrast gain control phenomena in the VEP.

In the model, an element H_2 and its output $y(t)$ form a neuronal excitatory pathway in the cortex. This element however receives another input I_G produced by contrast gain control G. Element G filters and senses the overall contrast of the signal processed in the excitatory pathway, and produces the output I_G that consequently modulates the parameters of element H_2. Since signal contrast, rather than signal value, is measured by G, element G must contain an even order nonlinearity or be a

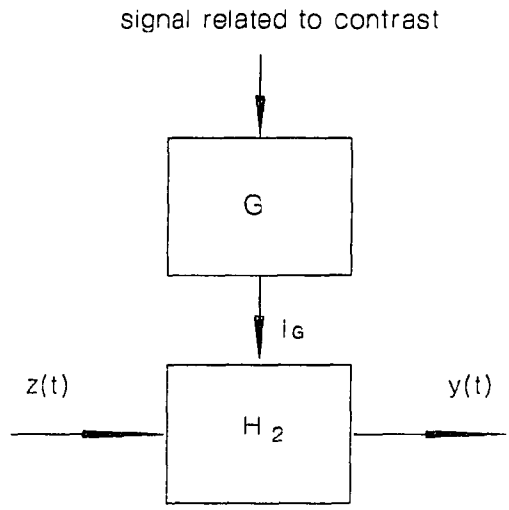

Figure 4.4 The model for contrast gain control in the cortex. A linear element H_2 representing direct-through pathway in the cortex is surrounded by a contrast gain control element G. This element senses the overall signal contrast in the direct-through pathway, and produces a signal I_G that modifies the temporal characteristic of H_2.

full-wave rectifier. which can extract the input signal contrast. Its input may either come from an earlier stage or feedback from the output $y(t)$.

4.3 Lateral Inhibitory Mechanism

4.3.1 Prior Studies on Lateral Inhibition

Investigation on neural networks can be implemented by means of neuronal receptive field studies. In past decades, much progress has been achieved in this area. It has been shown that visual neural structure is arranged in a retinotopic fashion at each level (Pearlmen, 1975). That is, the retinal cells in a given region project to a given region of the lateral geniculate nucleus, and then project to a given region of the visual cortex. Besides those parallel signal forwarding paths, within a neural cell layer, the cells in each region may affect each other due to lateral connections. It is believed, in the neural network, that forwarding pathways transmit excitatory signals, while lateral connections transmit inhibitory signals (Zemon Conte & Camisa, 1987). Thus, a signal processed in one forwarding path will inhibit the signal processed in

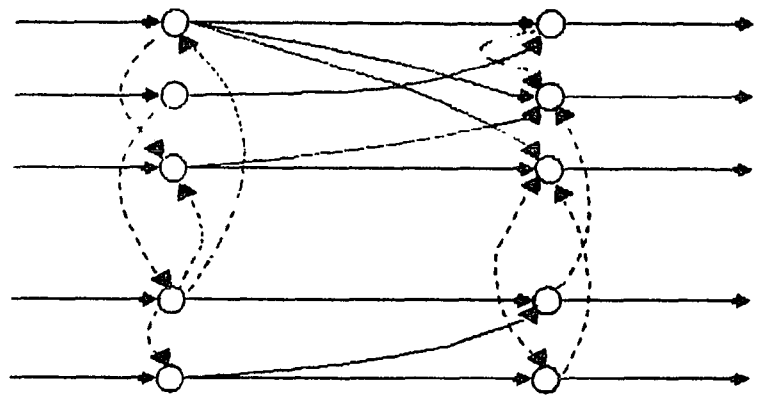

Figure 4.5 A demonstration of neural connections between two layers. Excitatory connections are marked by solid arrows, while inhibitory connections are marked by dash arrows.

the neighboring forwarding path through local lateral connections. A simple diagram of such neural structure is demonstrated in Figure 4.5.

The mechanism by which a signal processed in one cellular region inhibits the signal processed in another region via lateral connections is called *lateral inhibition or lateral interaction.* It has been found that this mechanism exists in the different layers of the visual pathways from the retina (Werblin, 1972; Masland, 1986), to the lateral geniculate nucleus (Kuffler & Nicholls, 1976), to the cortex (Benevento, Creutzfeldt & Kuhnt, 1972) that contribute to the VEP.

To investigate lateral inhibitory activity, one must extract this contribution to the VEP, which contains mixed contributions from other mechanisms. This work was done by Zemon and Ratliff (1984) by using two-sinusoid stimulation constructed in either a *superimposed* or *lateral condition.* In the *superimposed condition,* the stimulus was the same as the one described in Section 2.2. VEP sum and difference frequency components elicited by such stimulation essentially emphasize the excitatory process in the visual pathways. In the *lateral condition,* the stimulus was constructed in such

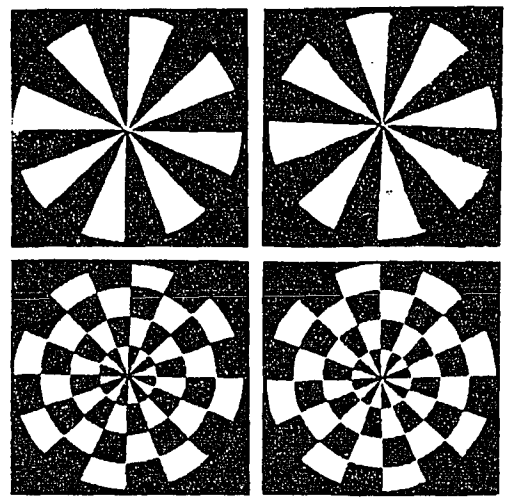

Figure 4.6 Photographs of the windmill-dartboard stimulus used to elicit lateral interaction. Segments in the central disk and the second annulus are modulated by one sinusoid of frequency f_1, while segments in the first and third annuli are modulated by a second sinusoid of frequency f_2. In this situation, the percept alternates between that of a dartboard and that of a windmill. Photographs of the stimulus at intermediate phases, between windmill and dartboard, are shown to the right of the windmill and dartboard photographs.
Source: Zemon, 1984.

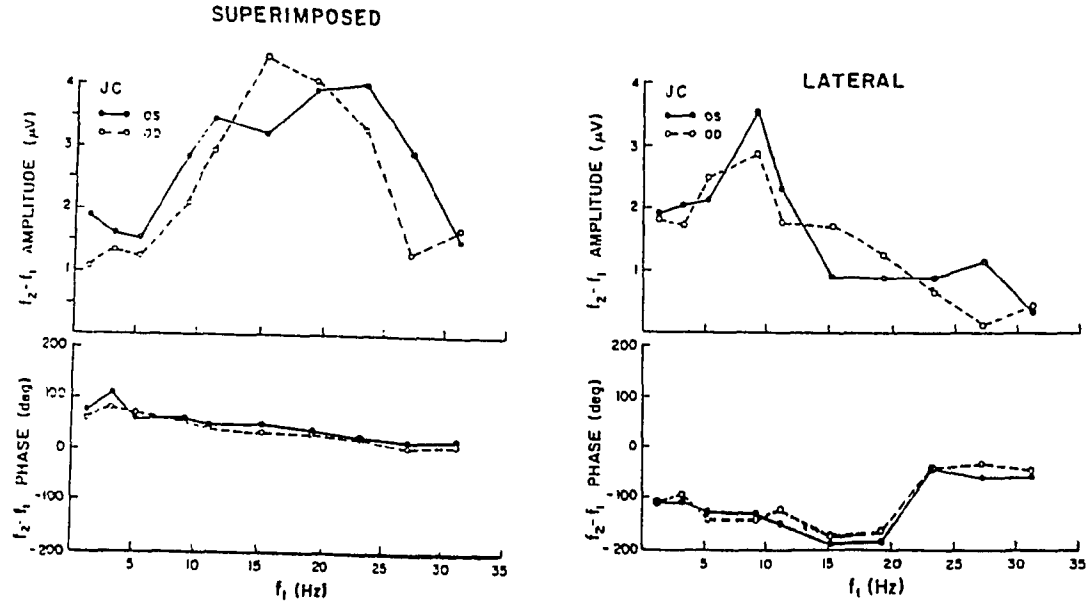

Figure 4.7 Amplitude and phase of the difference intermodulation component, for one normal subject, obtained using superimposed and lateral stimuli.
Source: Zemon, 1984.

a way that the luminance in the central disk and the second annulus was temporally modulated by a contrast reversing sinusoid with frequency f_1; while the luminance in the first and third annuli was modulated by a contrast reversing sinusoid with frequency f_2 (see Figure 4.6). Those separate stimulus functions thus elicited different temporal signals in the neural channels that interact with each other through lateral connections, and produce intermodulation components (SFC and DFC) in the VEP. These intermodulation components, to some extent, reflect the characteristics of the lateral pathways. The difference frequency component data, measured from a typical normal subject in either superimposed or lateral conditions, reported by Zemon (1984). are depicted in Figure 4.7.

Under the *superimposed condition*, similar to the data presented in Section 3.2, DFC response presents an amplitude peak around 20 Hz, and a negative phase slope in the high frequency region. Under the *lateral condition*, the DFC amplitude response falls off above 10 Hz, and the phase response differs by about 180^0 from that obtained under the *superimposed condition* at low and intermediate frequencies; it is nearly identical to the *superimposed condition* data at high frequencies. From those observations, Zemon pointed out that strong lateral interactions in the neural network may occur when the input frequency is around 10 Hz.

4.3.2 Demonstration of Lateral Interaction in the VEP

Based on the discussion in the last section, we propose a VEP pathway model that includes the lateral inhibitory mechanism. The model, illustrated in Figure 4.8.a, contains two identical parallel paths composed of linear-nonlinear-linear elements in cascade, which represent parallel neural channels that mediate the input signals from the retina to the brain. Lateral interactions between each channel are implemented through the lateral element L, which receives the input from one channel and sends the output to the other channel. As mentioned in Section 4.1, the major lateral inhibitory component occurs in the cortex. The signal I_L from the lateral pathway is applied to the H_2 stage and modifies the direct-through signal in a nonlinear manner.

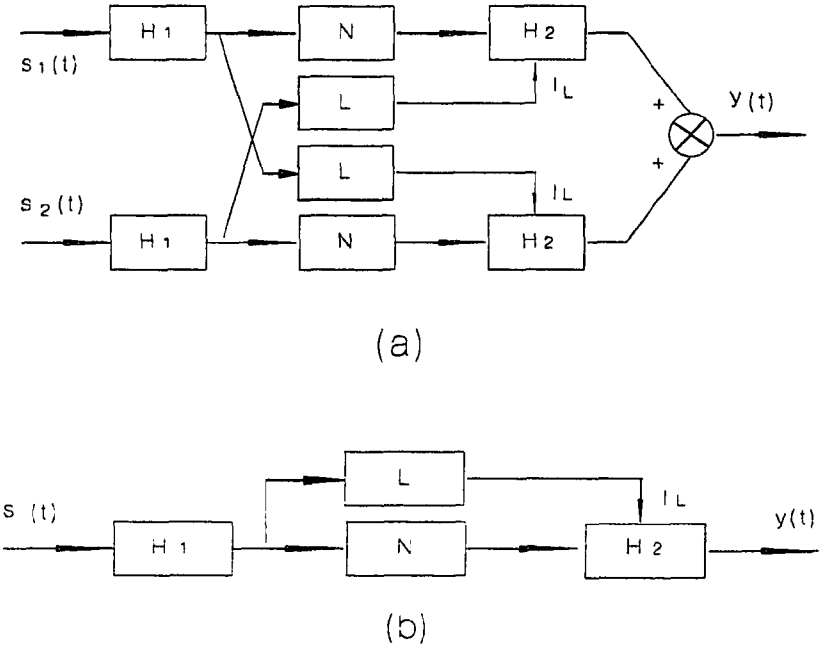

Figure 4.8 a: A model structure containing two parallel direct-through pathways connected with each other by lateral pathways. **b:** A model simplified from the structure in (a) with hypothesis that the symmetrical pathways are identical.

Considering that the lateral inhibitory signals are generated by neurons in the cortex, the lateral path begins at the position after H_1. The model in Figure 4.8.a can be further simplified to a structure shown in Figure 4.8.b, given symmetrical pathways that are identical.

Next, we discuss the experiment conducted in this study to demonstrate the effect of lateral interactions. Lateral inhibition is activated by the signals that are generated in neighboring neurons. If two superimposed sinusoids are used to modulate the luminance in the first and third annular rings of the dartboard pattern, and the luminance of central disk and second annular ring of the pattern is temporally modulated by a single third sinusoid with a different frequency and contrast, it is possible to observe how the difference frequency component (DFC) elicited by the superimposed two sinusoids is affected by the lateral neural signals corresponding to

the single sinusoid modulation of neighboring neurons.

The present experiment was designed and conducted in such a fashion. Two superimposed sinusoids were applied to the first and third annular ring of the dartboard pattern stimulation shown in Figure 2.2 at f_1=19.45 Hz and f_2=21.44 Hz. The peak contrast of each of these two sinusoids was 30%. The third sinusoid, applied to the central disk and second annular ring, served as a lateral signal with a frequency of 2.99, 4.99, 9.97, 20.44, and 24.93 Hz, and a contrast of 0%, 5%, 15% and 30%. Each test ran 32.08 seconds. Difference frequency components (DFCs) were obtained by Fourier analysis. The two adult subjects, A and B, were tested in this experiment. The results are depicted in Figure 4.9.1 for subject A and Figure 4.9.2 for subject B. The accuracy of the measurement is expressed by the radius of *error circle* and phase error range calculated from (2.37) and (2.39) respectively. When the amplitude of DFC is smaller than the radius of *error circle*, the phase data is not a reliable measurement, and is not displayed in the figure.

There are several outcomes:

1. In the entire frequency region (2.99 Hz–24.93 Hz), when the third sinusoid has nonzero amplitude ($A_{f_3} \neq 0$), the DFC response is attenuated in amplitude and advanced in phase in comparison with the data collected when $A_{f_3} = 0$.

2. Significant effects of the third sinusoid on the DFC occur at frequencies f_3 below 20 Hz. Above 20 Hz, the effect on DFC amplitude decreases remarkably for subject A, and is hardly observed for subject B. As f_3 increases to 20 Hs, Phase values of both subjects approach the value obtained when A_{f_3}=0.

3. The DFC amplitude has a minimum value when f_3 is around 10 Hz, and increases when f_3 increases or decreases from this point.

4. At frequency $f_3 = 10$ Hz, there is a certain relation between DFC response and the lateral signal's contrast A_{f_3}: When the contrast A_{f_3} increases, the DFC amplitude decreases and the DFC phase advances.

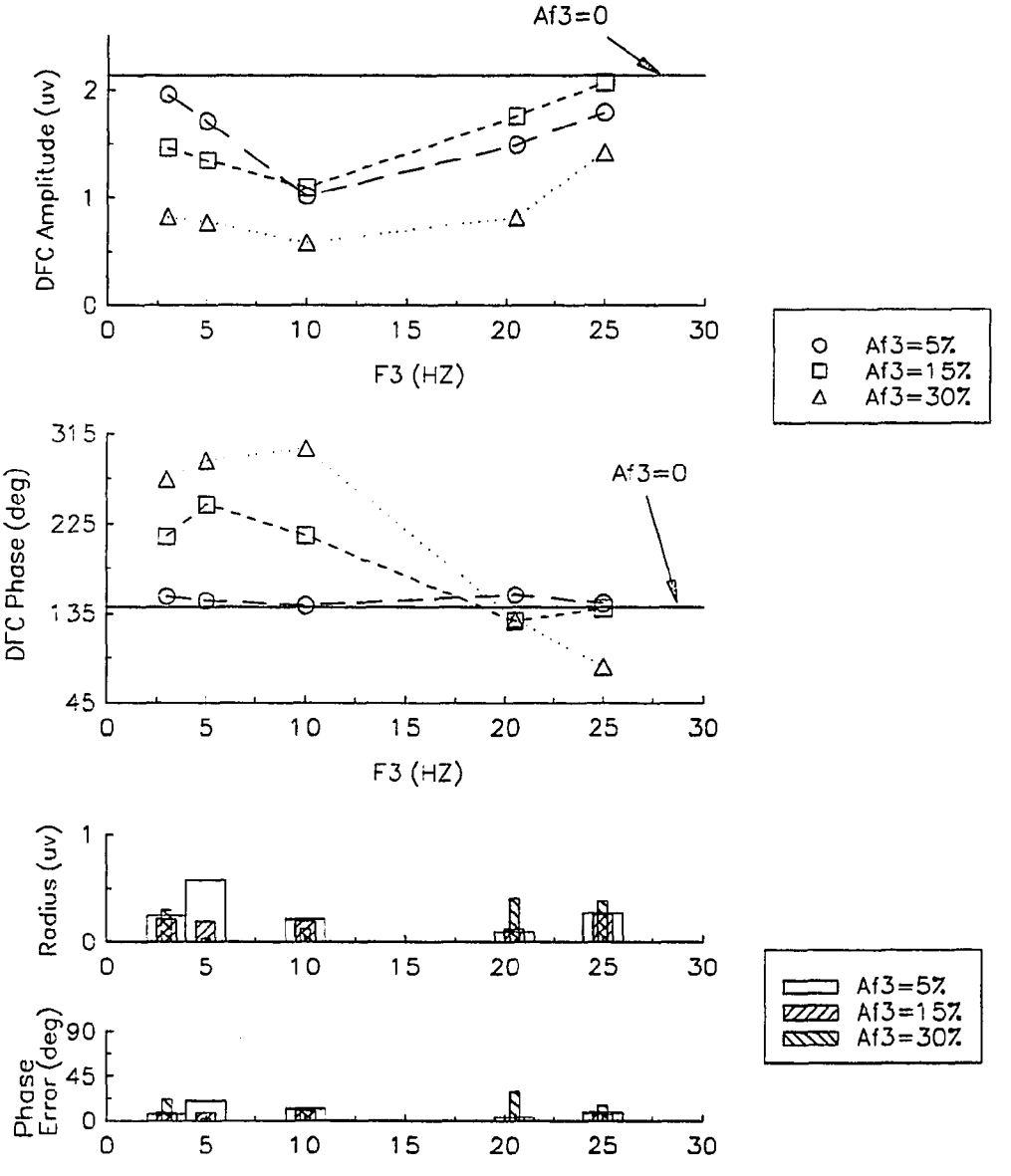

Figure 4.9.1 Examining the effect of lateral interactions: DFC data from subject A. The luminance of first and third annuli was modulated by a sum of two sinusoids with frequencies f_1=19.45 Hz, f_2=21.44 Hz and contrast of 30%. The luminance of central disk and second annulus was modulated by a single sinusoid with frequency f_3=2.99, 4.99, 9.97, 20.44, and 24.93 Hz and contrast A_{f_3}=0%, 5%, 15% and 30%. Vector averaged components, the radii of *error circles* and phase error ranges are obtained from four repeated measurements, and are plotted versus f_3. When the radius of *error circle* is bigger than the amplitude of DFC, the phase data is not a reliable measurement, and is not dispalyed in the figure.

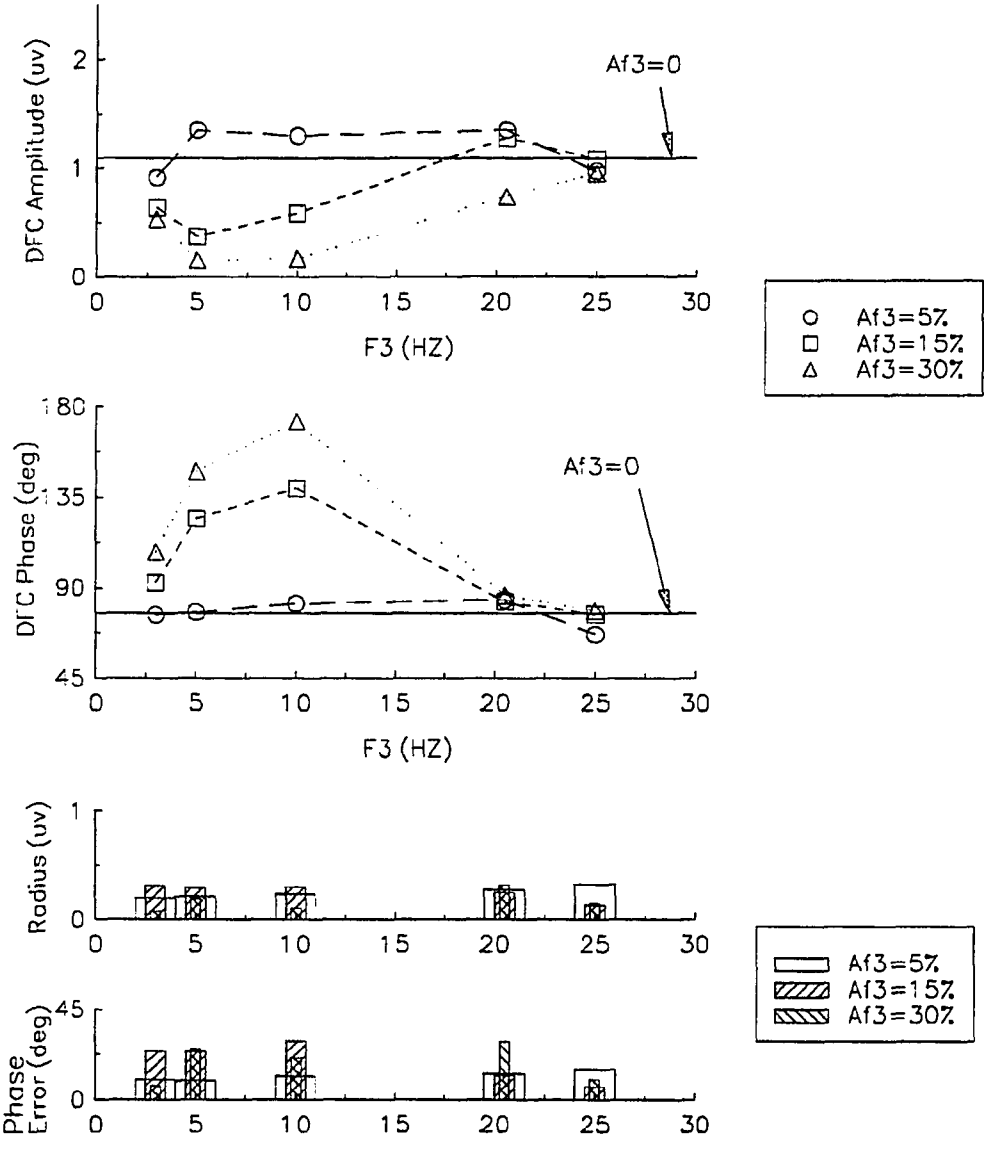

Figure 4.9.2 Examining the effect of lateral interactions: DFC data from subject B. The luminance of first and third annuli was modulated by a sum of two sinusoids with frequencies f_1=19.45 Hz, f_2=21.44 Hz and contrast of 30%. The luminance of central disk and second annulus was modulated by a single sinusoid with frequency f_3=2.99, 4.99, 9.97, 20.44, and 24.93 Hz and contrast A_{f_3}=0%, 5%, 15% and 30%. Vector averaged components, the radii of *error circles* and phase error ranges are obtained from four repeated measurements, and are plotted versus f_3. When the radius of *error circle* is bigger than the amplitude of DFC, the phase data is not a reliable measurement, and is not dispalyed in the figure.

If the above result. the DFC amplitude and phase that vary with contrast and frequency of the third sinusoid (lateral signal), reflects the lateral interaction phenomena, what does it tell us?

a. Since the effects of the lateral signal can be observed for DFC responses generated at frequencies other than f_3, a nonlinear process is indicated.

b. Input frequencies f_1 and f_2 are set close together. If the nonlinear gain control exerted through lateral interactions mainly affected the transfer characteristics of H_1, it would cause almost the same phase shift in the fundamental components produced by H_1: $\phi_v(f_1)$ and $\phi_v(f_2)$ are nearly identical. The phase of the DFC results from the difference between $\phi_v(f_1)$ and $\phi_v(f_2)$ (see (3.8)). Thus, no significant change in the DFC with contrast would be expected. A large DFC phase advance is found in this experiment (about 180^0 as contrast ranges from 0% to 30%), which indicates that principal nonlinear effect of the lateral interaction is exerted on H_2.

c. Since lateral inhibition will cause signal phase shift, the negative slope in the phase response of the DFC (see Figure 3.5 and 3.6) may result or partially result from the effect of this mechanism, particularly in the middle frequency region.

d. High frequency input in neighboring receptive fields will not cause significant contrast gain control through lateral interactions. The contrast of the input signal in the high frequency region, however, does produce a contrast gain control effect on local excitatory signals. (experiment result in Section 4.2.2). This implies that there are at least two kinds of inhibitory paths in the cortex: one possesses a lowpass filter and another one does not.

4.4 Shunting Inhibition Model

Inhibition within a single neuron can be simulated by a shunting inhibition model proposed by Furman in 1965. It assumes that inhibitory influences cause a shunting

of a portion of the excitation-produced depolarizing current in the receiving neuron's dendrite. This assumption is dictated by its considerable physiological plausibility. It has been found that interneuronal inhibition depended on nerve membrane conductance changes (Eccles, 1961; Lettvin, 1962). In the dendrites of a receiving neuron, the activation of an excitatory ending produces a current flow in a dendrite; the activation of an inhibitory ending results in a conductance increase of the membrane patch on which the ending terminates, which results in a portion of the excitatory-produced current to be shunted through this conductance. However, if the diameter and length of the dendrite is sufficient large and short, it will present a relatively low resistance path to the site of impulse generation. In this case, the local position and ordering of the inhibitory endings does not substantially affect the resultant generator current. A simple scheme of the shunting model is illustrated in Figure 4.10, in which, i_k is the source current produced by all of the excitatory influences acting on neuron N_k; V_{sj} $(j = 1, 2, \ldots, q)$ is the signal produced by each inhibitory neuron and transmitted to the neuron N_k; i_e, the generator current, is the part of the source current reaching the excitable portion of neuron N_k through membrane conductance G_e; i_{sj} $(j = 1, 2, \ldots, q)$ is the part of the source current shunted through the inexcitable portion of the membrane, whose conductance G_{sj} $(j = 1, 2, \ldots, q)$ is signal V_{sj} dependent; and C is the membrane capacitance. The basis of this model can be found in the article by Furman (1965) and the book by Nabet & Pinter (1991).

Now we assume that the shunting conductance G_{sj} is proportional to the inhibitory signal V_{sj}, that is,

$$G_{sj} = m_j V_{sj} \qquad j = 1, 2, \ldots, q \tag{4.1}$$

where $1 \leq j \leq q$ and m_j is a constant. From Figure 4.10, one obtains

$$\frac{C}{G_e}\frac{di_e}{dt} + i_e + i_s = 0 \tag{4.2a}$$

where

$$i_s = \sum_{j=1}^{q} i_{sj} = \frac{i_e}{G_e}\sum_{j=1}^{q} G_{sj} = \frac{i_e}{G_e}\sum_{j=1}^{q} m_j V_{sj} \tag{4.2b}$$

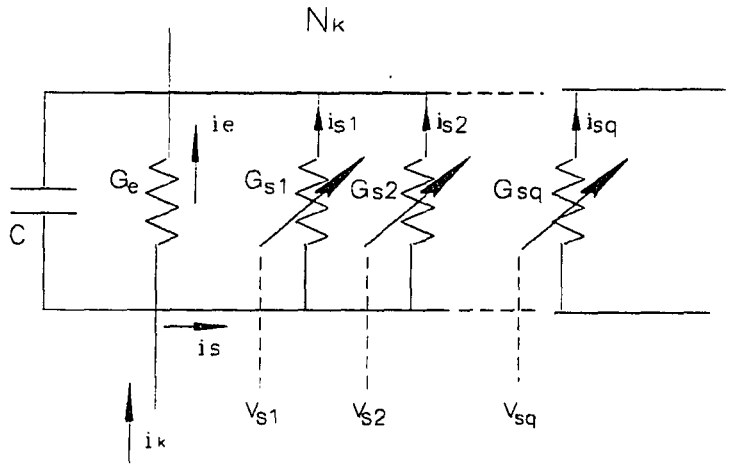

Figure 4.10 Schematic of shunting model. where i_k is source current, V_{sj} $(j = 1.2.\ldots.,q)$ is inhibitory input, i_e is generator current, and i_{sj} $(j = 1.2.\ldots.q)$ is shunted current.

Combining the above equations together yields

$$\frac{C}{G_\epsilon}\frac{di_\epsilon}{dt} + [1 + \frac{1}{G_e}\sum_{j=1}^{q} m_j V_{sj}]i_\epsilon = i_k \tag{4.3}$$

If V_{sj} varies with time, (4.3) is a time varying differential equation. If V_{sj} is a function of i_k, (4.3) becomes a nonlinear differential equation. If in the simple case, we assume that V_{sj} is constant, then we have the following transfer function:

$$\frac{I_e(s)}{I_k(s)} = \frac{G_e/C}{s + (G_e/C + \frac{1}{C}\sum_{j=1}^{q} m_j V_{sj})} \tag{4.4}$$

In periodic steady-state operation, the above equation means that increasing the inhibitory signal V_{sj} will decrease the gain and advance the phase shift.

The shunting inhibition model above shows how the local inhibitory signals modify the directly mediated signals. In the real visual system, because of complicated neuronal organization, inhibitory activity in the cortical neural network that produces the VEP may not be described simply by a single cell inhibition model. However, it is a reasonable expectation that the inhibitory phenomena observed in the VEP, to some extent, may still reflect the inhibitory activities in the single cells,

that is. an increase of inhibitory signal will decrease the gain and advance the phase characteristic of the neural system.

4.5 Summary of Inhibitory Mechanism Investigation

Analysis of lateral interactions may be achieved by treating the excitatory process and inhibitory process as two distinct pathways. Following this strategy, a model that describes lateral inhibitory paths was proposed in Figure 4.8.

Prior studies of inhibitory activities in the neural signal processing were reviewed. Those researches showed that both contrast gain control and lateral interaction will modify the temporal characteristics of the visual pathway. in particular, the effects of those inhibitory mechanisms on the VEP difference frequency components mainly result from the inhibitory activities in the cortex (Zemon, Conte & Camisa. 1987). Experiments conducted were performed on two subjects in this work to demonstrate the inhibition phenomena in the VEP. A shunting inhibition model was used to qualitatively describe such inhibition phenomena.

CHAPTER 5
SYSTEM IDENTIFICATION

The procedure of system identification will be divided into four steps, namely i) model construction, ii) selection of criterion for fit, iii) parameter estimation and iv) model validation (Ljung, 1987).

The model is constructed based on observed data and prior knowledge of the physical system. This is no doubt the most important and difficult step in the system identification procedure. It is here that a prior knowledge and engineering intuition and insight have to be combined with formal properties of the model. Particularly, for a complicated system, premodeling and reconstruction will sometimes be necessary until one finds a proper model to describe the system. In fact, it was the situation in our system modeling.

The second step, the choice of criterion for fit, is to set up a rule by which the candidate model can be assessed by using the observed data. There are varieties of methods to organize such assessment, and different methods may give different estimation results. Detailed discussions on this aspect can be referred to the text book by L. Ljung (1987).

The third step, parameter estimation, is to determine the model parameters by carrying out the response fitting procedure. Even with a good model structure and a proper fitting criterion, special fitting strategies should be considered to achieve correct convergence.

The final step, model validation, includes evaluation of how the model relates to the observed data, as well as establishment of the classes and ranges of stimuli for which the model is valid. All the above steps are included in the logical flow diagram as Figure 5.1 shown. Each step will be discussed in detail in the following sections.

In the system identification, although we desired a general type of transfer function for the model, the observed interindividual differences in the two-sinusoid stimulation test (Figure 3.5, Figure 3.6) necessitated incorporation of specific subject

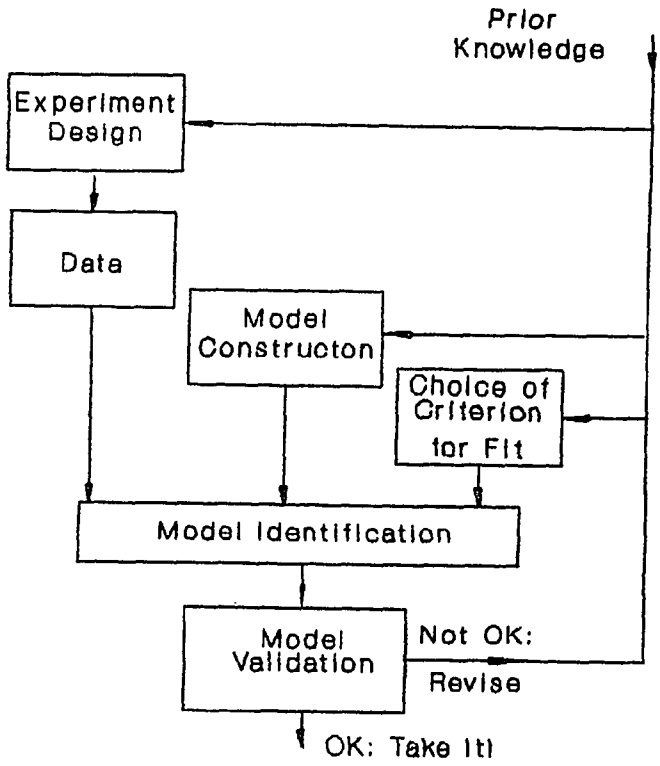

Figure 5.1 System identification loop.
Adapted from the book by Ljung, 1987.

attributes into the equation coefficients. In this case, the coefficients in the transfer functions will be subject dependent. We express, therefore, the transfer function type according to the common features of the VEP responses (sum and difference frequency components) measured from the group of ten subjects, and illustrate the parameter estimation for two specific subjects to obtain a protocol for VEP modeling.

5.1 Model Construction

5.1.1 Model Structure Consideration

As discussed in the previous chapters, there are several major mechanisms in the visual system that account for the generation of the VEP. Excitatory processes are involved in signal transmission through successive stages from the retina to the brain. Two types of inhibitory processes, contrast gain control and lateral interaction, are

known to modify the neural signal transmission. The contrast gain control exists in both the retina and the cortex, while the dominant lateral interaction is located in the cortex. A block diagram that depicts such neuronal signal processing is shown in Figure 5.2.a.

In the diagram, the signal direct-through process is expressed by a traditional sandwich model.

The initial filter H_1 represents the transfer characteristics of early stages of the visual pathway, including the retina, lateral geniculate nucleus (LGN) and front stage of the cortex. H_1 is segregated further into three elements, H_{1a}, H_{1b} and F, to represent the process of the contrast gain control in the retina. Evidence has been shown that the contrast mechanism in the retina receives the signals generated by some bipolar subunits and feedbacks to modulate the behavior of the front end of the subunits due to numerous amacrine-to-amacrine and amacrine-to-bipolar synapses*(Levick, 1975; Kolb, Famiglietti & Nelson, 1976). Hence, element F represents the feedback pathway of the contrast gain control in the retina, H_{1a} and H_{1b} represent the transfer characteristic before and after the feedback loop respectively. H_{1b} is a linear transducer, H_{1a} is a transducer with parameters controlled by the feedback signal from F.

Since we assume that the rectification process resides in the cortical level, the second filter H_2 following the rectifier represents transfer characteristic of the last stage in the cortex. Element G performs the contrast gain control in the cortex (see Section 4.2), while element L represents a lateral inhibitory pathway (see Section 4.3). The input of element G has not been decided, it can come from an earlier stage or feedback from a later stage. The parameters of the element H_2 are controlled by the inhibitory signals from both G and L.

The model above describes the neural message process in more detail than the sandwich model does. However, the VEP response elicited by the two-sinusoid

*Amacrines are the neuronal cells located between the bipolar layer and the ganglion layer in the retina, which play a function of modifying the activity at the junction between the bipolar cells and the ganglion cells (e.g. Masland, 1986).

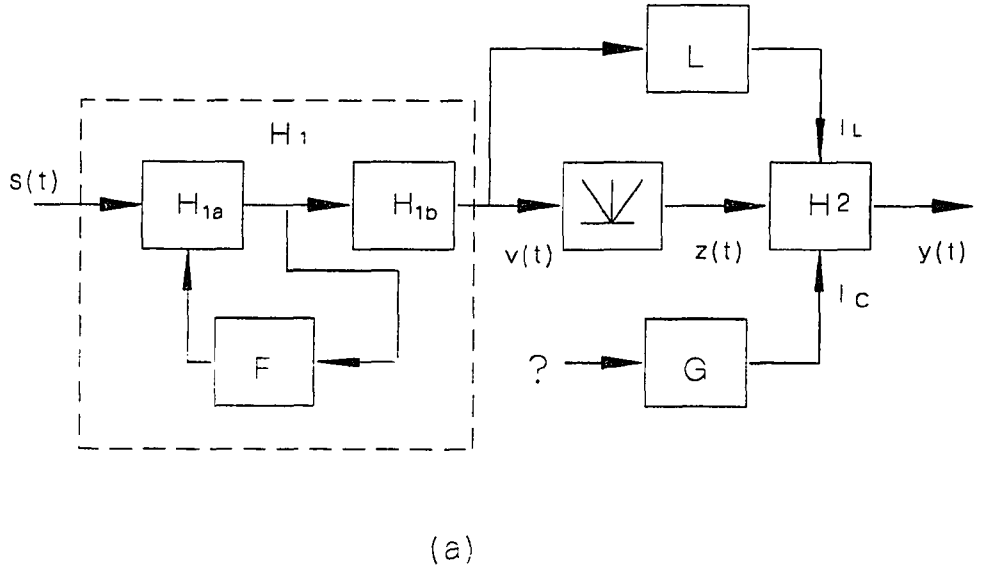

(a)

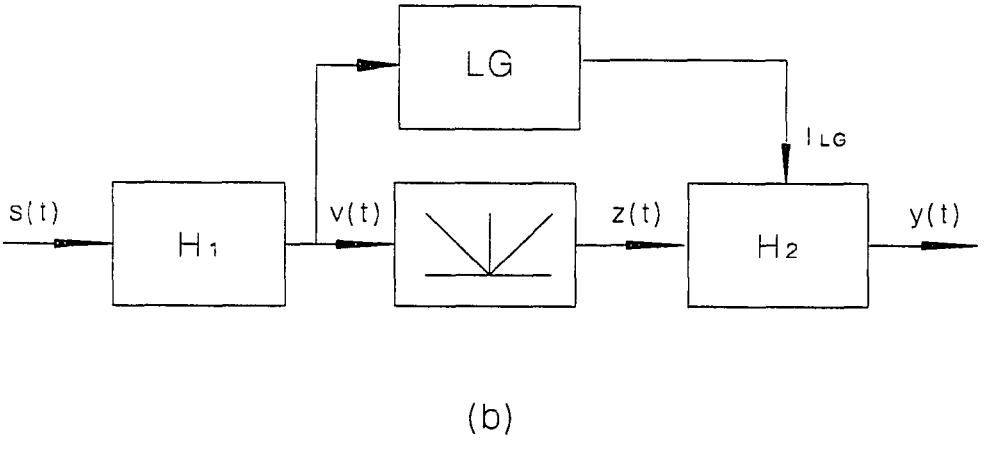

(b)

Figure 5.2 a: A block diagram of VEP generator containing excitatory process and two types of inhibitory processes. **b:** A simplified model containing one inhibitory process.

input. does not supply sufficient information for identifying each block in Figure 5.2.a. In searching for an adequate model that can explain the visual system's behavior including the excitatory and inhibitory processes, yet simple enough for analysis, two considerations regarding inhibitory processes in the retina and the cortex are made.

First, we note: Victor, in his work for modeling the dynamic behavior of cat retina X cells (Victor, 1987) and Y cells (victor, 1988), demonstrated that, although the model parameters depend on the stimulus contrast level, such models with parameters estimated at low contrast *frequency* response can predict the low contrast *transient response*, and so do the models with parameters determined for high contrast frequency response. This fact suggests that, if the stimulus contrast is kept at the same level during each test in our modeling, the effect of contrast gain control in the retina will not be significant, and therefore need not necessarily be taken into account, or it can be merged into the effect of contrast mechanism in the cortex. The transfer characteristics of H_1 can then be approximated as a purely linear process.

Second, we consider both inhibitory mechanism blocks L and G affecting H_2. i) We assume that the contrast gain control G measures the signal contrast from H_1: this means that both elements L and G have the same input. ii) Both lateral interaction and contrast gain control essentially have the same inhibitory effect on the signal transmission; namely an increase of inhibitory signal causes the forward signal to decrease in magnitude and to advance in phase (Section 4.2, 4.3). Thus, these two blocks can be combined into one. A simplified model based on the above discussion is illustrated in Figure 5.2.b, in which, LG is the block combined from element L and G.

Phase change due to LG

To describe the phase decrease of the DFC in the two-sinusoid stimulation test using the model in Figure 5.2, we hypothesize: in the mid-frequency region around 15 Hz, as f_1 increases, the signal from the lateral inhibitory pathway L decreases due to the bandpass nature of L (Section, 4.3), which causes the DFC phase to decrease. In the high frequency region above 20 Hz, as f_1 increases, the signal from contrast gain

control G decreases due to the gain character of H_1, which causes the DFC phase to decrease further. The combination of these effects thus presents a monotonic phase decrease in the region above 15 Hz. Therefore, in the model of Figure 5.2.b. the transfer function of LG should be properly constructed so that the phase decrease of the DFC response results from the inhibitory modification through LG.

5.1.2 Identification of Subsystem – Inhibitory Function

To set up a relation between the inhibitory signal from the block LG and its dependent parameters in H_2, element H_2 is segregated into two subsystems in cascade. One is a linear filter, the other contains the parameters which are controllable by the inhibitory signal. Since the inhibitory mechanisms affect both signal amplitude and phase, the transducer with controllable parameters is further segregated into two consequent blocks, namely a *magnitude modulator* and *phase modulator*. A block diagram of this H_2 stage model is illustrated in Figure 5.3.

In this model, H_{2L} is simply a linear transducer; H_{2P} is a phase modulator whose parameters depend on the inhibitory signal I_{LG}. H_{2A} is a zero memory magnitude modulator whose gain depends on inhibitory signal I_{LG}. I_{LG} is defined as a constant in steady-state operation, but its value varies with the input frequency.

The input-output relation of H_{2P} is defined as

$$G(s) = \left[\frac{s-(p_1+p_2 I_{LG})}{s+(p_1+p_2 I_{LG})}\right]^N Z(s) = H_{2P}(s, I_{LG}) Z(s) \tag{5.1}$$

where p_1 p_2 are constant coefficients, and N is an integer. Since I_{LG} is a constant in steady-state, for sinusoidal input $z(t)$, the output $g(t)$ is also a sinusoid with I_{LG} dependent phase but the same amplitude of the input.

The input-output relation of H_{2A} is defined as

$$X(s) = \frac{p_3}{p_4 + I_{LG}} G(s) = H_{2A}(I_{LG}) G(s) \tag{5.2}$$

where p_3 and p_4 are constant coefficients. For a sinusoidal input $g(t)$, if I_{LG} is fixed in steady-state, the output $x(t)$ is also a sinusoid with I_{LG} dependent amplitude but the same phase of the input.

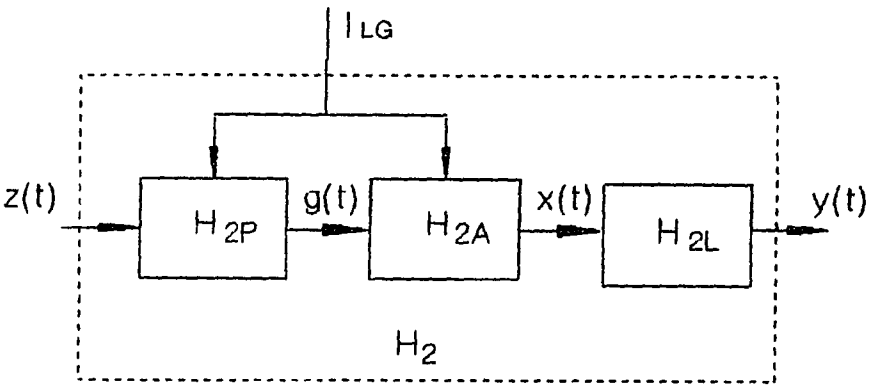

Figure 5.3 A block diagram of transducer H_2 which can be divided into two consequent processes, nonlinear and linear process. The nonlinearity consists of an amplitude modulator and a phase modulator both controlled by an inhibitory signal I_{LG}.

This separately controlled amplitude-phase model offers a distinct convenience to identify the linear element (H_{2L}). Suppose input $z(t)$ contains a difference frequency component (DFC) and a sum frequency component (SFC). Since H_{2A} changes the amplitudes of moth DFC and SFC in the same scale. while H_{2P} doesn't change the amplitudes at all. the DFC and SFC in the output $x(t)$ from these modulators retain the same ratio as that for input $z(t)$. Hence, the ratio of SFC and DFC (equation (2.17)) is still valid to determine the gain characteristic of the second linear element H_{2L}.

To determine the parameters of the modulators, one notes that, for two-sinusoid input. the phase and amplitude of the difference frequency component produced from the system are, respectively

$$\phi_{yDFC}(f_1, f_2) = N\pi - 2N \arctan\left[\frac{2\pi(f_2 - f_1)}{p_1 + p_2 I_{LG}}\right] + \angle H_{2L}(f_2 - f_1) + \phi_{zDFC}(f_1, f_2) \quad (5.3)$$

and

$$A_{yDFC}(f_1, f_2) = \frac{p_3}{p_4 + I_{LG}} |H_{2L}(f_2 - f_1)| A_{zDFC}(f_1, f_2) \quad (5.4)$$

Now if the input frequencies f_1 and f_2 are fixed, then $|H_{2L}(f_2-f_1)|$, $\angle H_{2L}(f_2-f_1)$ and $\phi_{zDFC}(f_1,f_2)$ in the above equations are constant. Because I_{LG} and $A_{zDFC}(f_1,f_2)$ are proportional to the stimulus contrast C_w, we denote

$$I_{LG} = M_1 C_w \tag{5.5a}$$

$$|H_{2L}(f_2-f_1)|A_{zDFC}(f_1,f_2) = M_2 C_w \tag{5.5b}$$

where M_1 and M_2 are constant. Equations (5.3) and (5.4) can be simplified as

$$\phi_{yDFC}(f_1,f_2) = -2N \arctan\left[\frac{2\pi(f_2-f_1)}{p_1+p_2 M_1 C_w}\right] + M_3 \tag{5.6}$$

and

$$A_{yDFC}(f_1,f_2) = \frac{p_3}{p_4+M_1 C_w} M_2 C_w \tag{5.7}$$

where $M_3 = N\pi + \angle H_{2L}(f_2-f_1) + \phi_{zDFC}(f_1,f_2)$ is a constant.

Equations (5.6) and (5.7) indicate: by fixing f_1, f_2 and varying the stimulus contrast C_w, the change in amplitude and phase of DFC can help one to determine the coefficients p_1, p_2, p_3 and p_4. M_1 and M_2 in (5.6) and (5.7) are related to the transfer gain of H_1, LG and H_{2L} at particular frequency, for convenient purpose, they can be set to unit value. Since the model is developed to fit the phase change rather than phase value of the DFC*, M_3 can be any arbitrary constant.

According to the discussion above, we divide the system parameter estimation into two steps. In the first step (we call it pre-parameter estimation), we use the two-sinusoid stimulus with a fixed frequency pair at different contrast levels to determine the coefficients p_1, p_2, p_3 and p_4. In the second step, with fixed coefficients p_1, p_2, p_3 and p_4, we use a modified two-sinusoid technique to identify the transfer characteristics of H_1, LG and H_{2L}. The modification, considering that one more element LG is included in the model, will be presented in the next section.

The identification of coefficients p_1, p_2, p_3 and p_4 was done as follows: The stimuli contained two superimposed sinusoids with contrasts of 0%, 5%, 10%, 20%,

*Equation (2.16a) used to determine the phase characteristic of H_1 contains an unknown constant $\phi_{yDFC}(f_1,f_2)$.

30% and 40%. The frequency pair was fixed to $f_1 = 18.95$ Hz and $f_2 = 20.94$ Hz. Other conditions were the same as those described in Chapter 2.

It should be mentioned:

1. The reason to set the stimulus frequency pair around 20 Hz is that the VEP difference frequency component may have a maximum response at this frequency, which is relatively reliable and accurate due to high signal to noise ratio.

2. In the model, I_{LG} represents the inhibitory signals of both contrast gain control and lateral interaction. Although the estimation of the coefficients in the phase modulator and amplitude modulator are guided by the contrast varying test, since we assume that both inhibitory mechanisms have similar nonlinear effect on the signal transmission within certain frequency region, that is, an increase of inhibitory signal will decrease the transfer gain and advance the phase of the system. Therefore, the parameter dependence on the inhibitory signal I_{LG}, obtained in the above experiment, essentially represents the general rule of neural inhibitory activity, either for the contrast gain control or the lateral interaction.

Difference frequency component data were derived by Fourier transform for the VEP records. Two subjects A and B, whose data are utilized in the modeling, were tested to obtain the subject dependent coefficients p_1, p_2, p_3 and p_4. Data were measured at two different times. Each time, the test was conducted twice. The first one ran in ascending order from low contrast to high contrast; the second one in descending order from high contrast to low contrast. The amplitude response corresponding to zero contrast input was set to zero. Averaged data over total four measurements, marked by circles, together with their radius of error circle and phase error range, are plotted in Figure 5.4.1 for subject A and Figure 5.4.2 for subject B.

Because the phase modulator also provides a phase shift to the sum frequency component (SFC), its order N should be selected so that the phase modulator co-

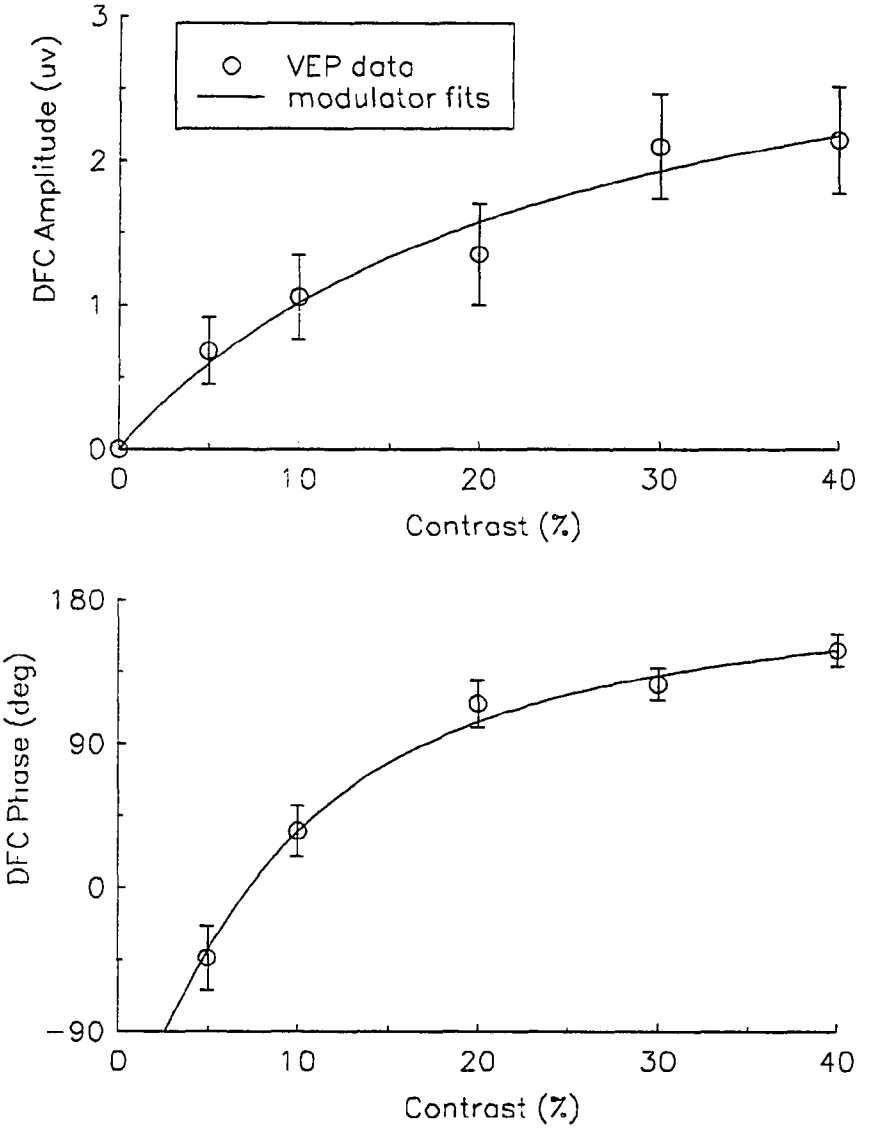

Figure 5.4.1 Contrast experiment data for determining the parameters of inhibitory modulators. DFC of VEP were measured from subject A by using superimposed two-sinusoid stimuli with fixed frequency pair of f_1=18.95 Hz, f_2=20.94 Hz and variable contrast set to 0%, 5%, 10%, 20%, 30% and 40%. Test was run at two separate times and repeated twice in each time. Averaged data over total four measurements, marked by the symbol of circle, are plotted versus stimulus contrast. Amplitudes are plotted with their radius of *error circle*, phases are plotted with their error range. The fitting curves were obtained by least-square method and are plotted in solid curves.

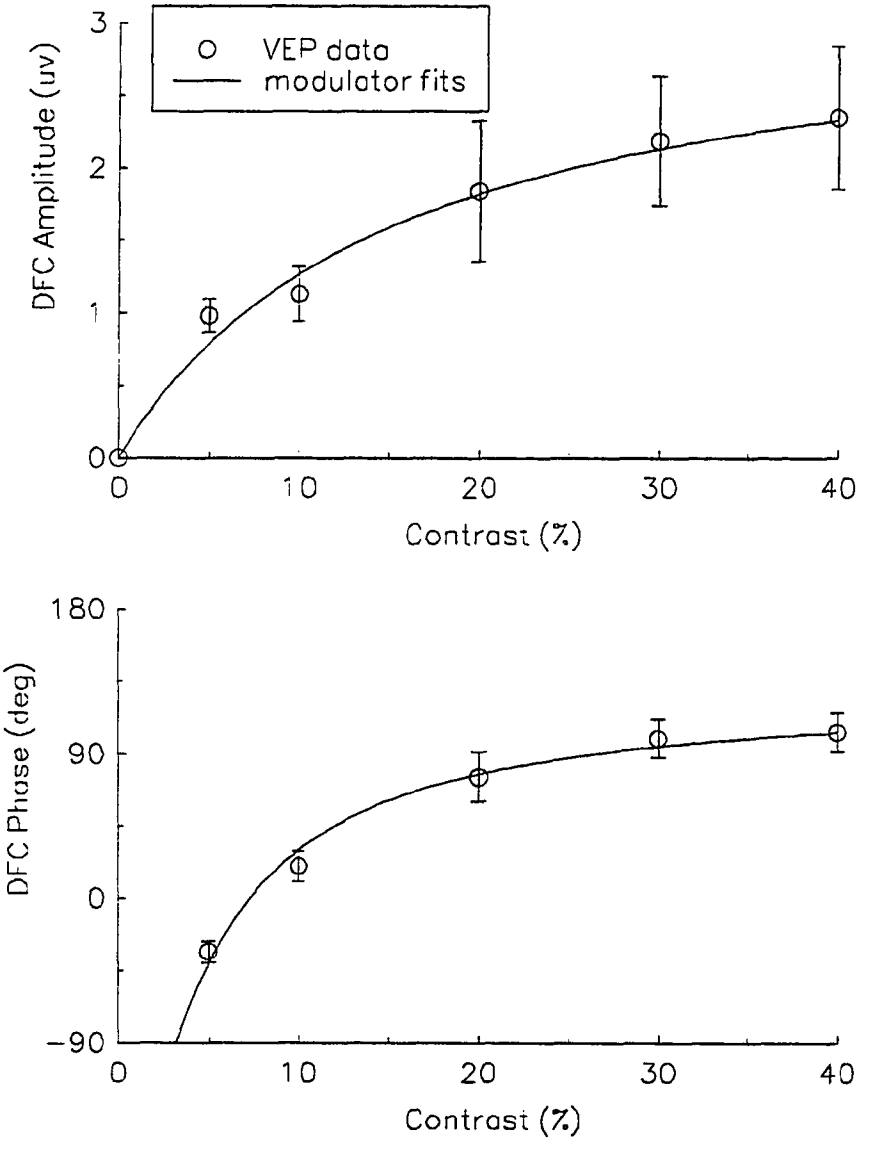

Figure 5.4.2 Contrast experiment data for determining the parameters of inhibitory modulators. DFC of VEP were measured from subject B by using superimposed two-sinusoid stimuli with fixed frequency pair of f_1=18.95 Hz, f_2=20.94 Hz and variable contrast set to 0%, 5%, 10%, 20%, 30% and 40%. Test was run at two separate times and repeated twice in each time. Averaged data over total four measurements, marked by the symbol of circle, are plotted versus stimulus contrast. Amplitudes are plotted with their radius of *error circle*, phases are plotted with their error range. The fitting curves were obtained by least-square method and are plotted in solid curves.

operating with the time delay in the system can provide a fit for the phase response of SFC. However, the time delay should be maintained in a proper value so that the model can also match the VEP transient response (to be discussed in Chapter 6). Therefore. After several tries of premodeling. it has been found that $N = 4$ provides reasonable matching. Least-square fitting was used to determine parameters p_1 to p_4. Parameters p_1 and p_2 were obtained by phase curve fitting with equation (5.6). Parameters p_3 and p_4 were determined by amplitude curve fitting with (5.7). Curves of model fits are plotted in solid line in Figure 5.4. The parameters identified are listed in Table 2.

Table 2 Parameters of inhibitory modulator

	p_1	p_2	p_3	p_4
subject A	0.678	4.587	3.489	24.379
subject B	0.155	6.704	3.218	15.374

5.1.3 The Strength of Inhibitory Signal

In Chapter 4, we indicated that a signal in the direct-through pathway at one frequency will be modified by an inhibitory signal at another frequency. This intermodulation modification depends on the strength of the inhibitory signal, which may be considered a measure of inhibitory signal contrast. Therefore, in the model of Figure 5.2.b, signal I_{LG}, which acts as a parameter in the magnitude and phase modulator, should be a measure of the signal contrast passing through the inhibitory path LG.

Now if the inhibitory signal consists of several sinusoids, what is its strength, average value, effective (RMS) value, or energy? Because all of these values are described in a steady-state category, and are related to each other, increase or decrease in one value means the same result in the other values. Whatever measure is selected as a definition of signal strength does not substantially influence the model identification. However, when the model is used to predict the response elicited by another type of stimulus other than the two-sinusoids, the contrast of the stimulus should be set so that the total inhibitory influence caused by contrast gain control in the retina is equivalent to that corresponding to the two-sinusoid stimulus. Otherwise,

the effect of contrast gain control in the retina will differ in each test, and it cannot be omitted from the model. Therefore, when the model's prediction is checked by comparing the observed response elicited by different stimuli, the equivalent contrast should be determined and used. Naturally, the definition of inhibitory signal strength, I_{LG}, should be expressed in terms of such equivalency.

In prior studies of modeling X and Y type ganglion cells of the cat retina, Victor (1987; 1988) demonstrated that either frequency response or transient response depend on stimulus contrast. A model identified in terms of the cell's frequency response to low contrast stimuli essentially generates a close match to the step response measured at low contrast, but it substantially deviates from the observed step response to high contrast stimuli. Similarly, a model based on the frequency response measured at high contrast can only produce a good fit for the observed step response to high contrast stimuli, particularly when the step function stimulus and sinusoidal stimulus have the same root-mean squared (RMS) values of the modulating signals $s(t)$. This finding leads to the hypothesis that stimuli with identical RMS values of the modulating signals produce equivalent contrast gain control in the retina.

Based on this assumption, we define the signal I_{LG} as RMS value of the inhibitory modulating signal. A model of the inhibitory path, LG, based on the above consideration, is proposed in Figure 5.5.a, here, H_3 is a linear transducer, representing the linear process in the inhibitory path; M is an algorithm element which converts the inhibitory signal $q(t)$ into its RMS value, I_{LG}; that is

$$I_{LG} = M[q(t)] = \lim_{T\to\infty} \sqrt{\frac{1}{T}\int_0^T q^2(t)dt} \tag{5.8a}$$

or

$$I_{LG} = \sqrt{A_1^2 + A_2^2 + \cdots + A_n^2}/\sqrt{2} \tag{5.8b}$$

where $A_1, A_2, \ldots, A_n$ are the amplitudes of the sinusoids consisting in $q(t)$. Since the system input $s(t)$ does not contain DC component, $q(t)$ does not contain DC component either. I_{LG} is a measure of overall contrast of the inhibitory signal $q(t)$.

In the physical visual system, the inhibitory process in the cortex may not

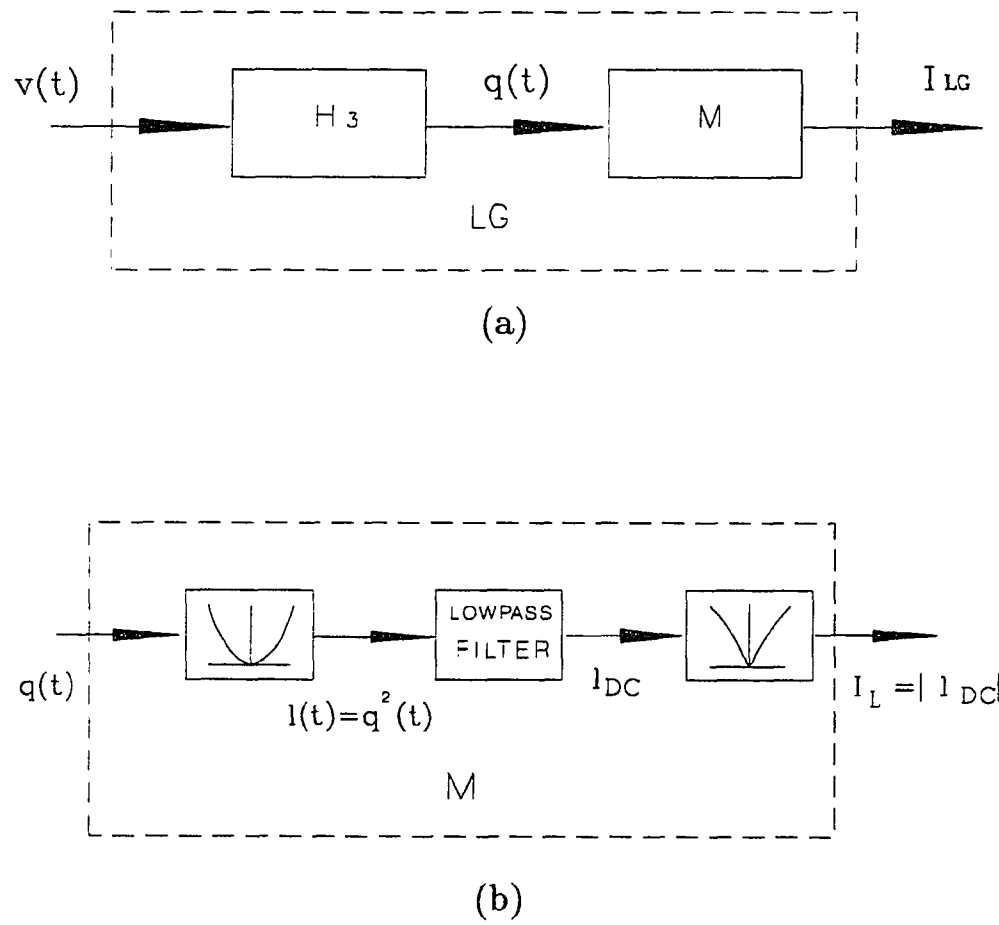

Figure 5.5 a: Inhibitory path containing a linear transducer H_3 and a converter M. **b:** A subsystem M that, in steady-state, transforms the input signal to its root-mean squared (RMS) value.

be necessarily described by algorithm (5.8), yet for the system modeling, we feel this algorithm, together with modulators H_{2A} and H_{2P}, may conveniently suite description of the inhibitory process under steady-state condition. Therefore, we accept this algorithm just as we accept equation (3.4) to approximate the input-output relation of the rectifier. The difference is that (3.4) is derived based on the rectification characteristic, while (5.8) is derived based on the experimental results.

A physically realizable subsystem that can equivalently fulfill such signal transformation is shown in Figure 5.5.b. In the system, the first element is quadratic full-wave rectifier with input-output relation $l(t) = q^2(t)$; The second element is a lowpass filter with a sufficient low corner frequency to extract the DC component from $l(t)$; The third element is a square-root rectifier that produces output $I_{LG} = |l_{DC}|^{\frac{1}{2}} = \lim_{T-\infty} \sqrt{\frac{1}{T}\int_0^T q^2(t)dt}$.

A completed model for describing VEP generating in steady-state operation is shown in Figure 5.6. In the model, H_1, H_{2L} and H_3 are linearities whose transfer functions are determined in the identification procedure described later.

5.2 Choice of Criterion for Fit

To identify the parameters in the model, least-square fitting is used. Suppose n tests are conducted at different frequency pairs, $f_1 = \eta_i$ and $f_2 = \eta_i + 2 =$ Hz $(i = 1, 2, \cdots, n)$. We denote the corresponding averaged Fourier components of the VEP as $\overline{Y}_i$; the model response as

$$\hat{Y}_i = \xi(\eta_i, \theta) \tag{5.9}$$

where θ is a vector of parameters in the model to be determined, and ξ is the model equation which correlates the model output $\hat{Y}_i$ and the variables η_i and θ. $\overline{Y}_i$ and $\hat{Y}_i$ may represent either the DFC or the SFC. The criterion function is given by

$$R_n(\theta) = \sum_{i=1}^{n} [\overline{Y}_i - \xi(\eta_i, \theta)]^2 \tag{5.10}$$

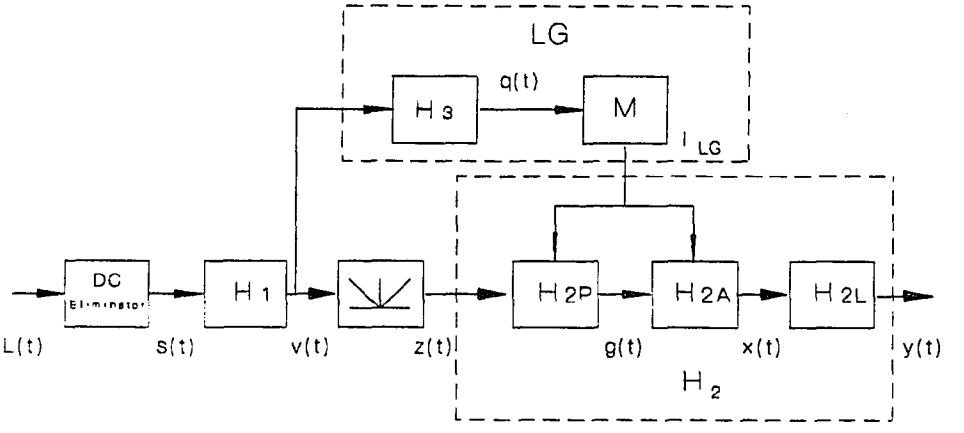

Figure 5.6 VEP frequency response model, which contains a direct-through pathway and a parallel inhibitory pathway. The direct-through pathway consists of a linear transducer H_1 followed by a rectifying nonlinearity N and an inhibitory signal dependent transducer H_2. The inhibitory pathway is formed by a linear transducer H_3 and a converter M. components of the blocks are defined in detail in Table 3.

Table 3 Characteristics of each element in the model guided by frequency responses.

H_1:	$V(s)=\frac{(s+b_0)k_0}{s+a_0}(\frac{1}{s^2+a_1 s+a_2})^2(\frac{1}{s^2+a_3 s+a_4})^2 \exp^{-sT} S(s)$
N :	$z(t) = N[v(t)] = \lvert v(t)\rvert$
H_{2P} :	$G(s) = [\frac{s-(p_1+p2I_{LG})}{s+(p_1+p_2I_{LG})}]^4 Z(s)$
H_{2A} :	$X(s) = \frac{p_3}{p_4+I_{LG}} G(s)$
M :	$I_{LG} = M[q(t)] = \lim_{T\to\infty} \sqrt{\frac{1}{T}\int_0^T q^2(t)dt} = \sqrt{< q^2(t) >_{AVE}}$
H_{2L} :	$Y(s) = \frac{(s+b_1)k_1}{s+a_5}\frac{1}{s^2+a_6 s+a_7}\frac{1}{s^2+a_8 s+a_9} X(s)$
H_3 :	$Q(s) = \frac{k_2 s^2}{(s^2+a_{10}s+a_{11})^2} V(s)$

where $R_n(\theta)$ is a sum of residuals which should be minimized by adjusting the parameter vector θ. The unique feature of this criterion, developed from the linear parameterization and quadratic criterion, is that it is a quadratic function in θ, which, therefore, can be minimized analytically. In the practical identification procedure, the criterion equation (5.10) may be modified. Different weights W_i can be assigned to the residuals, yielding a criterion equation

$$R_n(\theta) = \sum_{i=1}^{n} W_i[\overline{Y}_i - \xi(\eta_i, \theta)]^2 \tag{5.11}$$

The reasons to consider weighted least-square method are:

1. The observations $\overline{Y}_i$ could be of varying reliability. The degree of disturbance in some observations could be subject to change, or that certain measurements are less representative of the system's properties. In such case, the observations should be down weighted.

2. The observations could be of varying relevance. This is because the model is proposed and identified according to the data we measured over the entire testing region, but the corresponding fitting curve may not exactly fit every observation. In some particular testing region, the model may not hold. Therefore, an observation in such questionable region, even if accurate, should carry less weight.

Reviewing the VEP data measured from the ten subjects (Figure 3.5, 3.6), one finds, for the phase response of DFC, that all the response curves are relatively consistent in the high frequency region, presenting a negative slope, but possess a large variance in the low frequency region below 10 Hz. One reason is that the VEP frequency responses have low sensitivity in the low frequency region, and easy to be contaminated by noise. Such phenomena can also be seen from the repeated test on single subject. Figure 5.7 shows a set of difference frequency component (DFC) data measured six times from subject B. In this experiment, measurements were carried out in three different times. Each time, DFC corresponding to each frequency point was

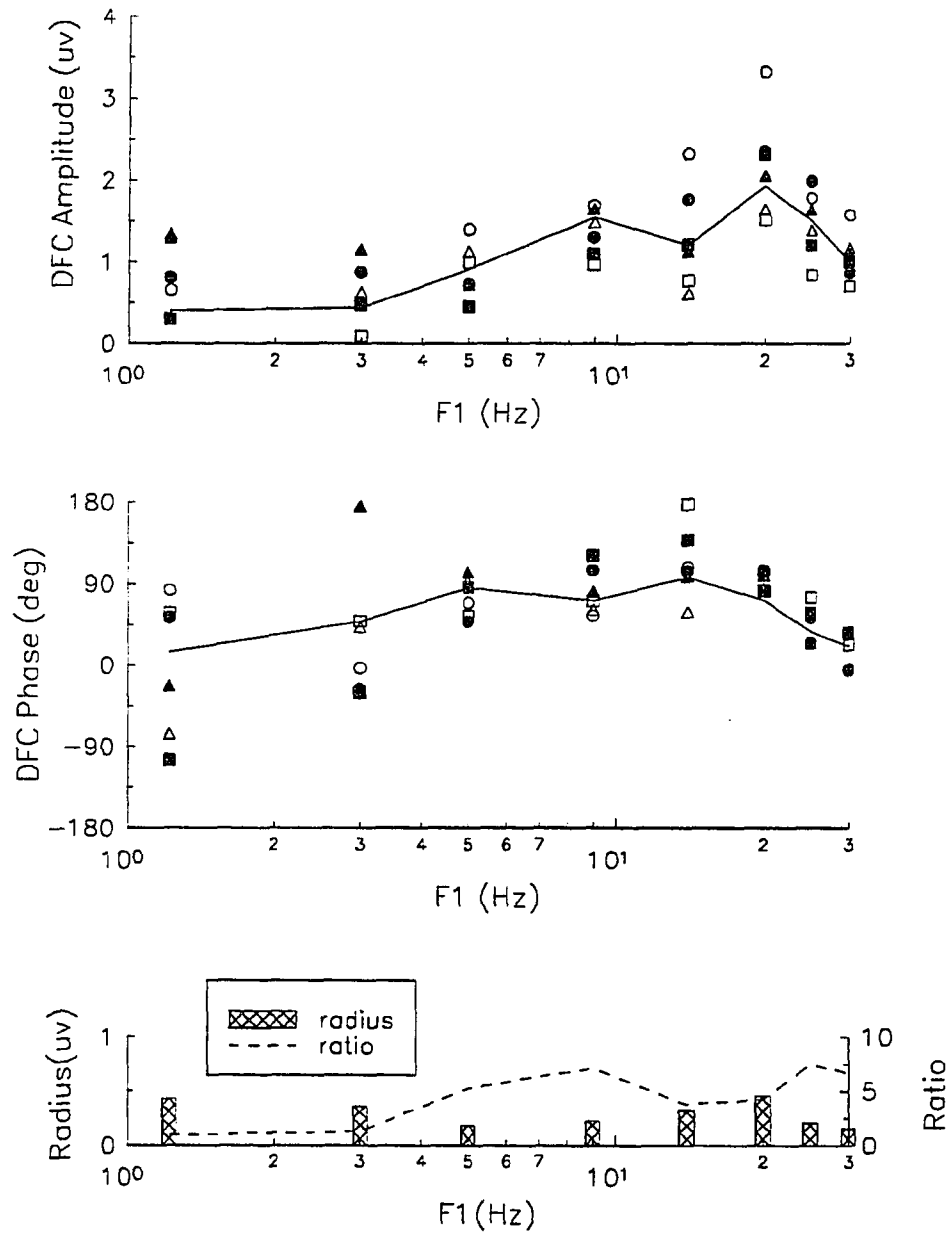

Figure 5.7 Experiment of VEP reliability investigation. Stimuli were of two-sinusoids in superimpos. The separation of two frequencies was 1.99 Hz. The sampling frequencies were set to f_1=1.22. 2.99, 4.99, 8.98, 13.96, 19.95, 24.93 and 29.92 Hz. Test repeated twice on subject B at three different times. Each test ran 32.08 seconds. DFC were obtained by Fourier analysis on recorded VEP data and are plotted in top for amplitude and middle for phase. The data collected at different time are marked by the symbols of circle, box and triangle respectively. In each time, two sets of repeated measurements are marked by unfilled and filled symbols respectively. Vector-averaged data are plotted in solid line. The radius of *error circle* r_{circ} and the ratio of the amplitude of the averaged response and r_{circ} are plotted in bars and dash line respectively in the bottom.

measured twice, one was forward (from low frequency point to high frequency point), the other was backward (from high frequency point to low frequency point). Each test ran 32.08 seconds. The data measured at different times and in different orders are marked by different symbols. The vector-averaged data over the six measures are linked by a solid line. The radii of *error circles*, r_{circ}, at each frequency point are marked by bars. The ratios of the amplitude of the averaged response and r_{circ} are linked by a dash line.

The data show i). Even though there is a variance between each single recordings. except for the phase response at low frequencies below 5 Hz, the response curve shapes. are essentially consistent with each other. ii). The ratios of the amplitude of the averaged response and r_{circ}, which reflect the signal to noise ratio. is much lower in the region below 5 Hz than in the another region.

Therefore, instead of averaging large numbers of repeated records to get rid of noise in the low frequency region, we assign a lower weight to the measurements in that questionable region and higher weight to the others in order to guide the system identification by reliable and consistent data. In this work, the weighting function is defined as the ratio of the mean amplitude of DFC (calculated from (2.32a)) and the radius of *error circle* (calculated from (2.37)), that is,

$$W_i = \frac{A_{yDFC}(\eta_i, \eta_i + 2)_{AVE}}{r_{circ}(\eta_i)} \tag{5.12}$$

where $A_{yDFC}(\eta_i, \eta_i + 2)_{AVE}$ is the mean amplitude of DFC at the ith frequency pair $(\eta_i, \eta_i + 2)$, and $r_{circ}(\eta_i)$ is the radius of *error circle* at the ith frequency pair. For the sum frequency components, the same procedure is followed to obtain the weighting function.

5.3 Parameter Estimation

There are three subsystems in the model to be identified, namely the linear filters H_1. H_3 and H_{2L}. Since more blocks are included in the model, the equations for the sandwich system should be modified. We denote the gain and phase characteristic

of those linear filters as $|H_1(f)|$, $\angle H_1(f)$, $|H_3(f)|$, $\angle H_3(f)$, $|H_{2L}(f)|$ and $\angle H_{2L}(f)$ respectively. For the system input

$$s(t) = C_w[\sin(2\pi f_1 t) + \sin(2\pi f_2 t)] \tag{5.13}$$

where C_w is the depth of modulation which is 30%, the amplitudes and phases of DFC and SFC produced from the rectifier are given by equations (3.5), (2.16), (2.17), that is

$$A_{zDFC}(f_1, f_2) = \Gamma[C_w|H_1(f_1)|, C_w|H_2(f_2)|] \tag{5.14}$$

$$A_{zSFC}(f_1, f_2) = A_{zDFC}(f_1, f_2) = \Gamma[C_w|H_1(f_1)|, C_w|H_2(f_2)|] \tag{5.15}$$

$$\phi_{zDFC}(f_1, f_2) = \angle H_1(f_2) - \angle H_1(f_1) + \frac{\pi}{2} \tag{5.16}$$

$$\phi_{zSFC}(f_1, f_2) = \angle H_1(f_1) + \angle H_2(f_2) - \frac{\pi}{2} \tag{5.17}$$

Since H_3 linearly filters the signal from H_1, the amplitudes of the two sinusoids produced from H_3 are $C_w|H_1(f_1)||H_3(f_1)|$ and $C_w|H_1(f_2)||H_3(f_2)|$. The inhibitory signal generated from block M, according to (5.8b), is given by

$$I_{LG} = C_w\sqrt{|H_1(f_1)|^2|H_3(f_1)|^2 + |H_1(f_2)|^2|H_3(f_2)|^2}/\sqrt{2} \tag{5.18}$$

Finally, the difference frequency component and sum frequency component from the entire system, according to (5.3) and (5.4), are given by the equations

$$A_{yDFC}(f_1, f_2) = \frac{p_3}{p_4 + I_{LG}}\Gamma[C_w|H_1(f_1)|, C_w|H_1(f_2)|]|H_{2L}(f_2 - f_1)| \tag{5.19}$$

$$\phi_{yDFC}(f_1, f_2) = \angle H_1(f_2) - \angle H_1(f_1) + \frac{9}{2}\pi - 8\arctan\frac{2\pi(f_2 - f_1)}{p_1 + p_2 I_{LG}} + \angle H_{2L}(f_2 - f_1) \tag{5.20}$$

$$A_{ySFC}(f_1, f_2) = \frac{p_3}{p_4 + I_{LG}}Gamma[C_w|H_1(f_1)|, C_w|H_1(f_2)|]|H_{2L}(f_1 + f_2)| \tag{5.21}$$

$$\phi_{ySFC}(f_1, f_2) = \angle H_1(f_1) + \angle H_1(f_2) + \frac{7}{2}\pi - 8\arctan\frac{2\pi(f_1 + f_2)}{p_1 + p_2 I_{LG}} + \angle H_{2L}(f_1 + f_2) \tag{5.22}$$

The ratio of sum frequency component and difference frequency component is then

$$\frac{A_{ySFC}(f_1, f_2)}{A_{yDFC}(f_1, f_2)} = \frac{|H_{2L}(f_1 + f_2)|}{|H_{2L}(f_2 - f_1)|} \tag{5.23}$$

For a given input of two-sinusoids in (5.13), when $f_2 - f_1$ is a constant. the gain $|H_{2L}(f_2 - f_1)|$ and phase shift $\angle H_{2L}(f_2 - f_1)$ are constant too. Therefore, (5.19) and (5.20) provide the rules for identifying H_1 and H_3 according to the observed difference frequency components. while (5.23) provides a rule for identifying $|H_{2L}(f)|$ according to the observed amplitude ratios of sum frequency component and difference frequency component. Once those have been done, equation (5.22), together with (5.19), (5.20) and (5.23), offer additional rules for adjusting the parameters in all the three elements H_1. H_3 and H_{2L} simultaneously. In the procedure of parameter estimation, a unit value and an arbitrary constant are assigned to $|H_{2L}(f_2 - f_1)|$ and $\angle H_{2L}(f_2 - f_1)$ respectively. so that relative values of DFC and SFC are used to guide the parameter identification.

The transfer function forms are constructed in such a way: First. since the amplitude response of DFC reflects the gain characteristic of H_1 (from (3.7b)), it can be used to determine the transfer function form of H_1. Although the magnitude modulator H_{2A} in the H_2 stage will modify the amplitude of DFC observed from the system, such effect may merely change the DFC value rather than response curve shape.

Second, the amplitude ratio of SFC and DFC, reflecting the gain characteristic of H_{2L}. can be used to determine the transfer function of H_{2L}.

Third, considering when H_1 is a minimum phase function, it only offers a rather flat phase response in the DFC; the phase response of DFC in the VEP (which is not a flat curve) mainly results from the inhibitory process through inhibitory path LG and phase modulator H_{2P}. Since the phase of DFC produced from H_{2P} increases with inhibitory signal I_{LG}, thus, the DFC phase response curve shape, in some extent, reflects the gain characteristic of H_3 in path LG. This feature can be used to set the transfer function form of H_3.

We determine the transfer function forms of H_1, H_{2L} and H_3 in terms of the above discussion with consideration in minimum phase function category (except for a constant delay). After several tries for fitting the DFC and SFC data measured

from subjects A and B, we established the transfer functions for each linearity as follows:

$$H_1: \quad H_1(s) = \frac{(s+b_0)k_0}{s+a_0}\left(\frac{1}{s^2+a_1s+a_2}\right)^2\left(\frac{1}{s^2+a_3s+a_4}\right)^2 \exp^{-sT} \tag{5.24}$$

$$H_{2L}: \quad H_{2L}(s) = \frac{(s+b_1)k_1}{s+a_5}\frac{1}{s^2+a_6s+a_7}\frac{1}{s^2+a_8s+a_9} \tag{5.25}$$

$$H_3: \quad H_3(s) = \frac{k_2s^2}{(s^2+a_{10}s+a_{11})^2} \tag{5.26}$$

In H_1, a constant delay $\exp^{-sT}$ is added to the transfer function to express the time cost for transmitting the neural signal from the retina to the cortex. All the input-output relations of the blocks in model, so far, are completed, which are listed in Table 3.

Since there are eighteen parameters included in the model to be determined, the procedure of residual minimization may not necessarily yield unique parameter set or may not even converge. To avoid this situation, pre-adjustment of the initial parameters has to be made. A parameter identification procedure was developed in this work, its flowchart is shown in Figure 5.8.

The parameter estimation is done in two stages, namely pre-adjustment and parameter identification. During the pre-adjustment stage, individual elements are considered separately, while during the identification stage, all parameters are adjusted simultaneously. In each of the step, least-square sitting is used.

First, after each parameter has been assigned an initial value, the parameters in H_{2L} are determined independently to fit the SFC/DFC amplitude ratios according to (5.23).

Second, the parameters in H_1, except the constant delay T, are temporarily determined by DFC amplitude curve fitting according to (5.19). When H_1 has been settled, the parameters of H_3 are estimated by DFC phase curve fitting according to (5.20). After this has been done, the inhibitory modulation on the DFC amplitude has been changed due to the parameter change in H_3, the DFC amplitude response

from the model may not fit the data. If so, we repeat adjustment of the parameters of H_1 according to (5.19). Similarly, this change in H_1 parameters modifies the phase modulation of the DFC through H_3, so that the model fit for the phase response of the DFC may not hold. We again adjust parameters in H_3 in terms of (5.20). After alternatively repeating these two steps several times, both amplitude and phase responses of DFC from the model will be close to the observed VEP data. At this stage, the parameters of H_1 and H_3 are adjusted simultaneously according to (5.19) and (5.20).

Third, the conduction delay T is estimated by fitting the phase response of the SFC in accordance with (5.22).

Finally, the parameter identification is carried out, whereby all eighteen parameters are adjusted simultaneously by fitting both DFC and SFC responses in terms of (5.19), (5.20), (5.22) and (5.23).

When the system identification is guided by both amplitude and phase of VEP intermodulation components, the total least-square residuals to be minimized is a combination of amplitude residuals and phase residuals. However, because the phase values are much greater than the amplitude values, the total residuals are more sensitive to the phase variance than to the amplitude variance. Therefore, a different weight must be assigned to each residual set in order to balance the sensitivity of the amplitude variance and the phase angle variance.

The total least-square residual then is given by

$$R_n(\theta) = W_A \sum_{i=1}^{n} W_i[\overline{Y}_{iA} - \xi_A(\eta_i, \theta)]^2 + W_\phi \sum_{i=1}^{n} W_i[\overline{Y}_{i\phi} - \xi_\phi(\eta_i, \theta)]^2 \qquad (5.27)$$

where W_i are the weights obtained by (5.12) in terms of signal to noise ratio; W_A and W_ϕ are the constant weights assigned to the amplitude residuals and phase residuals respectively. The weight ratio of W_A and W_ϕ was set to 1:0.0001 in this work.

A corresponding program for frequency response fit was written in this work and linked with a Simplex minimum-residual-searching algorithm (Caceci & Cacheris, 1984). By using this program, we identified the system parameters for subject A and

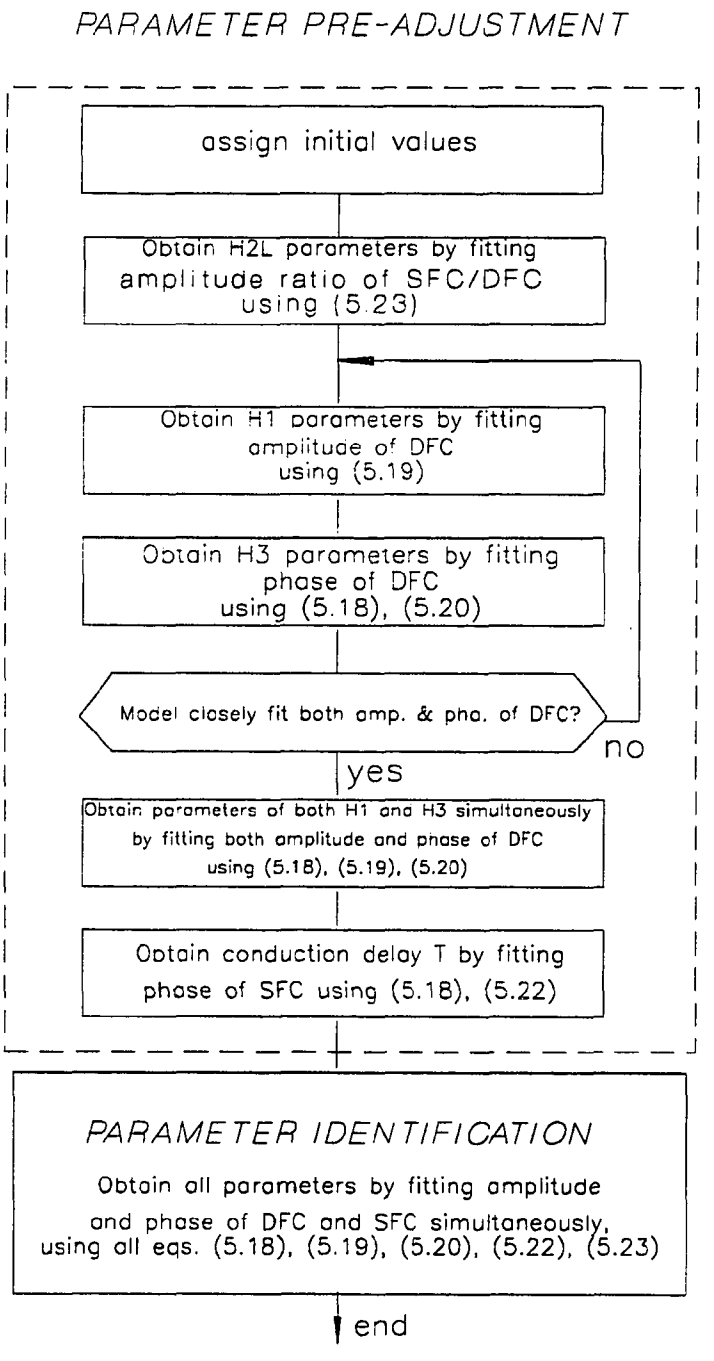

Figure 5.8 Frequency response curve fitting procedure.

subject B. The VEP data of both DFC and SFC measured from these two subjects and the model fits are displayed in Figure 5.9.1 and 5.9.2 respectively. In the figures, the data points are marked by symbols, while the fits are plotted in lines. The frequency characteristic of the initial linear filter H_1 in both model A and B are plotted in Figure 5.10, and the characteristic of H_3 are plotted in Figure 5.11. All the resulting parameters of models A and B are listed in Table 4. We expect these sets of data can offer useful information to set the initial values for further system identification.

We also mention : For the direct-through path in the model, the signal goes through H_1, H_{2A} and H_{2L}. The overall constant gain of the direct-through path is the product $k_0 p_3 k_1$. For the inhibitory path. the signal goes through H_1 and H_3. The overall constant gain of the inhibitory path is the product $k_0 k_2$. Those products can be treated as new parameters instead of k_0. p_3, k_1 and k_2. The number of model parameters can then be reduced.

5.4 Model Validation

When the model has been set, it remains to test whether this model is valid for its purpose. It involves the assessment how the model relates to observed data and its intended use. In this section, model validation is performed for the two subjects A and B. We will discuss i) whether the model is "good enough" to fit the VEP sum and difference frequency components, and ii) whether the model can predict the VEP response corresponding to the stimulus other than two-sinusoids.

5.4.1 Goodness of Fit

The model's goodness of fit is examined by the method of "lack of fit" (e.g. Davis & Goldsmith, 1972). This method is utilized for repeated sampling data and assumes that the errors or residuals are normally distributed. The principle is briefly described below, more details can be found in the reference.

Suppose that there are n frequency points, and at each point, there are m repeated measurements, then the total number of measurements is mn. We denote

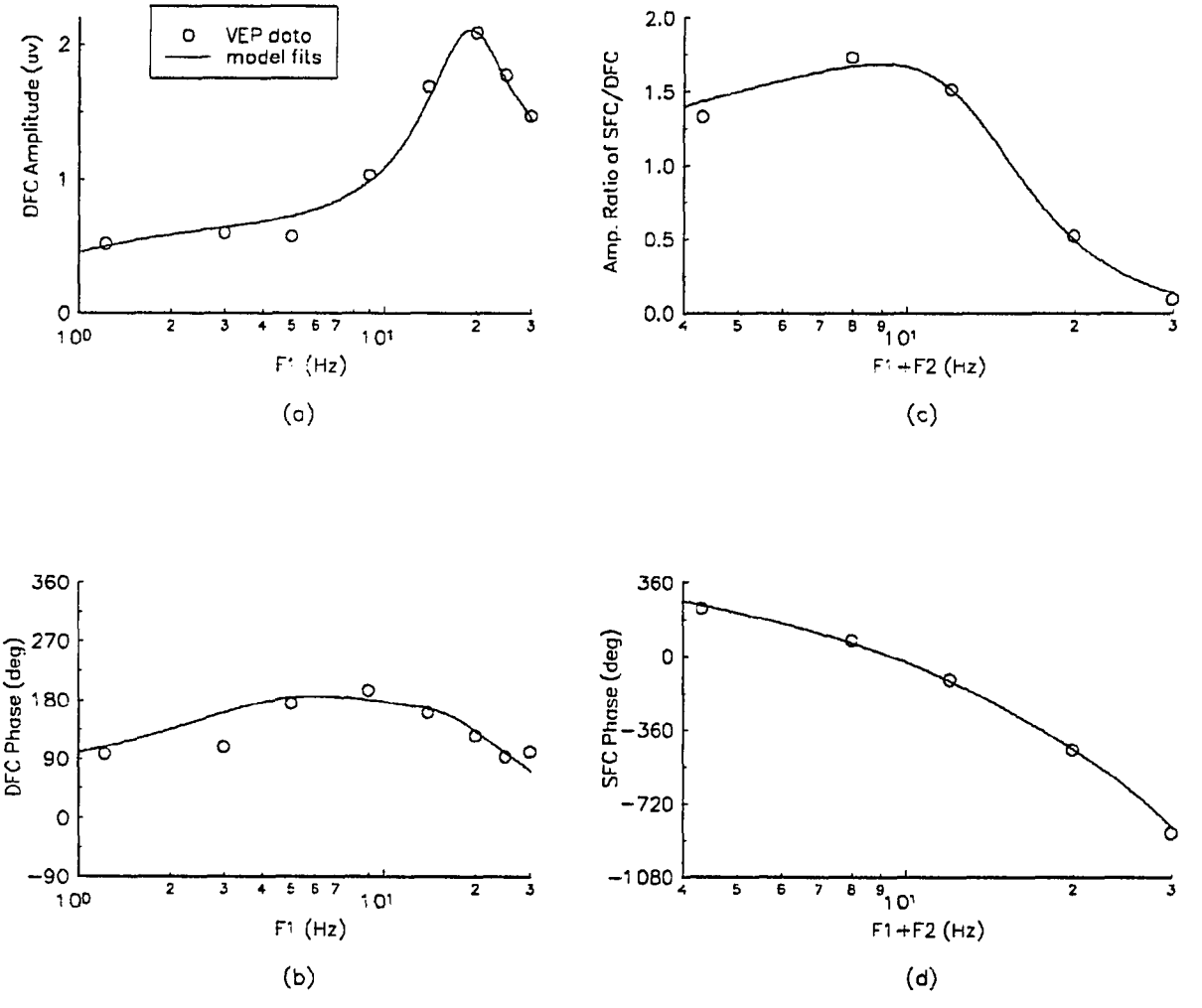

Figure 5.9.1 Intermodulation components of VEP from subject A and their fits from model A. The averaged observations are marked by the circular symbols The fits are plotted in smooth curves. a: amplitude responses of difference frequency component; b: phase responses of difference frequency component; c: ratios of sum and difference frequency component; d: phase responses of sum frequency component.

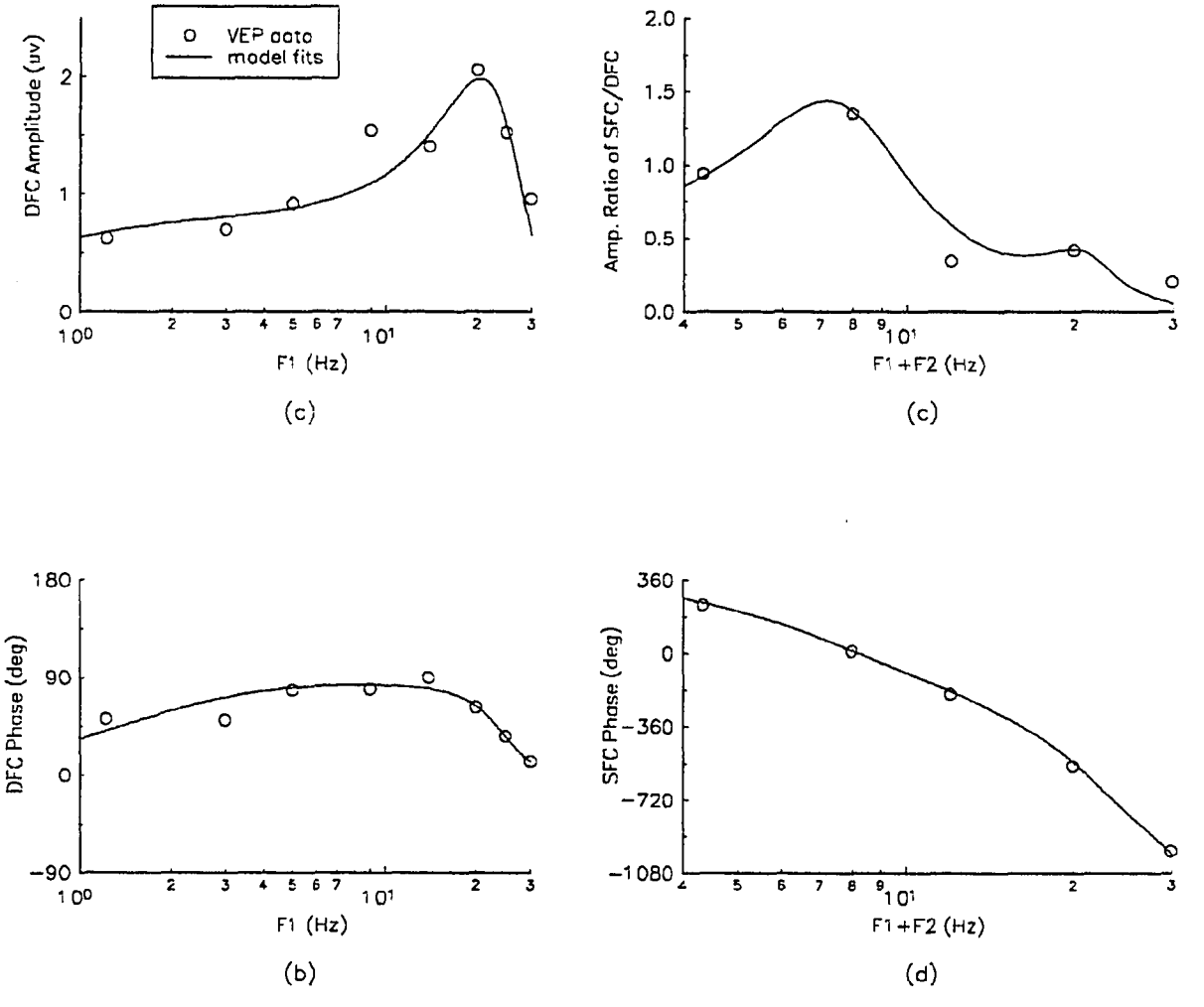

Figure 5.9.2 Intermodulation components of VEP from subject B and their fits from model B. The averaged observations are marked by the circular symbols. The fits are plotted in smooth curves. a: amplitude responses of difference frequency component; b: phase responses of difference frequency component; c: ratios of sum and difference frequency component; d: phase responses of sum frequency component.

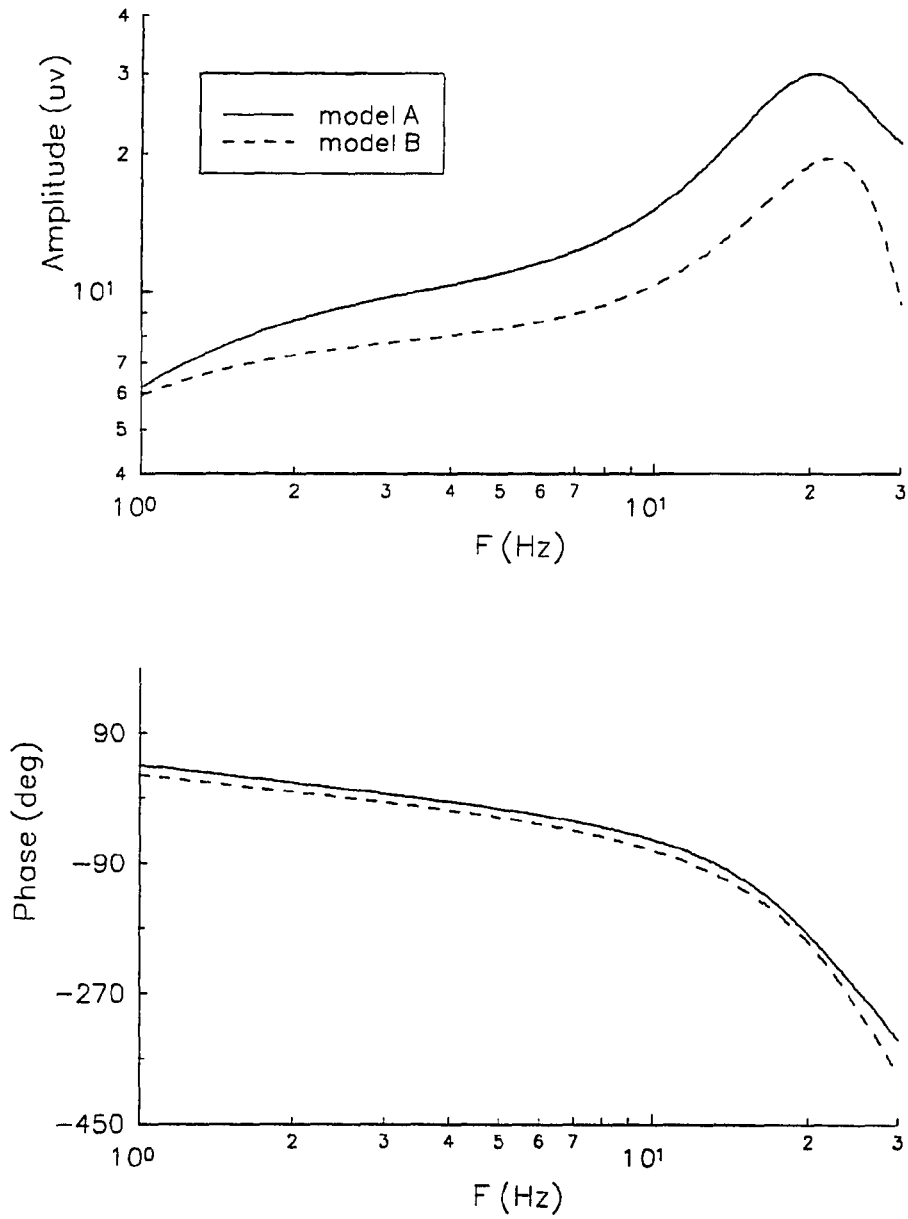

Figure 5.10 Frequency characteristic of initial linear filter H_1. Upper: amplitude; lower: phase. Model A's characteristic are plotted in solid, while model B's are plotted in dash.

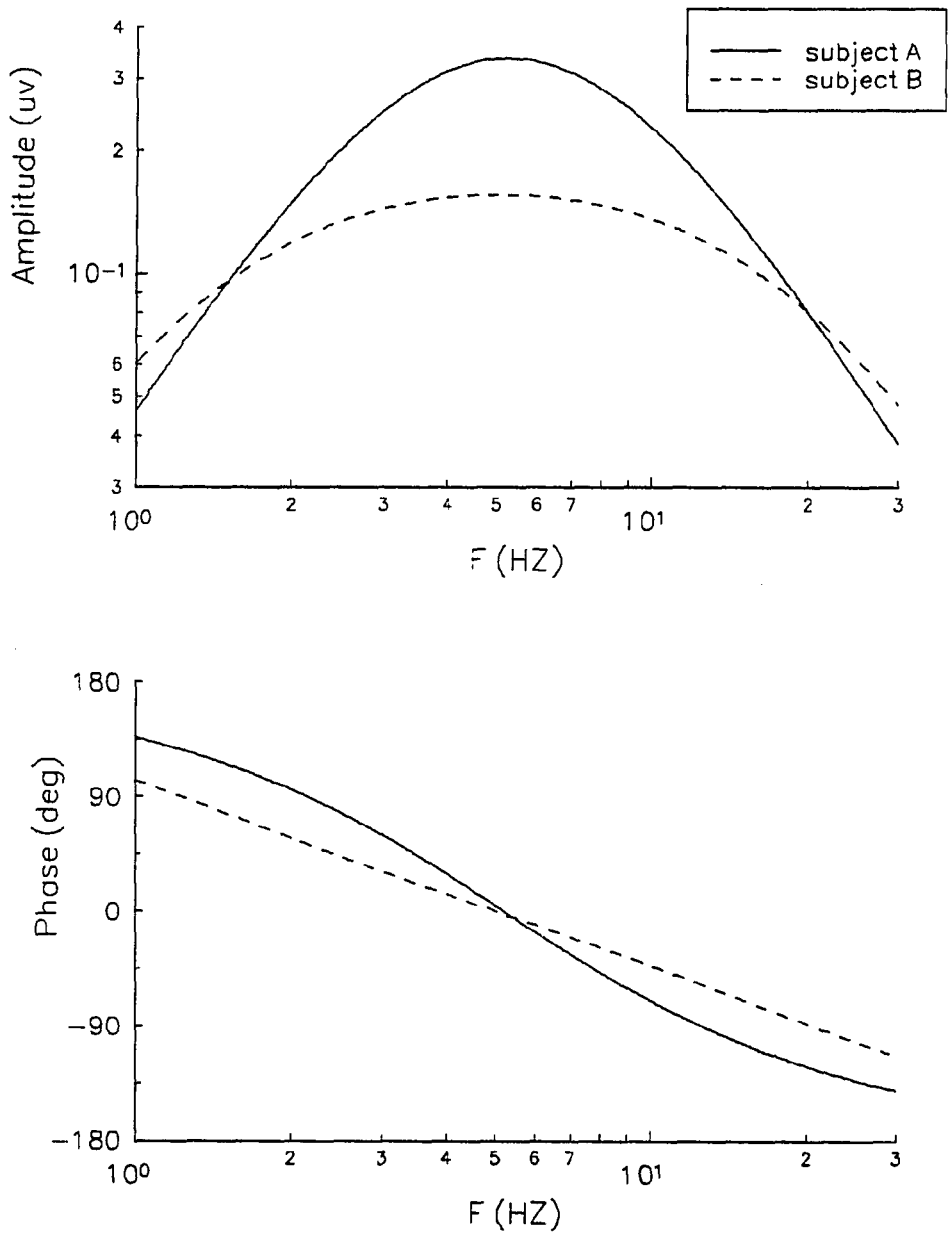

Figure 5.11 Frequency characteristic of H_3 in the inhibitory path. Upper: amplitude; lower: phase. Model A's characteristic are plotted in solid, while model B's are plotted in dash.

Table 4 Parameters of subject A and subject B resulted from frequency response curve fitting.

	H_1							
	k_0	b_0	a_0	a_1	a_2	a_3	a_4	T
subject A	7.05×10^9	0.2614	8.1367	102.06	16721	77.076	49098	0.030
subject B	9.02×10^9	0.2306	5.4600	181.665	37236	154.05	28507	0.032

	H_{2L}						
	k_1	b_1	a_5	a_6	a_7	a_8	a_9
subject A	3.59×10^8	7.2950	331.50	114.65	1922.6	73.168	6777.3
subject B	3.30×10^7	0.7540	31.416	31.491	2218.7	40.200	18026

	H_3		
	k_2	a_{10}	a_{11}
subject A	1.5996	69.266	1057.9
subject B	2.2322	120.95	990.47

a Fourier component measured at the ith point as Y_{ij} $(1 \leq i \leq n,\ 1 \leq j \leq m)$: the averaged data over all m measurements at point i as $\overline{Y}_i$; the model response at point i as $\hat{Y}_i$, then the total mean squared error due to noise is

$$MS_{(noise)} = \sum_{i=1}^{n}\sum_{j=1}^{m}(Y_{ij} - \overline{Y}_i)^2/df_{(noise)} \tag{5.28}$$

The total mean squared error due to "lack of fit" is

$$MS_{(lof)} = \sum_{i=1}^{n} m(\hat{Y}_i - \overline{Y}_i)^2/df_{(lof)} \tag{5.29}$$

where $df_{(lof)}$ is the degrees of freedom for "lack of fit", $df_{(noise)}$ is the degrees of freedom for noise.

Now we construct a F-ratio function

$$F = \frac{MS_{(lof)}}{MS_{(noise)}} = \frac{\sum_{i=1}^{n} m(\hat{Y}_i - \overline{Y}_i)^2/df_{(lof)}}{\sum_{i=1}^{n}\sum_{j=1}^{m}(Y_{ij} - \overline{Y}_i)^2/df_{(noise)}} \tag{5.30}$$

which satisfies condition of the F distribution. The criterion of judgement is statistically based. We give a null hypothesis that the total variance between the model responses and the true responses for all sampling points is not greater than the total variance of the measurements, and set a critical value F_{cri} so that there is a small probability that the F distribution value is greater than F_{cri}. If the calculation of (5.30) exceeds F_{cri}, the hypothesis is rejected, we say, there is a significant "lack of

fit", otherwise, we accept the hypothesis and say that the model has no significant "lack of fit". In such a case, problems with the model are attributed to noise.

In the system identification procedure, we fitted the VEP data expressed in amplitude and phase angle, the reason is that the data in such expression has more visible relation to the parameters in the model than the expression in real and imaginary part in s-plane, and thus more convenient for transfer function configuration and initial value setting. However, as described in Section 2.6, the amplitude and phase of VEP data do not satisfy the condition of normal distribution. Therefore, to examine the model goodness of fit, we calculate the model residuals and measurement residuals in terms of the component expressed in real and imaginary parts.

For difference frequency component, there are eight sampling points ($n = 8$) from 1.22 to 30 Hz. For sum frequency component, there are five sampling points ($n = 5$) from 4.33 to 30 Hz. At each point, there are four repeated records, and each record contains two measurements–real and imaginary components. So the total number of measurements is $(8+5) \times 4 \times 2 = 104$. The total mean squared error due to noise is

$$MS_{(noise)} = \sum_{i=1}^{13}\sum_{j=1}^{4}(Y_{ij(real)} - \overline{Y}_{i(real)})^2/df_{(noise)} + \sum_{i=1}^{13}\sum_{j=1}^{4}(Y_{ij(ima)} - \overline{Y}_{i(ima)})^2/df_{(noise)} \tag{5.31}$$

The total mean squared error due to "lack of fit" is

$$MS_{(lof)} = \sum_{i=1}^{13} 4(\hat{Y}_{i(real)} - \overline{Y}_{i(real)})^2/df_{(lof)} + \sum_{i=1}^{13} 4(\hat{Y}_{i(ima)} - \overline{Y}_{i(ima)})^2/df_{(lof)} \tag{5.32}$$

The footmarks 'real' and 'ima' in (5.31) and (5.32) express real part and imaginary part of the data respectively. Because there are eighteen parameters estimated, among which k_0 and k_1 can be combined into a new parameter k_0k_1, the degrees of freedom for residuals is

$$df_{(res)} = (8+5) \times 4 \times 2 - 17 = 87 \tag{5.33}$$

The degrees of freedom for noise is

$$df_{(noise)} = (8+5) \times (4-1) \times 2 = 78 \tag{5.34}$$

The degrees of freedom for "lack of fit" is

$$df_{(lof)} = df_{(res)} - df_{(noise)} = 87 - 78 = 9 \tag{5.35}$$

Because in the parameter estimation, weights was assigned to the residuals to be minimized (see equation (5.27)), the model has a tendency to more closely fit the data with higher weight than the data with lower weight. In checking the goodness of fit, the weights should also apply to the squared errors in (5.28) and (5.29). Therefore, the F ratio function becomes

$$F = \frac{\sum_{i=1}^{13}\sum_{j=1}^{4} W_i(Y_{ij(real)} - \overline{Y}_{i(real)})^2 + \sum_{i=1}^{13}\sum_{j=1}^{4} W_i(Y_{ij(ima)} - \overline{Y}_{i(ima)})^2}{\sum_{i=1}^{13} 4W_i(\hat{Y}_{i(real)} - \overline{Y}_{i(real)})^2 + \sum_{i=1}^{13} 4W_i(\hat{Y}_{i(ima)} - \overline{Y}_{i(ima)})^2} \cdot \frac{78}{9} \tag{5.36}$$

where W_i is the weight determined as the ratio of the amplitude and the radius of *error circle* of the component at ith point. Applying the data listed in Appendix B-II to (5.36), we have: for subject A, $F = 1.58$; for subject B, $F = 1.53$. From the table of F distribution, the critical value F_{cri} corresponding to 0.05 probability and (9.78) degrees of freedom is 1.99. Because both subjects F values are less than F_{cri}, we suggest that the model has no significant "lack of fit".

5.4.2 Model Prediction

Model prediction for the stimuli other than two-sinusoids is examined. The following two cases are considered of interest:

(1). Single-sinusoid stimulation (steady-state response).

(2). Step-function stimulation (transient response).

Single Sinusoid Stimulation

The stimulus for checking the model prediction, the same as the two-sinusoid one, was a contrast reversing dartboard pattern, but the luminance was temporally modulated with sinusoidal function

$$L(t) = L_m + L_m s(t) = L_m + L_m C_w \sin(2\pi f t) \tag{5.37a}$$

for one set of segments in the pattern, and

$$L(t) = L_m - L_m s(t) = L_m - L_m C_w \sin(2\pi f t) \tag{5.37b}$$

for the other set of segments. In (5.37), L_m is average luminance, $s(t) = C_w \sin(2\pi ft)$ is modulating signal, and C_w is modulation depth or contrast peak in percentage. To eliminate the effect caused by the contrast gain control in the retina, the modulating signal of the single sinusoid stimuli should match that of the two-sinusoid stimuli in RMS value. Therefore, the contrast peak C_w in equation (5.37), corresponding to 30% contrast of two-sinusoids, was set to 42.43%. Since the model contains a full-wave rectifier in the direct-through pathway, and only even harmonic components are produced from the system, second harmonic components from the model and in the VEP were compared. The frequency points in the experiment were set to 1.22, 2.87, 5.55, 7.29, 9.82, 12.15 and 14.96 Hz. Each test ran 32.08 seconds, and repeated four times at each frequency. Subjects A and B were tested monocularly with the same eye as the one tested with two-sinusoid stimulation. The second harmonic data are obtained by Fourier analysis on the recorded VEP. The vector-averaged data, as well as the radius of *error circle* are plotted versus frequency $2f$ in Figure 5.12.1 and 5.12.2.

To calculate the output from the model, we again use the 6th order polynomials to approximate the rectifier characteristic. For the single sinusoid input of (5.37), the second harmonics from the rectifier is (see Appendix C-I)

$$\text{amplitude:} \quad A_z(2f) = C_w|H_1(f)|(\tfrac{1}{2}a_2 + \tfrac{1}{2}a_4 + \tfrac{15}{32}a_6)$$
$$= 0.4307 C_w|H_1(f)|^* \tag{5.38}$$

$$\text{phase:} \quad \phi_z(2f) = 2\angle H_1(f) - \pi/2 \tag{5.39}$$

The inhibitory signal:

$$I_{LG} = C_w|H_1(f)||H_3(f)| \tag{5.40}$$

The second harmonics from the entire system is then

$$\text{amplitude:} \quad A_y(2f) = A_z(2f)\tfrac{p_3}{p_4+I_{LG}}|H_{2L}(2f)| \tag{5.40}$$

$$\text{phase:} \quad \phi_y(2f) = \phi_z(2f) + 4\pi - 8\arctan(\tfrac{4\pi f}{p_1+p_2 I_{LG}}) + \angle H_{2L}(2f) \tag{5.41}$$

*In equation (5.38), a_2, a_4 and a_6 are constant coefficients in the polynomials which are 2.307, -2.820 and 1.466 respectively.

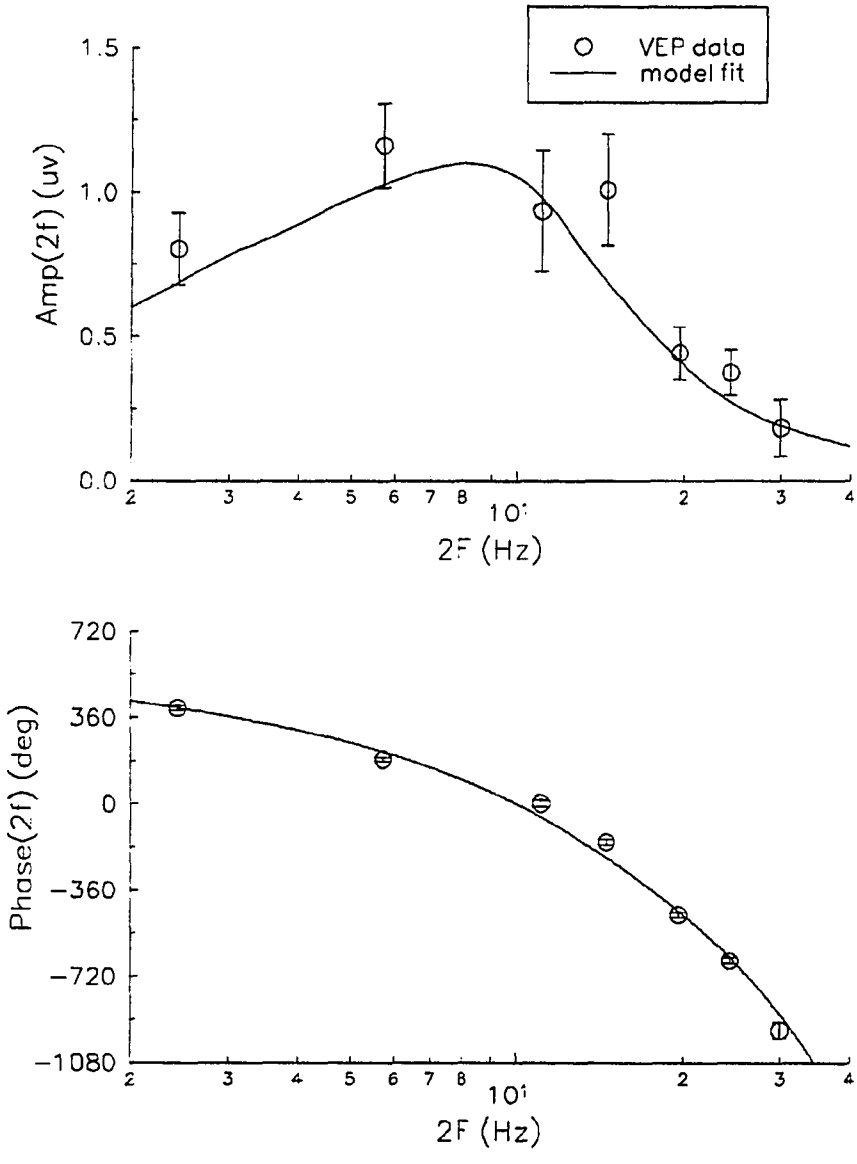

Figure 5.12.1 Comparison of single sinusoid stimulus responses from subject A and model A. Stimulus contrast was set to 42.43%. The stimulus frequencies were set to 1.22, 2.87, 5.55, 7.29, 9.82, 12.15 and 14.96 Hz. Second harmonics were selected for comparison. The vector-averaged data are marked by the circular symbols. Amplitudes are plotted with the radius of *error circles*, phases are plotted with their error range. The model responses are displayed in solid lines.

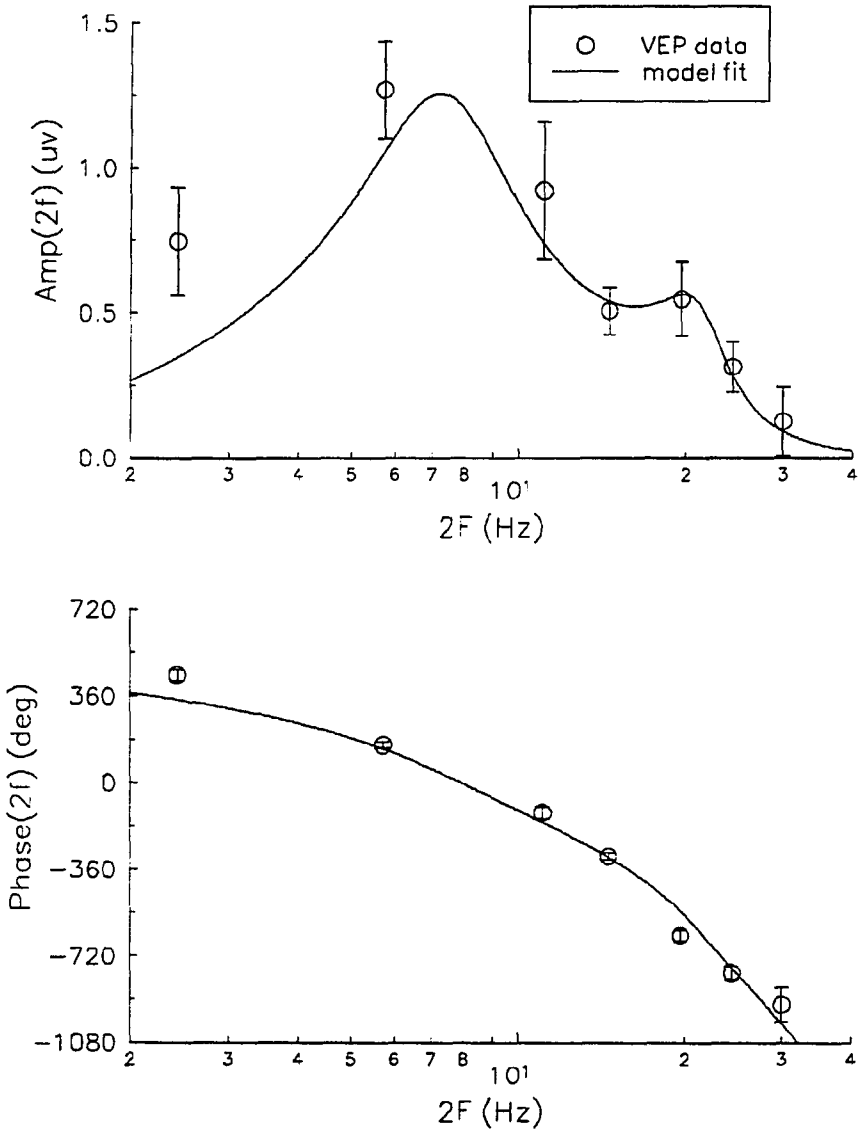

Figure 5.12.2 Comparison of single sinusoid stimulus responses from subject B and model B. Stimulus contrast was set to 42.43%. The stimulus frequencies were set to 1.22, 2.87, 5.55, 7.29, 9.82, 12.15 and 14.96 Hz. Second harmonics were selected for comparison. The vector-averaged data are marked by the circular symbols. Amplitudes are plotted with the radius of *error circles*, phases are plotted with their error range. The model responses are displayed in solid lines.

The model responses, calculated from the above equations for comparison, are plotted in solid lines in Figure 5.12.1 and 5.12.2.

The results are discussed as follows:

1. Amplitude responses of both subjects have a peak around 8 Hz and a rapid decrease beyond 15 Hz.

2. There are some quantitative differences between the two subjects' responses: subject B presents a sharp peak. while subject A has a relatively flat peak: subject B has an another small peak around 20 Hz, subject A does not. The differences may result from the cortical transfer characteristic because i) the same differences can be observed from the ratios of sum and difference frequency components (SFC/DFC) measured from subjects A and B due to the two-sinusoid stimulation (Figure 3.5.1.c and 3.5.2.c), and these ratios reflect the gain characteristic of H_2, which represents the cortical transfer characteristic (Section 2.1); ii) the second harmonic response due to the single sinusoid stimulation depends on the transfer characteristic of H_2 in the region below 30 Hz and that of H_1 in the region below 15 Hz; the latter has a rather flat gain below 15 Hz. (Figure 3.5.1.a and 3.5.2.a). Therefore, the VEP amplitude characteristic of the second harmonic as shown in Figure 5.12, reflects the gain characteristic of H_2 or the cortical transfer function.

3. The model response curves of Figure 5.12 essentially matches the VEP's for both subjects A and B.

Step Function Stimulation

To test the model prediction in time domain, a step function or a square-wave stimulus is usually considered. However, the transient behavior of the model which was developed for steady-state operation can not match that of the visual system. To facilitate the representation of the inhibitory process, block M (Figure 5.5.a) was constructed in the inhibitory path. This block converts the inhibitory signal $q(t)$ to

its RMS value I_{LG} which acts as a parameter in elements H_{2P} and H_{2A} for steady-state operation. The lowpass filter in block M (Figure 5.5.b) must possess a corner frequency below the lowest frequency of the signal processed in the inhibitory path. This means the corner frequency must be lower than 2 Hz. However, a typical transient VEP, which subsides within 500 ms (see Section 6.2), has a spectrum containing frequencies considerably greater than 2 Hz.

Therefore, in order to describe the visual system transient behavior, the parameters in H_2 must be controlled by a dynamic signal rather than a steady-state constant. A direct method to solve this problem is to modify the model in such a way that all the linear elements in the model retain the same functions, but the description of parameter control in H_2 for the steady-state operation is substituted by a dynamic description. For such limited range modification, the resultant questions are: i). can the dynamic model fit the VEP transient response? and ii) are the steady-state responses of the dynamic model reasonably consistent with those of the frequency response model?

Indeed, in the frequency response test, the input only contains one or two frequency components, but in the transient response test, the step function input contains the components covering a wide frequency range. Because a neuronal mechanism that responses to one particular stimulus may not response to another type of stimulus, or may not have an equivalent function to both stimuli, it is difficult to ensure that a model, which can fit the VEP frequency response, is able to fit the VEP transient response and vice versa. However, sinusoid and step function are the two important types of inputs for system modeling, both stimuli may reveal the characteristics of the response not apparent in the opposite stimulus response. We, therefore, readily take them into account for model assessment. This issue will be discussed in the next chapter.

CHAPTER 6
VEP DYNAMIC MODEL

In the frequency response model discussed in Chapter 5, the RMS value of the inhibitory signal $q(t)$, I_{LG}, is a constant acting as a parameter in elements H_{2P} and H_{2A}. However, to match the transient behavior of visual system, the dynamics of the inhibitory signal has to be considered. In this chapter, we modify the inhibitory process of the model, which includes block M in the inhibitory path LG (Figure 5.5), phase modulator H_{2p} and magnitude modulator H_{2A}, to make the system applicable for time domain operation. We also discuss the VEP transient response, including response recovering time and wave forms. A selective transient response to guide the parameter estimation is derived. System identification and model prediction are presented later in this chapter.

6.1 Dynamic Model Construction

As discussed in Chapter 5, block M (Figure 5.5) in the inhibitory path extracts the RMS value of inhibitory signal $q(t)$ to generate a constant signal I_{LG}. The lowpass filter in M should possess a sufficiently low corner frequency to eliminate all the harmonic and intermodulation components. Convenient as this may be for frequency response considerations. Such mechanism may not necessarily represent physiological function. In reality, the inhibitory parametric control may be much faster than that provided by the element M of Figure 5.5. This is an apparent reason that the frequency response model fails to predict the VEP transient response. To recover this deficiency, it is reasonable to either increase the corner frequency of the lowpass filter in M or even removed from the model. The inhibitory signal will then become a time varying signal, that is, we replace the notation I_{LG} by $i_{LG}(t)$. In the steady-state operation, from time average point of view, one can still expect, in some degree, that $i_{LG}(t)$ modulates the transfer character of H_{2A} and H_{2P} in a similar way as DC signal I_{LG} does.

We construct the dynamic model by keeping all the linear elements and the full-wave rectification constructed in the frequency response model unchanged, but remove the lowpass filter from element M in Figure 5.5, which gives the input-output relation of M:

$$i_{LG}(t) = \sqrt{q^2(t)} = |q(t)| \tag{6.1}$$

Thus, block M is simply a full-wave linear rectifier, $i_{LG}(t)$ is the absolute value of $q(t)$. A completed model structure for VEP temporal dynamics is illustrated in Figure 6.1. In the model, a time delay block ϵ^{-sT_c} is added so that the magnitude modulator H_{2A}, receiving $i_{LG}(t)$ via the delay block, can timely cooperate with phase modulator H_{2P} to generate a proper transient response. The input-output relations for all the elements in the model are listed in Table 5.

The VEP dynamic model of Figure 6.1 is essentially the same as the frequency response model of Figure 5.6 except for the inhibitory mechanism controlling elements h_{2A} and h_{2P}. This involves five new parameters, namely p_1, p_2, p_3, p_4 and T_c.

It is assumed that all the parameters in the linear elements will essentially be the same as those for frequency response modeling and identified as described in Chapter 5. One exception is the direct-through conduction delay T in element H_1.

Thus, in the VEP dynamic model, there are six parameters, p_1, p_2, p_3, p_4, T_c and T are to be identified. The parameter estimation is guided by the VEP transient response. The model will then go back to the frequency domain for examination of its performance.

6.2 VEP Transient Response

The transient response considered here is the step function response. The VEP is a weak signal merged in noise. To obtain a clear and correct response, we must average several responses corrected under the same test condition to increase the signal to noise ratio. A repetition of step functions is conveniently obtained by square-wave stimulation. If the square-wave frequency is set sufficiently low so that the VEP

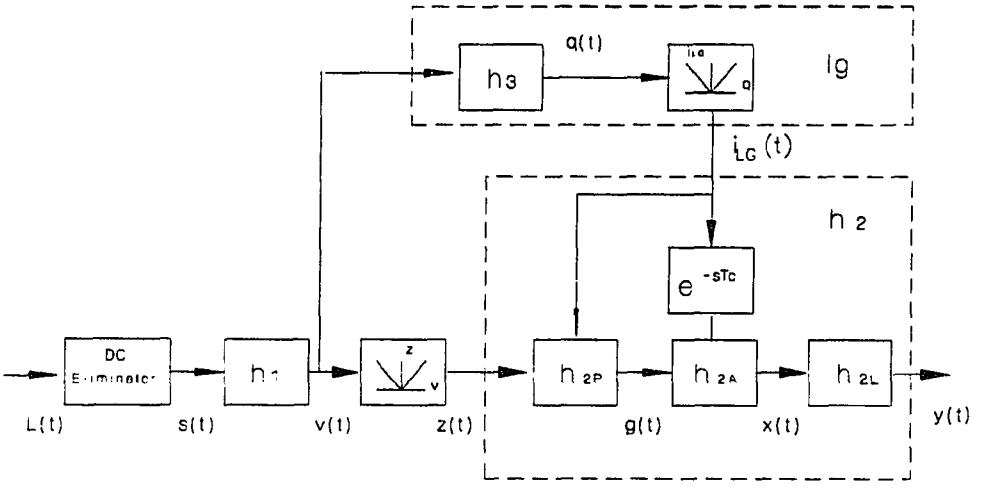

Figure 6.1 The VEP dynamic model. Components of the blocks are presented in Table 5.

Table 5 Characteristics of each element in the dynamic model

$$h_1: \quad v(t) = \int_0^t \mathrm{L}^{-1}\left[\frac{(s+b_0)k_0}{s+a_0}\left(\frac{1}{s^2+a_1 s+a_2}\right)^2\left(\frac{1}{s^2+a_3 s+a_4}\right)^2 e^{-sT}\right] s(t-\tau)d\tau$$

$$N: \quad z(t) = N[v(t)] = |v(t)|$$

$$h_{2P}: \quad \begin{bmatrix} \dot{x}_1 \\ \dot{x}_2 \\ \dot{x}_3 \\ \dot{x}_4 \end{bmatrix} = \begin{bmatrix} -\eta(t) & 0 & 0 & 0 \\ -2\eta(t) & -\eta(t) & 0 & 0 \\ -2\eta(t) & -2\eta(t) & -\eta(t) & 0 \\ -2\eta(t) & -2\eta(t) & -2\eta(t) & -\eta(t) \end{bmatrix} \begin{bmatrix} x_1 \\ x_2 \\ x_3 \\ x_4 \end{bmatrix} + \begin{bmatrix} 2\eta(t) \\ 2\eta(t) \\ 2\eta(t) \\ 2\eta(t) \end{bmatrix} z(t)$$

$$g(t) = \begin{bmatrix} -1 & -1 & -1 & -1 \end{bmatrix} \begin{bmatrix} x_1 & x_2 & x_3 & x_4 \end{bmatrix}^T + \begin{bmatrix} 1 \end{bmatrix} z(t)$$

$$\eta(t) = p_1 + p_2 i_{LG}(t)$$

$$h_{2A}: \quad x(t) = \frac{p_3}{p_4 + i_{LG}(t-T_c)} g(t)$$

$$M: \quad i_{LG}(t) = M[q(t)] = |q(t)|$$

$$h_{2L}: \quad y(t) = \int_0^t \mathrm{L}^{-1}\left[\frac{(s+b_1)k_1}{s+a_5}\frac{1}{s^2+a_6 s+a_7}\frac{1}{s^2+a_8 s+a_9}\right] x(t-\tau)d\tau$$

$$h_3: \quad q(t) = \int_0^t \mathrm{L}^{-1}\left[\frac{k_2 s^2}{(s^2+a_{10}s+a_{11})^2}\right] v(t-\tau)d\tau$$

response elicited by the step-changes of luminance returns to its initial state before next step-change occurs, the response can be effectively considered as a transient one.

The frequency of the square-wave function should be determined so that the half period of the function is longer than the VEP *recovering time*, defined as the time period that the VEP response returns to its initial state after each luminance step-change. Experiments showed (Figure 3.1) that the VEP due to a luminance step-change essentially subsides in 500 ms (see also Zemon, 1984 and Regan, 1989). Hence, a 1 Hz square-wave stimulus was used to obtain the VEP transient responses.

VEP transient responses were measured from both subjects A and B. The dart-board stimulus pattern was the same as the one used in the two-sinusoid stimulation test. The luminance on the pattern was temporally modulated by the function

$$s(t) = \begin{cases} C_w & nT < t \leq (n+1/2)T \\ -C_w & (n+1/2)T < t \leq (n+1)T \end{cases} \quad n = 0, 1, 2, \ldots \qquad (6.2a)$$

for one set of segments and

$$s(t) = \begin{cases} -C_w & nT < t \leq (n+1/2)T \\ C_w & (n+1/2)T < t \leq (n+1)T \end{cases} \quad n = 0, 1, 2, \ldots \qquad (6.2b)$$

for another set of segments. To maintain the equivalent effect of the contrast gain control in the retina, the modulation depth C_w of the square-wave function was set to 30%, equal to the RMS value of the modulation signal of the two-sinusoid stimuli (Appendix C-II). The test ran 32.08 seconds and was repeated four times on each subject. Since the response waveforms in each half period of 500 ms are considered identical to each other, due to the rectification process in the visual pathways, data recorded in each 500 ms period are averaged. The responses, filtered by a digital lowpass filter with a cut-off frequency of 40 Hz, are presented in Figure 6.2. The top row shows the four individual averaged responses. The middle rows shows the mean responses (solid line) and the error ranges (expected error of the mean, dashed line). The "expected error of the mean", $\varepsilon_y(t)$, represents the accuracy of the estimate of the VEP response $y(t)$*. the bottom shows the the stimulus function. The left column of the figure is for subject A, and the right column is for subject B.

*For each time sample t of the $m = 4$ responses, the "expected error of the mean", $\varepsilon_y(t)$, of the

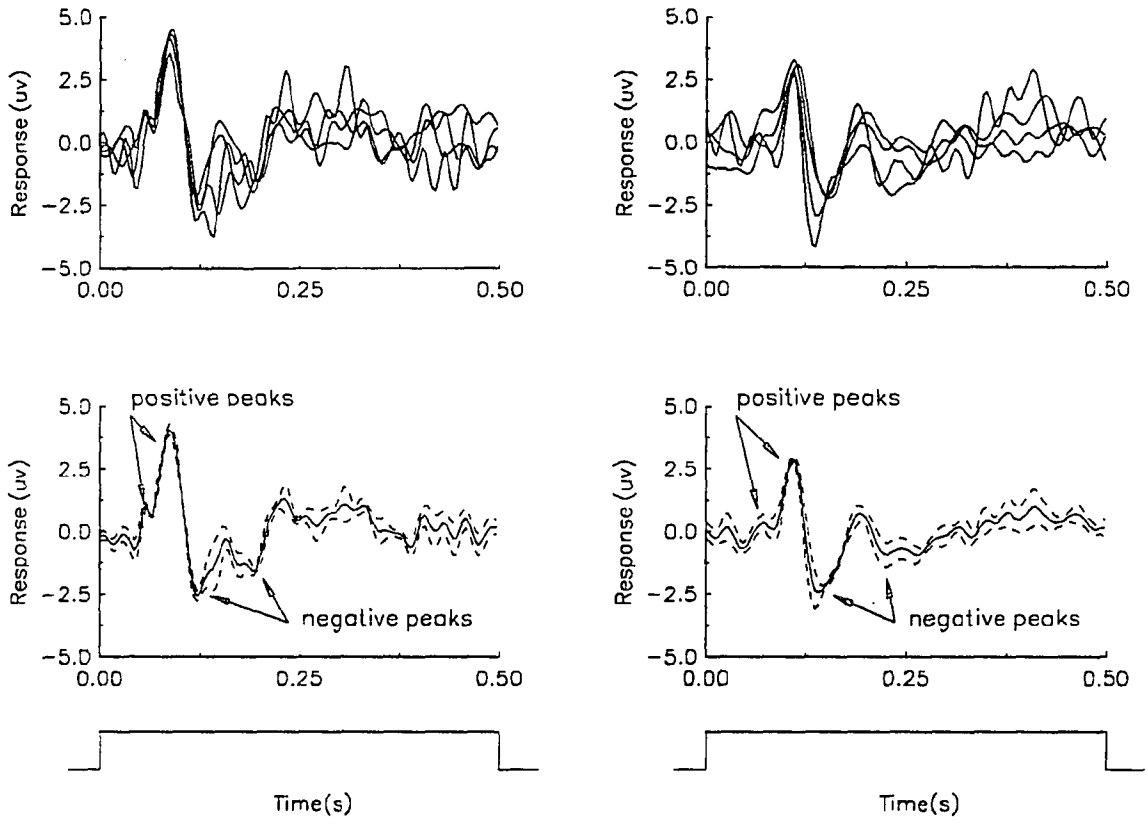

Figure 6.2 VEP transient responses measured from subject A (left column) and subject B (right column). The top plots present the four responses, each averaged over 64 records. The second row shows the mean responses (solid line) and the error ranges (expected error of the mean, dashed line). The bottom row shows the stimulus function.

It is seen in Figure 6.2 , the response shape can be predominantly characterized as two positive waves (the first one is much smaller than the second one) followed by two negative waves. These different waves can reflect different cellular events. Excitatory postsynaptic potentials depolarize apical dentrites' membranes near the cortical surface to generate a superficial sink and deep current source, resulting surface negative activity; Inhibitory postsynaptic potentials hyperpolarize the dentrites' membranes to generate a superficial current source and deep sink, resulting surface positive activity (Eccles, 1951; Purpura, 1959; Creutzfeldt & Kuhnt, 1973). The earlier two positive waves might reflect combined action potentials arriving at the cortex via two groups of LGN (lateral geniculate nucleus) afferent fibers which have different conduction velocities (Watanabe, Konishi & Creutzfeldt, 1966; Zemon, Kaplan & Ratliff, 1986). The initial positivity, occurring around 60 ms, is thought to be an initial depolarization occurring deep in the cortex, presumably in layer *IV* (Watanabe, Konoshi & Creutzfeldt, 1966; Cretzfeldt, Rosina, Ito & Probst, 1969; Creutzfeldt & Kuhnt, 1973). The second positive wave, occurring around 100 ms, is believed an inhibitory process, mediated by GABA–a presumed inhibitory transmitter, in the visual cortex (Krnjevic & Schwartz, 1967; Zemon, Kaplan & Ratliff, 1986). The two negative waves, occurring later, probably reflect the neuron excitatory activities in the cortex (Eccles, 1951; Purpura, 1959; Creutzfeldt & Kuhnt, 1973).

The relative "smoothness" of the average responses, shown in the center row of Figure 6.2 during $t < 100$ ms and $t > 300$ ms, suggests that the waves in the

four individual VEP averaged responses $\overline{y}_j(t)$ $(j = 1, 2, 3, 4)$ is defined as

$$\varepsilon_y(t) = \sqrt{\sum_{j=1}^{4} (\overline{y}_j(t) - \overline{y}(t))^2} \Big/ \sqrt{(4)(4-1)}$$

where $\overline{y}(t) = \frac{1}{4}\sum_{j=1}^{4} \overline{y}_j(t)$ is the mean value of $\overline{y}_j(t)$. The expected error of the mean, which represents the accuracy of the estimate of the VEP response $y(t)$, is related to the standard deviation of $y(t)$,

$$\sigma_y(t) = \sqrt{\sum_{j=1}^{4} (\overline{y}_j(t) - \overline{y}(t))^2} \Big/ \sqrt{4-1} = 2\varepsilon_y(t)$$

individual responses (top row) during those intervals represent (uncorrelated) noise.

6.3 Choice of Criterion for Fit

To obtain reliable data for parameter estimation, we prefer to reserve the relevant positive and negative waves discussed before, and disregard the earlier and later parts of the responses. we also expect the parameter estimation to be guided by the predominant waveforms, the initial positive wave, which is much smaller than the other three waves. is then neglected even though it is a portion of reliable response.

Similar to the identification of the frequency response model, least-square method is selected for the dynamic model identification, using the criterion function

$$R_N(\theta) = \sum_{i=1}^{N} W_i[\overline{y}(i\Delta T) - \xi(i\Delta T, \theta)]^2 \tag{6.3}$$

where θ is a vector of parameters to be determined, ΔT is a sampling interval, N is the number of sampling points in the period, $\overline{y}$ is the mean response and ξ is the model response, W_i is a window-like weighting function created for extracting the predominant positive wave and the two negative waves in the transient response. The window-like weighting function is defined for the sample at $i\Delta T$ as

$$W_i = \frac{1}{1 + 9\exp^{-k(i\Delta T - T_1)}} - \frac{1}{1 + 9\exp^{-k(i\Delta T - T_2)}} \tag{6.4}$$

The coefficients k, T_1 and T_2 were determined manually by visual inspection to cover the region of the predominant wave forms. Their values are listed in Figure 6.3, which presents plots of the weighting function W_i for both subjects A and B.

6.4 Parameter Estimation

The VEP averaged responses of subjects A and B, presented in Figure 6.2, are used for guiding the parameter estimation. The model transient response is derived by applying a step function input to the system and calculating its output with MATRIXx software (produced by Integrated System Inc., Santa Clara, CA). The minimum residuals-search routine for criterion function (6.3) is implemented by *Maximum-Likelihood* algorithm in the MATRIXx software.

	weighting func.		
	k	T_1	T_2
subject A	87.89	0.025	0.2
subject B	87.89	0.025	0.3

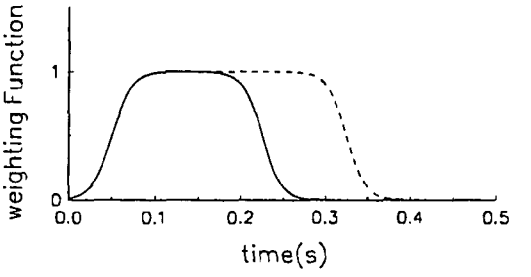

Figure 6.3 Window-like weighting function (6.4) used in the least-square curve fitting, which extracts the predominant wave forms in the VEP transient response. The solid curve is for subject A. and dashed curve is for subject B. Coefficients in (6.4) for both subjects are listed in the left of the figure.

The system identification procedure. as shown in Figure 6.4, is separated into several steps. First, we set the conduction delay T_c to zero, and assign some reasonable initial values to the coefficients p_1, p_2, p_3 and p_4. In this work, we set the initial values: $p_1 = 1.2$, $p_2 = 1.2$, $p_3 = 0.4$ and $p_4 = 1.2$. Generally, this initial assignment will enable the dynamic model to produce a transient response with one positive wave followed by two negative waves.

Second, by varying conduction delay T, the whole response curve can be shifted to the position that the positive wave peak in the model response matches the positive peak of the VEP response.

Third, we note that. for step function input, the signal $i_{LG}(t)$ produced in the lateral path possesses a sharp peak wave. If we change conduction delay T_c, the inhibitory signal $i_{LG}(t)$ will shift along the time axis, which allows us to inhibit the direct-through signal selectively. In our model, T_c is set to 0.013 s so that the first negative wave will be inhibited by the sharp peak of $i_{LG}(t)$.

The adjustment of both T and T_c above were done manually.

When conduction delays T and T_c have been set, only four remaining parameters should be determined. We note that p_3 represents an overall system gain which affects the magnitudes of all three peak waves; p_4 influence the level of magnitude inhibition. Since T_c has been selected to inhibit the first negative wave, the magnitude

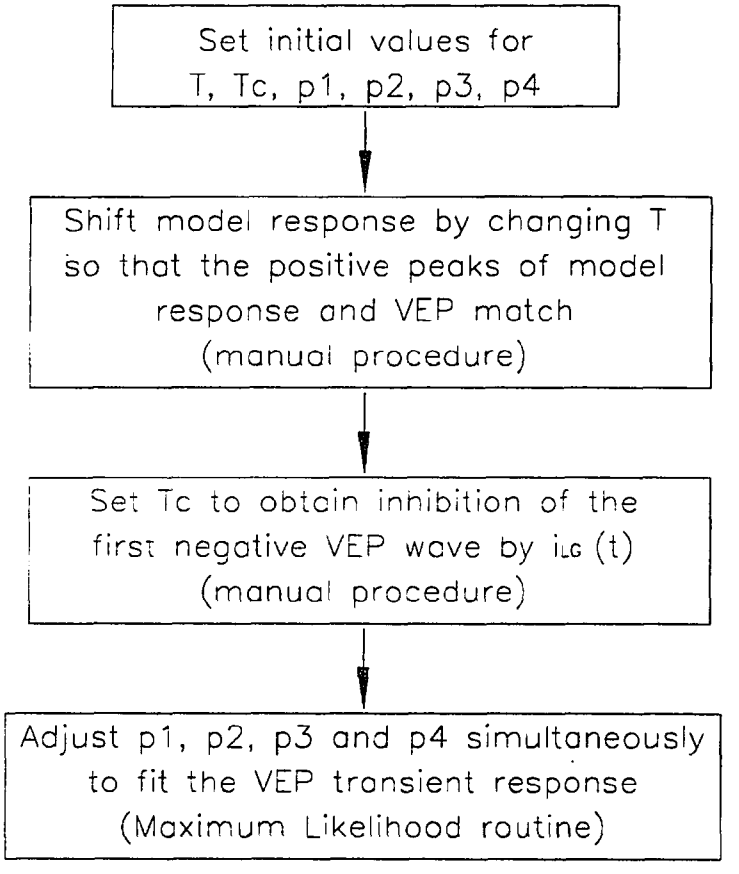

Figure 6.4 Transient response curve fitting procedure.

of the first negative wave can be controlled by adjusting coefficient p_4. Furthermore, by numerical calculation, we found that p_1, cooperating with p_2, can control the magnitude of the two negative waves. In this last step, all these four parameters are determined simultaneously by least-square curve fitting, carried out by Maximum-Likelihood routine in MATRIXx software.

Model parameters have been identified for both subjects A and B. The results are plotted in Figure 6.5. VEP averaged transient responses are plotted in solid curves, while the model responses are plotted in dashed curves. The resulting parameters and the coefficients of the weighting functions in criterion equation (6.3) are listed

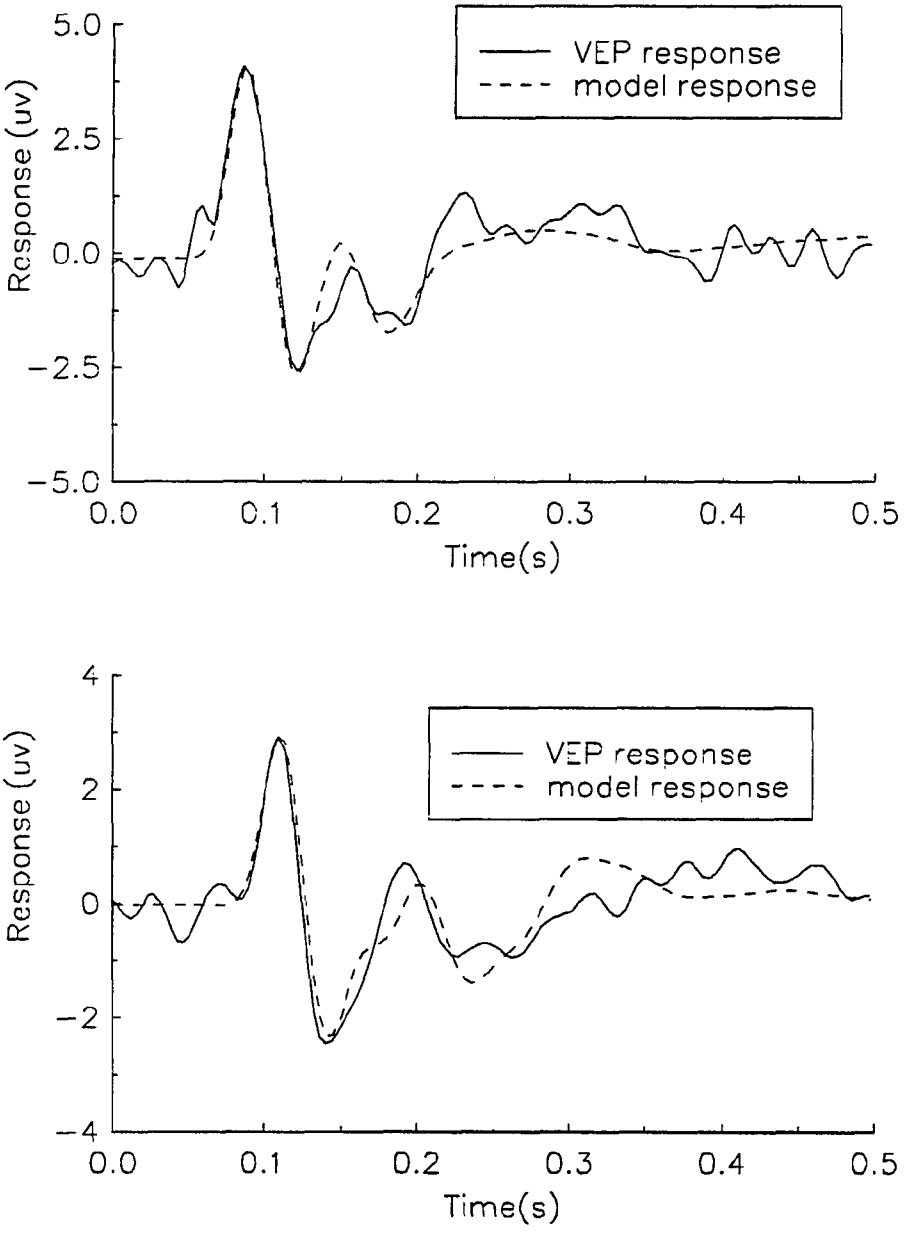

Figure 6.5 The transient responses measured from the cortex (solid) and produced by the model (dash). Top: responses for subject A. Bottom: responses for subject B.

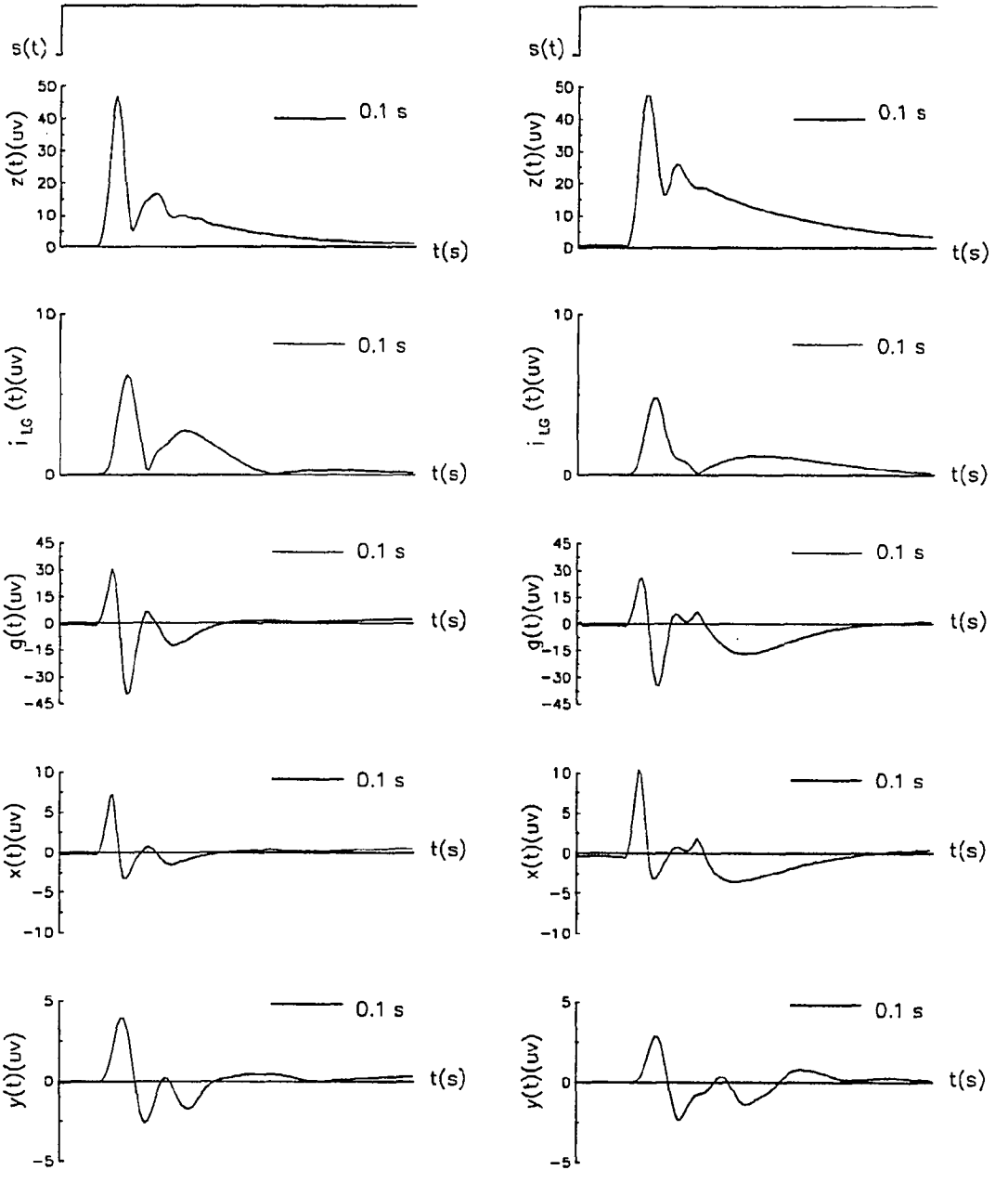

Figure 6.6 Input signal and corresponding responses produced from some blocks in the model. The left column is the plot for subject A, and the right column for subject B.

Table 6 Parameters of the dynamic model for subject A and subject B, resulting from curve fitting of VEP transient responses.

	model parameters					
	T	T_c	p_1	p_2	p_3	p_4
subject A	0.035	0.013	1.715	2.453	0.435	0.811
subject B	0.047	0.013	1.034	2.507	0.347	0.512

in Table 6. The input function, responses from some subsystems of the model, $z(t)$, $i_{LG}(t)$, $x(t)$ and $y(t)$, are drawn in Figure 6.6. It is seen from Figure 6.5 that the dynamic model appears to provide a reasonable fit of the predominant VEP wave forms for each of the two subjects.

6.5 Model Prediction

It now remains to be examined how well the dynamic model will perform in the steady-state for periodic stimuli. The prediction ability of the model for periodic stimulation has been examined for the two-sinusoid input. The sum and difference frequency components produced from the system were obtained by numerical calculation* and compared with the VEP responses measured from subjects A and B. The amplitude of two-sinusoid input for the model was set to 0.30. The input frequencies were set to f_1 =1.2, 1.8, 3.0, 3.8, 5.0, 6.8, 9.0, 11.8, 14.0, 16.8, 20.0, 22.0, 25.0, 28.0 and 30.0 Hz. The separation between the two frequencies in each pair was fixed at 2 Hz. The DFC and SFC responses produced from the dynamic model, together with the previous DFC and SFC responses from the frequency response model and the VEP data, are plotted in Figure 6.7.1–4. In those figures, amplitude response of DFC is plotted in (a), phase response of DFC in (b), amplitude response of SFC in (c) and phase response of SFC in (d). It is seen that the dynamic model responses (DFC and SFC) do not match the measured VEP data although the curve shapes of the model

*The responses of the model due to the two-sinusoid input are recorded for 10 seconds with 1000 sampling points. difference frequency components (DFC) and sum frequency components (SFC) are obtained by Fourier transform of the dynamic model response from simulation.

responses and the VEP's are consistent in the region above 5 Hz for DFC and above 8 Hz for SFC.

The above outcome limits the application of the dynamic model in the frequency category. However, if the model prediction is only considered for response curve rather than values in the high frequency region, the application of the dynamic model may extend to the frequency domain.

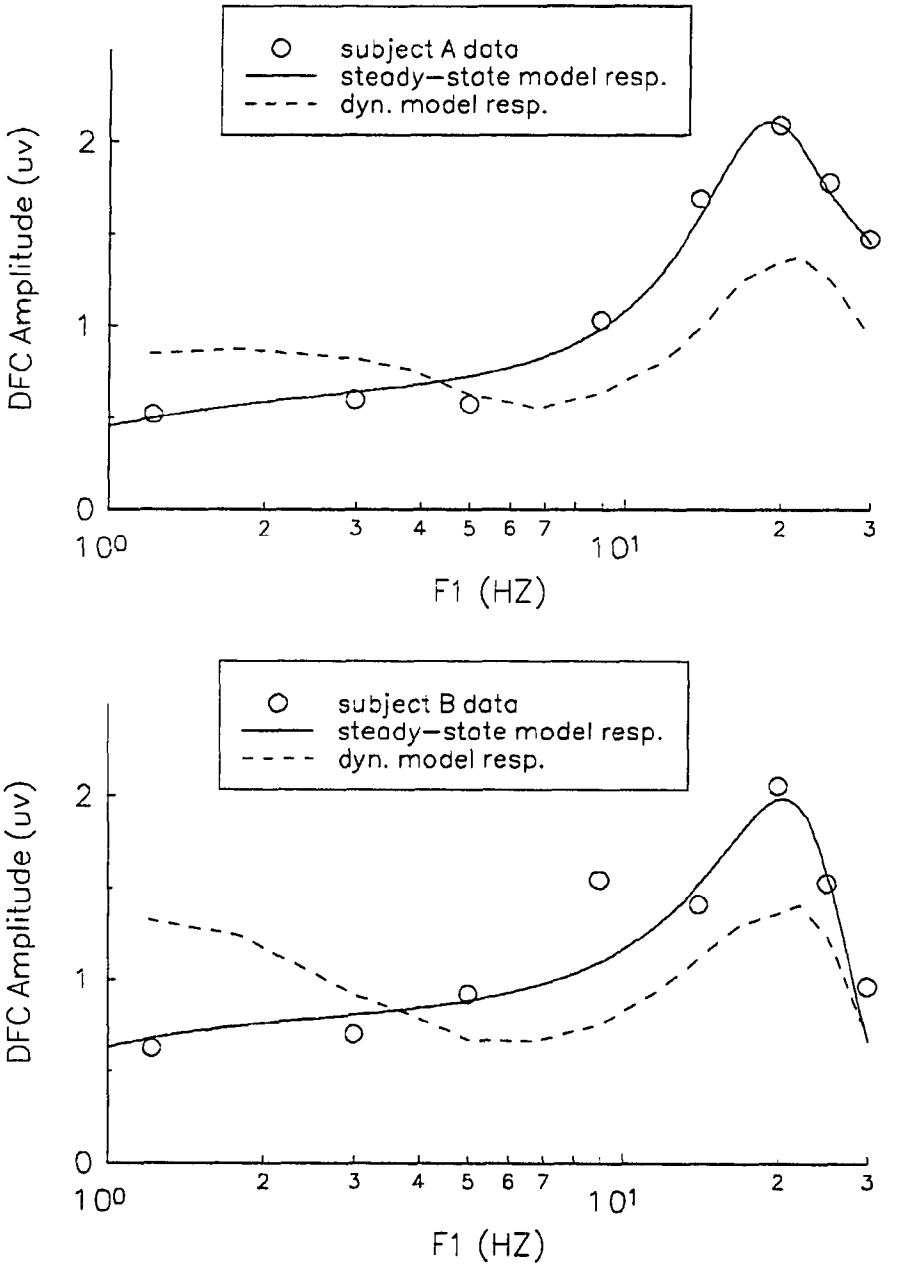

Figure 6.7.1 Amplitude responses of difference frequency component from the dynamic model, frequency response model and VEP. The upper graphic is for subject A, the bottom graphic is for subject B. The dynamic model response is derived by employing a two-sinusoid input to the system with amplitude 0.30 and frequency pair separation 2.0 Hz.

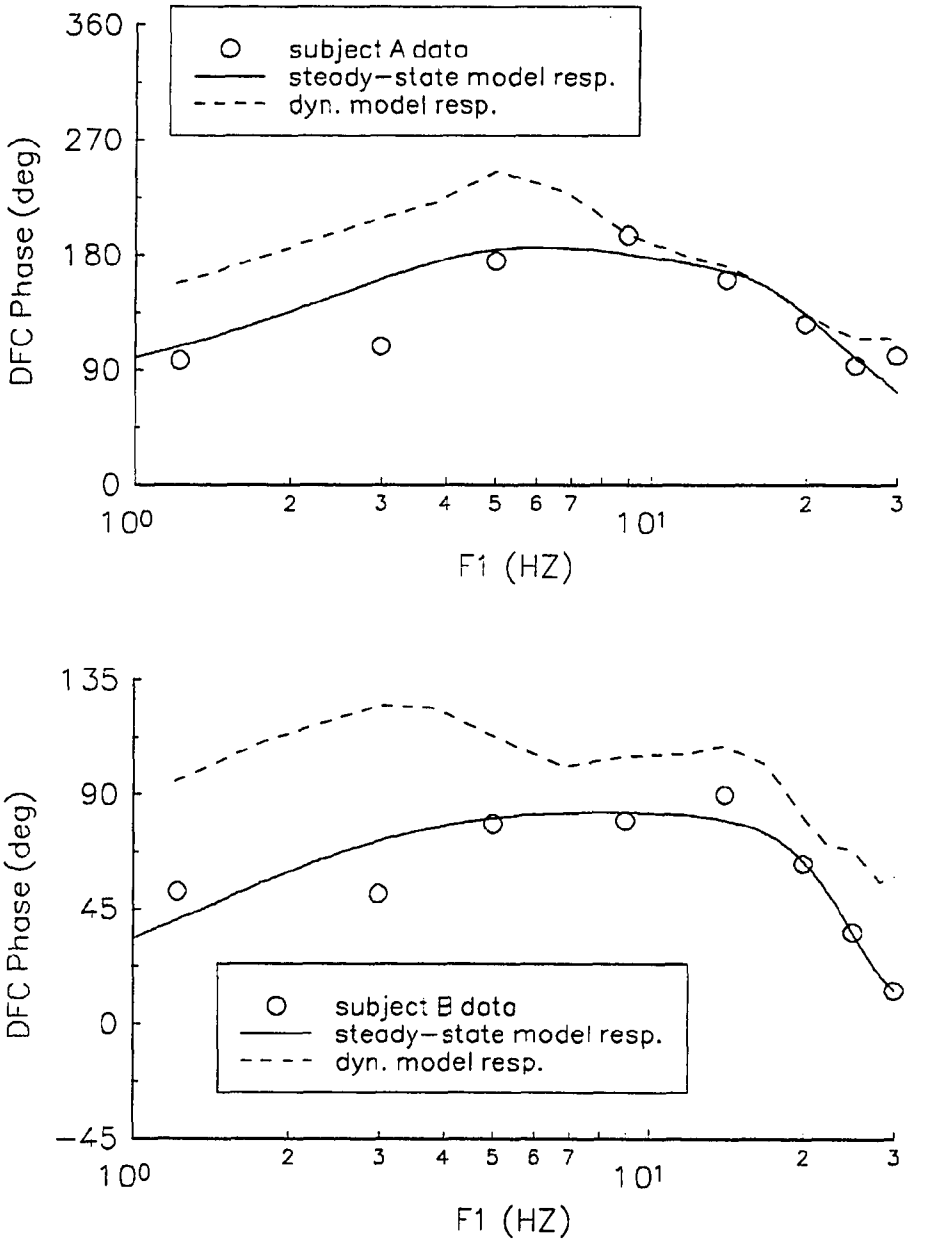

Figure 6.7.2 Phase responses of difference frequency component from the dynamic model, frequency response model and VEP. The upper graphic is for subject A, the bottom graphic is for subject B. The dynamic model response is derived by employing a two-sinusoid input to the system with amplitude 0.30 and frequency pair separation 2.0 Hz.

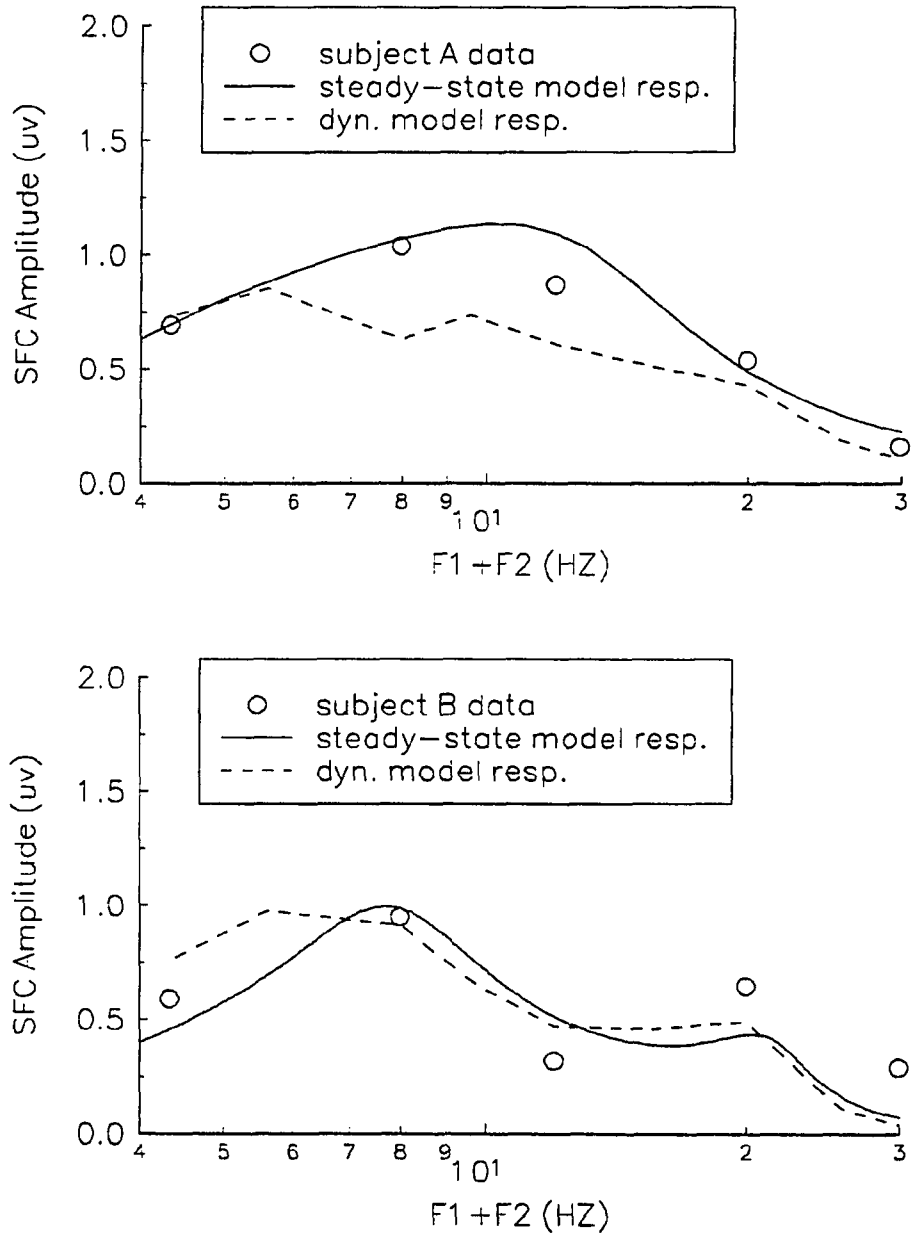

Figure 6.7.3 Amplitude responses of sum frequency component from the dynamic model, frequency response model and VEP. The upper graphic is for subject A, the bottom graphic is for subject B. The dynamic model response is derived by employing a two-sinusoid input to the system with amplitude 0.30 and frequency pair separation 2.0 Hz.

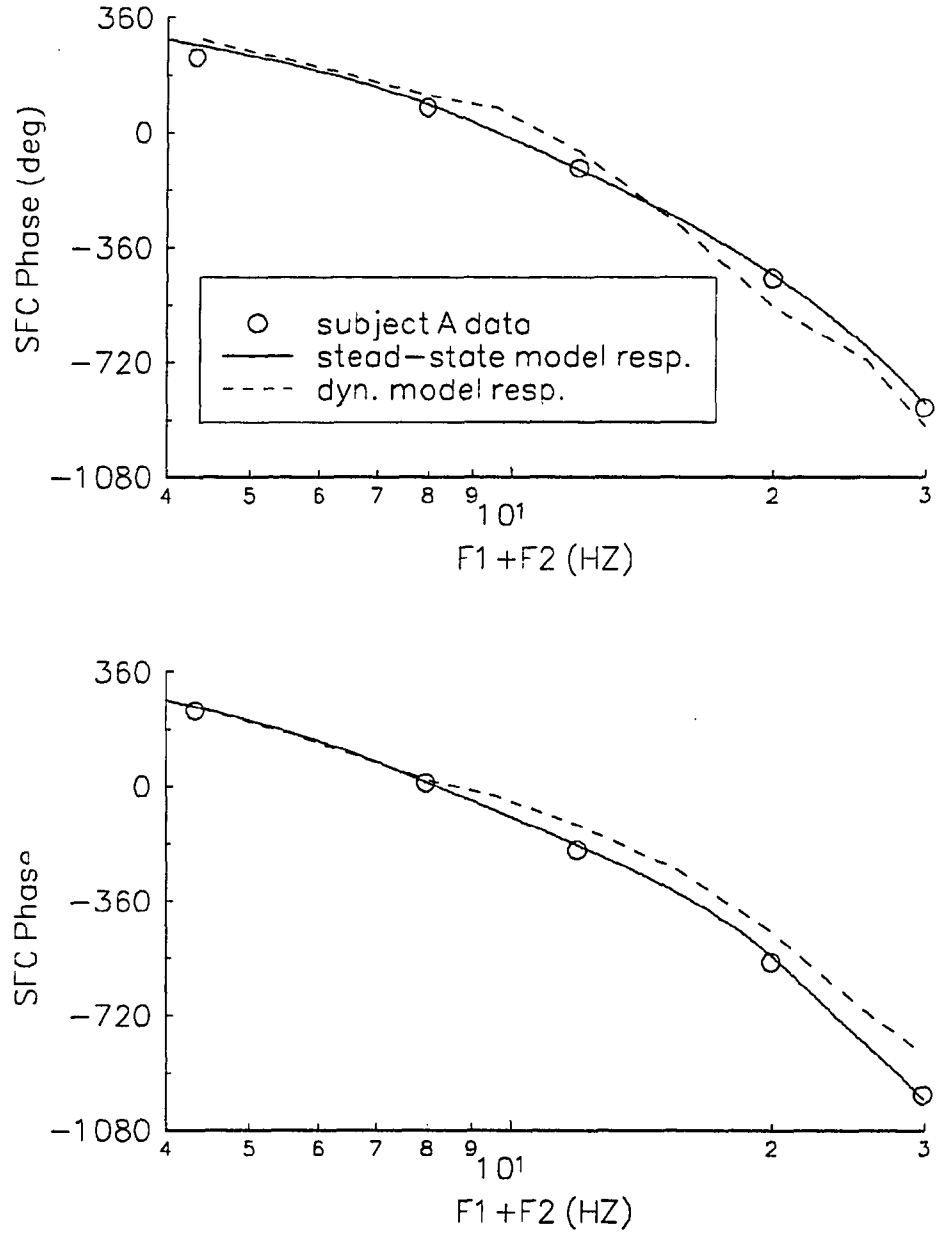

Figure 6.7.4 Phase responses of sum frequency component from the dynamic model, frequency response model and VEP. The upper graphic is for subject A, the bottom graphic is for subject B. The dynamic model response is derived by employing a two-sinusoid input to the system with amplitude 0.30 and frequency pair separation 2.0 Hz.

CHAPTER 7
DISCUSSION

7.1 Summary of the Results

1. Sandwich modeling for the VEP frequency response was performed, and the resulting fit for the VEP intermodulation components was analyzed using the two-sinusoid approach. This resulted in the selection of a full-wave rectifier for the nonlinearity in the model and determination of the forms of the transfer functions (Chapter 3).

2. In order to search for the transfer functions for the sandwich model, ten normal subjects data were analyzed. We found, to fit the VEP sum and difference frequency components measured from those subjects, the first linear element H_1 must be a *non-minimum* phase function with zeros in the right side of the s-plane. The amplitude characteristic of H_1 is a bandpass filter with a peak around 20 Hz, and the phase characteristic of H_1 possesses the feature that its slope becomes steeper as the frequency increases in the region above 15 Hz (Subsection 3.3.1). This finding does not match with previous investigations of the temporal characteristics of the visual system, which showed that ganglion cells in the retina and the linear processing stages in the VEP pathways can be characterized by *minimum* phase functions (Subsection 3.3.2).

3. Further investigation was done by performing the experiment of two-sinusoidal stimulation with different separation within the stimulus frequency pairs on two subjects. This work showed that the VEP phase response of the difference frequency component did not simply result from the classic linear-static nonlinear-linear process (Subsection 3.3.2).

4. Based on the previous studies of temporal behaviors of single cells and large populations of neurons, two inhibitory phenomena–contrast gain control and lateral interaction are thought to be involved in VEP generation. These two

phenomena may reflect a single nonlinear mechanism that is distinct from the static nonlinearity in the visual system. Their effects in the VEP responses were demonstrated by experiments conducted. The effect of contrast gain control was demonstrated using the two-sinusoid stimulation with different contrast levels (Section 4.2). The effect of lateral interaction was demonstrated using three-sinusoid stimulation introduced during the current investigation (Section 4.3). The inhibitory processes modify the signal transfer character in the visual system, and they can be qualitatively explained by a neural shunting inhibition model (Section 4.4).

5. A VEP model was extended from the sandwich system with the hypothesis that contrast gain control and lateral interactions modify the forward-through signal in the cortex (Subsection 5.1.1). These two inhibitory mechanisms are represented by an element in parallel with the sandwich system that produces a signal to control the parameters of the second filter H_2 in the sandwich system (Figure 5.2).

6. Model parameter estimation and validation were carried out for two individual subjects to obtain a system identification method.

7. In the first model (frequency response model), the parameter dependence on the inhibitory signal is defined for frequency domain operation (Subsection 5.1.3). The inhibitory signal is constant in steady-state for a given stimulus, but varies as the stimulus frequency changes. Parameter estimation was guided by the VEP sum and difference frequency components using a least-square fitting method (section 5.3). Model fitting quality was verified by "lack of fit" examination (Subsection 5.4.1). Model prediction ability in the frequency domain was examined for single sinusoid stimulation (Subsection (5.4.2). The model's response curve essentially matched the VEP's. Since the parameter control by the inhibitory signal is defined in steady-state operation, the frequency response model is not able to describe the visual system's dynamics in the time domain.

8. The second model (dynamic model) is developed in such a way that the model structure and all the linear elements identified in the first model are kept unchanged, and the parameter dependence on the inhibitory signal is defined in time course instead of steady-state operation (Section 6.1). Parameter estimation was guided by the VEP transient response elicited by a square-wave contrast reversing pattern (Section 6.4). Model prediction in the frequency domain was examined for two-sinusoid stimulation (Section 6.5). Some agreement in response curve shapes can be observed in the frequency region above 5 Hz for difference frequency components and above 8 Hz for sum frequency components. However, the dynamic model does not provide a good fit for the values of the steady-state VEP data (Figure 6.7).

In summary, The present research on the human visual system relates to two aspects. The first one is the study of evoked potential methods and experimental work in order to obtain an understanding of the mechanisms responsible for the generation of evoked potentials in biophysical terms. The second one is system modeling in order to transform the evoked potential methodology from an empirical phenomenology into a quantitative subject of research. We introduced system identification procedures and performed these procedures for two individual subjects to drive a protocol of VEP modeling.

The major contributions of this work include:

1. Proposed a VEP model structure based on the sandwich system with consideration of incorporating the nonlinear contrast gain control and lateral interaction mechanisms. This extended model enables the analysis of separate inhibitory and excitatory processes and their interactions.

2. Introduced a mathematical equations and method to describe and identify the model with the consideration of both frequency and time domain prediction.

7.2 Discussion

In this research, two models were proposed. The second one was developed from the first one in an attempt to extend the model from a description in the frequency domain to one in the time domain. As mentioned in Section 5.4, for a nonlinear physiological system, generally a model can only describe the system responses corresponding to some particular inputs, it cannot describe the actual system's behavior for any input. "The real-life actual system is an object of a different kind than our mathematical models. In a sense, there is an impenetrable but transparent screen between our word of mathematical descriptions and the real word. We can look through this window and compare certain aspects of the physical system with its mathematical description, but we can never establish any exact connection between them" (Ljung, 1987). For a set of given stimuli, for instance in our system modeling with two superimposed sinusoids and a square-wave function, a model capable of fitting the response corresponding to one type of stimulation is not guaranteed to fit the response corresponding to another type of stimulation. System modeling, nevertheless, is aimed to elaborate a mathematical form that can describe the physical system's behavior in as large a range as possible. The current work is indeed an attempt to achieve this goal. In the steady-state case, one can imagine the visual neural mechanisms may have similar reactions to both two-sinusoid and single sinusoid stimuli, particularly when the frequencies of the two sinusoids are close together. However, a square-wave function contains a wide range of frequency components. Reactions of neural mechanisms to the square-wave input may significantly differ from the reactions to the two-sinusoid input. Naturally, it is more difficult for the model to predict the responses in both the frequency and time domain than to predict the responses of different stimuli in the same frequency domain. As a result, the dynamic model gains an ability to describe the transient behavior of the real system, but loses its prediction power in the frequency region. Based on the above discussion, we prefer to accept the model guided by "usefulness" rather than "truth." From this point, Both the frequency response model and the dynamic model should have their specific application range.

7.3 Topics for Future Research

The current work also exposed some problems that may lead to further visual evoked potential research.

I. The source of the contrast gain control in the cortex

The experiment in Chapter 3 elucidated how the contrast mechanism affects the direct-through signals in the cortex. However, the source of this contrast signal remains in question. There are three likely possibilities: i) The signals directly come from an early stage, which forms a forward inhibitory structure. ii) The signals come from a later stage, which forms a feedback inhibitory structure. iii) They simply come from direct-through signals themselves, which forms a self inhibitory structure. Because visual evoked potentials combine the activities of many neural mechanisms, there is little hope to obtain a clear picture about the structure of this contrast mechanism through VEP analysis. This problem is expected to be solved by physiological and anatomical studies in the future.

II. Subsystems of inhibitory process in the cortex

The parameter control in the model is represented by a phase modulator and a magnitude modulator. One of the reasons for such a treatment is that a sufficient background is lacking about cellular connections that relate to the inhibitory process in the cortex. If the cellular structure responsible for those inhibitory processes is clarified, and further the network inhibitory behavior is properly represented by some functional blocks according to the neural connecting structure, the resultant model may possess more physiological sense and predictive power.

III. Model application extension in other aspects

The models proposed in this work were developed, tested and validated under certain conditions. As a next step, extension of the model conditions can be considered, which refers to the following subjects:

i). *Model response as a function of stimulus contrast*

In either the frequency response model or the dynamic model, the luminance modulation depth of the stimuli was fixed in order to get rid of the effect caused by the

contrast gain control in the retina. This limitation can be removed if the properties of this contrast mechanism is considered in the model. In fact, Victor has proposed a model for the cats' X type cells in the retina (Victor, 1987), which included the effect of this mechanism. This single-cell model may serve as a reference for fulfilling the objective.

ii). *Model response as a function of spatial variables*

If a dartboard or a checkboard pattern stimulus with variable-size segments is used in VEP studies, lateral interaction across the areas of different size may be investigated and further described in the model. In this case, VEP responses are not only a function of time, but also a function of one- or two-dimensional special variables.

The above topics may be considered with regard to both microphysiological and global neural network investigations. We expect any progress in these fields will enhance the knowledge of visual neural physiology and perception.

Finally, we want to expand the current work to the clinical field. In the current studies, the model identification procedure was demonstrated for two subjects. The model parameters listed in Table 4 and Table 5 can supply a reference of initial value selection for further model identification. If this procedure is carried out over a large sample of the population, the model parameters can be statistically analyzed. The statistical parameters, such as mean value, variance, etc., may serve as a standard for clinics to analyze disease states and deficits associated with the visual neural pathways. The parameter estimation routine (VEP data measuring, processing and curve fitting) and equipment used in this research are also accessible to the general clinic.

APPENDIX A

A-I Intermodulation Components from an Asymmetrical Rectifier

An asymmetrical rectifier $N(v)$ can be expanded in a series

$$N(v) = \sum_{k=0}^{\infty} a_k v^k = \sum_{k=0}^{\infty} a_{2k} v^{2k} + \sum_{k=0}^{\infty} a_{2k+1} v^{2k+1} \qquad (A.1)$$

by least-square fitting approach. The first term of the right side of (A.1) is the even portion of the rectifier, the second term is the odd portion of the rectifier. Now we want to prove, for two-sinusoid input

$$v(t) = A_1 \sin \omega_1 t + A_2 \sin \omega_2 t \qquad (A.2)$$

that the odd portion will not produce sum and difference frequency component. The proof is divided in three steps.

1. When $k = 3$,

$$v^3(t) = (A_1 \sin \omega_1 t + A_2 \sin \omega_2 t)^3$$

$$= A_1^3 \sin^3 \omega_1 t + 3A_1^2 A_2 \sin^2 \omega_1 t \sin \omega_2 t + 3A_1 A_2^2 \sin \omega_1 t \sin^2 \omega_2 t + A_2^3 \sin^3 \omega_2 t$$

$$= A_1^3 \sin^3 \omega_1 t + \frac{3}{2} A_1^2 A_2 \sin \omega_2 t - \frac{3}{4} A_1^2 A_2 [\sin(\omega_2 - 2\omega_1)t + \sin(\omega_2 + 2\omega_1)t]$$

$$-\frac{3}{4} A_1 A_2^2 [\sin(\omega_1 - 2\omega_2)t + \sin(\omega_1 + 2\omega_2)t] + \frac{3}{2} A_1 A_2^2 \sin \omega_1 t + A_2^3 \sin^3 \omega_2 t \qquad (A.3)$$

It is seen, $v^3(t)$ does not contain even order frequency components*.

2. Suppose that, when $k = r$ (r is an odd integer), $v^r(t)$ does not contain even order frequency components.

3. When $k = r + 2$,

$$\begin{aligned} v^{r+2}(t) &= v^r(t) v^2(t) \\ &= v^r(t) \{ \frac{1}{2}(A_1^2 + A_2^2) - \frac{1}{2} A_1^2 \cos 2\omega_1 t - \frac{1}{2} A_2^2 \cos 2\omega_2 t \\ &+ A_1 A_2 [\cos(\omega_1 - \omega_2)t - \cos(\omega_1 + \omega_2)t] \} \end{aligned} \qquad (A.4)$$

*The even order frequency components is referred to the components at frequencies $n\omega_1 \pm m\omega_2$ (n, m=0, 1, 2, $\cdots$, and $n + m$ is an even integer.)

All the terms in the brackets are even order frequency components, and according to the assumption that $v^r(t)$ only contains odd order frequency components, therefore, $v^{r+2}(t)$ does not contain even order frequency components, including sum and difference frequency components.

(end of proof)

A-II Intermodulation Components from the Full-Wave Rectifier

For two-sinusoid input applying to the rectifier

$$v(t) = A_1 \sin(\omega_1 t + \phi_1) + A_2 \sin(\omega_2 t + \phi_2) \tag{A.5}$$

to obtain the amplitude of DFC and SFC, we expand the rectifier $N(v)$ into a six degree series by least square approximation:

$$N(v) \approx \sum_{k=1}^{6} a_k v^k \tag{A.6}$$

If $N(v)$ is a full wave rectifier, only even order terms exist in the series. the second term

$$\begin{aligned}
v^2(t) &= [A_1 \sin(\omega_1 t + \phi_1) + A_2 \sin(\omega_2 t + \phi_2)]^2 \\
&= A_1^2 \sin^2(\omega_1 t + \phi_1) + A_2^2 \sin^2(\omega_2 t + \phi_2) + 2A_1 A_2 \sin(\omega_1 t + \phi_1) \sin(\omega_2 t + \phi_2) \\
&= A_1^2 \sin^2(\omega_1 t + \phi_1) + A_2^2 \sin^2(\omega_2 t + \phi_2) \\
&+ A_1 A_2 \{\cos[(\omega_1 - \omega_2)t + \phi_1 - \phi_2] - \cos[(\omega_1 + \omega_2)t + \phi_1 + \phi_2]\} \\
&= A_1^2 \sin^2(\omega_1 t + \phi_1) + A_2^2 \sin^2(\omega_2 t + \phi_2) \\
&+ A_1 A_2 \{\sin[(\omega_1 - \omega_2)t + \phi_1 - \phi_2 + \frac{\pi}{2}] \\
&+ \sin[(\omega_1 + \omega_2)t + \phi_1 + \phi_2 - \frac{\pi}{2}]\}
\end{aligned} \tag{A.7a}$$

It is seen, the amplitude of DFC and SFC produced by the second term is $A_1 A_2$. By further calculation, one can show that the amplitudes of DFC or SFC produced by

the fourth term and sixth term are also equal, they are:

$$\text{amplitude of fourth term:} \qquad \frac{3}{2}(A_1^3 A_2 + A_1 A_2^3) \tag{A.7b}$$

$$\text{amplitude of sixth term:} \qquad \frac{15}{8}(A_1^5 A_2 + A_1^3 A_2^3 + A_1 A_2^5) \tag{A.7c}$$

The amplitude of DFC or SFC produced from the rectifier then can be expressed by:

$$\begin{aligned} & A_{zDFC}(f_1, f_2) = A_{zSFC}(f_1, f_2) \approx \\ & \approx a_2 A_1 A_2 + \frac{3}{2} a_4 (A_1^3 A_2 + A_1 A_2^3) + \frac{15}{8} a_6 (A_1^5 A_2 + A_1^3 A_2^3 + A_1 A_2^5) \end{aligned} \tag{A.8}$$

Next, considering the approximation (A.6) only valid when the value of input v is within a specific range (in this work, $|v| \leq 1$ for $a_0 = 0.085$, $a_2 = 2.307$, $a_4 = -2.820$ and $a_6 = 1.466$), expression (A.8) therefore should be normalized. The input $v(t)$ can be rewritten as

$$\begin{aligned} v(t) &= (A_1 + A_2)\left[\frac{A_1}{A_1 + A_2}\sin(\omega_1 t + \phi_1) + \frac{A_2}{A_1 + A_2}\sin(\omega_2 t + \phi_2)\right] \\ &= (A_1 + A_2) v'(t) \end{aligned} \tag{A.9}$$

where $v'(t)$ is also a two-sinusoid function with amplitudes $A_1/(A_1+A_2)$ and $A_2/(A_1+A_2)$. Now the output of the rectifier

$$\begin{aligned} z(t) = N[v(t)] = |v(t)| = |(A_1 + A_2) v'(t)| \\ = (A_1 + A_2)|v'(t)| = (A_1 + A_2) N[v'(t)] \end{aligned} \tag{A.10}$$

We denote the amplitude of DFC, produced from the rectifier due to input $v'(t)$, as $A'_{zDFC}(f_1, f_2)$. Because $|v'(t)| \leq 1$, $A'_{zDFC}(f_1, f_2)$ can be obtained from (A.8) by substitution of A_1 and A_2 by $A_1/(A_1+A_2)$ and $A_2/(A_1+A_2)$ respectively. This gives

$$\begin{aligned} A'_{zDFC}(f_1, f_2) \approx\ & a_2 \left(\frac{A_1}{A_1 + A_2}\right)\left(\frac{A_2}{A_1 + A_2}\right) + \frac{3}{2} a_4 \left[\left(\frac{A_1}{A_1 + A_2}\right)^3 \left(\frac{A_2}{A_1 + A_2}\right) + \right. \\ & + \left. \left(\frac{A_1}{A_1 + A_2}\right)\left(\frac{A_2}{A_1 + A_2}\right)^3\right] + \frac{15}{8} a_6 \left[\left(\frac{A_1}{A_1 + A_2}\right)^5 \left(\frac{A_2}{A_1 + A_2}\right) + \right. \\ & + \left. 3\left(\frac{A_1}{A_1 + A_2}\right)^3 \left(\frac{A_2}{A_1 + A_2}\right)^3 + \left(\frac{A_1}{A_1 + A_2}\right)\left(\frac{A_2}{A_1 + A_2}\right)^5\right] \end{aligned} \tag{A.11}$$

The final expression is obtained by multiplying $A'_{zDFC}(f_1, f_2)$ by $(A_1 + A_2)$,

$$\begin{aligned} A_{zDFC}(f_1, f_2) &= (A_1 + A_2)A'_{zDFC}(f_1, f_2) \\ &\approx a_2 \frac{A_1 A_2}{A_1 + A_2} + \frac{3}{2} a_4 \frac{A_1^3 A_2 + A_1 A_2^3}{(A_1 + A_2)^3} + \frac{15}{8} a_6 \left[\frac{A_1^5 A_2 + 3A_1^3 A_2^3 + A_1 A_2^5}{(A_1 + A_2)^5} \right] \end{aligned} \quad \text{(A.12)}$$

That is the result of equation (3.4).

APPENDIX B

B-I Confidence Limit for VEP Response Description

In Chapter 3, we examined the VEP sum and difference frequency components recorded from ten subjects. We gave a description for those responses based on most of the subjects' data. In the worst case, that is the ratio of sum and difference frequency components, there are two subjects' response curves differing from the description. In terms of those observations, now we must give a confidence limit that the description we have given is correct for large number of populations.

Assume that the a response curve (amplitude or phase of DFC or SFC) satisfies binomial distribution, that is, the probability that the response curve satisfies the given description is p, and fails to satisfy the description is $1-p$. The probability that r successful responses out of n observations is given by

$$P(r) = \frac{n!}{r!(n-r)!} p^r (1-p)^{n-r} \qquad (B.1)$$

Now if r and n are given, and p is unknown, the probability (confidence level) that p is within some particular range Φ $(0 \leq \Phi \leq 1)$ is given by the ratio of integrals

$$P\{p \in \Phi\} = \frac{\int_{p\in\Phi} \frac{n!}{r!(n-r)!} p^r (1-p)^{n-r} dp}{\int_0^1 \frac{n!}{r!(n-r)!} p^r (1-p)^{n-r} dp} = \frac{\int_{p\in\Phi} p^r (1-p)^{n-r} dp}{\int_0^1 p^r (1-p)^{n-r} dp} \qquad (B.2)$$

In our VEP observation that $r = 8$ and $n = 10$, if we want to obtain 95% confidence that p is greater than a value p_{cri}, it requires

$$95\% = \frac{\int_{p_{cri}}^1 p^8 (1-p)^{10-8} dp}{\int_0^1 p^8 (1-p)^{10-8} dp} \qquad (B.3)$$

Solving equation (B.3) yields $p_{cri} = 0.53$, which means that we have 95% confidence that at least 53% of the population's VEPs satisfy the description given in Chapter 3.

Table 7. VEP noise errors and model errors.

Subject A DFC Real Part Errors									
point i	$(Y_{ij}-\overline{Y}_i)^2$				$\sum(Y_{ij}-\overline{Y}_i)^2$	$4(\hat{Y}_i-\overline{Y}_i)^2$	W_i	$\sum W_i(Y_{ij}-\overline{Y}_i)^2$	$4W_i(\hat{Y}_i-\overline{Y}_i)^2$
1	0.0018	0.0076	0.0596	0.0397	0.1087	0.0329	3.7682	0.4096	0.1241
2	0.1277	0.0015	0.8234	0.3470	1.2996	0.0845	1.3962	1.8145	0.9557
3	0.0167	0.0107	0.0218	0.0147	0.0639	0.0890	1.9093	0.1220	0.1698
4	0.0653	0.3952	0.1282	0.0002	0.5889	0.0002	3.9243	2.3111	0.0008
5	0.0987	0.0023	0.8477	0.4279	1.3765	0.0044	2.9741	4.0939	0.0130
6	0.2693	0.0721	0.0024	0.0405	0.3843	0.1639	4.8152	1.8507	0.7894
7	0.0004	0.2735	0.0595	0.0675	0.4009	0.1251	5.0669	2.0313	0.6339
8	0.0236	0.0630	0.1520	0.0002	0.2388	2.1534	5.0336	1.2021	10.839
$\sum$								13.835	13.526

Subject A DFC Imaginary Part Errors									
point i	$(Y_{ij}-\overline{Y}_i)^2$				$\sum(Y_{ij}-\overline{Y}_i)^2$	$4(\hat{Y}_i-\overline{Y}_i)^2$	W_i	$\sum W_i(Y_{ij}-\overline{Y}_i)^2$	$4W_i(\hat{Y}_i-\overline{Y}_i)^2$
1	0.0543	0.0386	0.0094	0.0177	0.1199	0.0072	3.7682	0.4520	0.0271
2	0.1426	0.1253	0.0044	0.6365	0.9076	0.5175	1.3962	1.2672	0.7226
3	0.4618	0.2511	0.0867	0.2235	1.0232	0.0366	1.9093	1.9536	0.0698
4	0.0073	0.0664	0.1288	0.0349	0.2374	0.2833	3.9243	0.9317	1.1119
5	0.5214	0.7329	0.6938	0.5553	2.5034	0.1544	2.9741	7.4454	0.4593
6	0.6951	0.0423	0.1392	1.0022	1.8789	0.1083	4.8152	9.0473	0.5217
7	0.2475	0.1931	0.6106	0.0242	1.0754	0.0192	5.0669	5.4488	0.0973
8	0.0235	0.5706	0.0479	0.1467	0.7888	0.0175	5.0336	3.9705	0.0881
$\sum$								30.516	3.0978

Subject A SFC Real Part Errors									
point i	$(Y_{ij}-\overline{Y}_i)^2$				$\sum(Y_{ij}-\overline{Y}_i)^2$	$4(\hat{Y}_i-\overline{Y}_i)^2$	W_i	$\sum W_i(Y_{ij}-\overline{Y}_i)^2$	$4W_i(\hat{Y}_i-\overline{Y}_i)^2$
1	0.1610	0.1960	0.2163	0.1592	0.7325	0.0990	4.1519	3.0413	0.4109
2	0.0328	0.0356	0.0232	0.0343	0.1258	0.2410	11.956	1.5044	2.8815
3	0.0340	0.1118	0.3879	0.3340	0.8677	0.0159	2.8520	2.4745	0.0454
4	0.0097	0.0061	0.0044	0.0222	0.0423	0.0095	3.8417	0.1626	0.0366
5	0.0194	0.0211	0.0248	0.0176	0.0829	0.0088	1.8568	0.1538	0.0163
$\sum$								7.3366	3.3907

Subject A SFC Imaginary Part Errors									
point i	$(Y_{ij}-\overline{Y}_i)^2$				$\sum(Y_{ij}-\overline{Y}_i)^2$	$4(\hat{Y}_i-\overline{Y}_i)^2$	W_i	$\sum W_i(Y_{ij}-\overline{Y}_i)^2$	$4W_i(\hat{Y}_i-\overline{Y}_i)^2$
1	0.3616	0.3237	0.3236	0.3618	1.3707	0.0464	4.1519	5.6910	0.1928
2	1.0242	1.0378	1.0228	0.9960	4.0808	0.0078	11.956	48.789	0.0937
3	0.4679	0.4008	0.4090	0.4558	1.7336	0.2558	2.8520	4.8644	0.7296
4	0.2863	0.3172	0.2935	0.3692	1.2662	0.0069	3.8417	4.8644	0.0264
5	0.0088	0.0090	0.0128	0.0113	0.0419	0.0522	1.8568	0.0778	0.0969
$\sum$								64.366	1.1394

Table 7. VEP noise errors and model errors (continued).

Subject B DFC Real Part Errors									
point i	$(Y_{ij}-\overline{Y}_i)^2$				$\sum(Y_{ij}-\overline{Y}_i)^2$	$4(\hat{Y}_i-\overline{Y}_i)^2$	W_i	$\sum W_i(Y_{ij}-\overline{Y}_i)^2$	$4W_i(\hat{Y}_i-\overline{Y}_i)^2$
1	0.0670	0.1389	0.1161	0.0845	0.4066	0.0638	1.8665	0.7589	0.1190
2	0.0008	0.5065	0.1924	0.0598	0.7595	0.1461	1.9559	1.4851	0.2857
3	0.0586	0.1197	0.1192	0.0590	0.3565	0.0062	3.7940	1.3525	0.0236
4	0.1000	0.0751	0.2442	0.2878	0.7070	0.0822	4.7154	3.3340	0.3874
5	0.1627	0.0016	0.1037	0.1489	0.2829	0.2827	3.3134	0.9374	0.9300
6	0.1517	0.0737	0.1714	0.0610	0.4577	0.0161	3.3285	1.5234	0.0535
7	0.2074	0.0110	0.0001	0.3230	0.5414	0.0124	5.6833	3.0772	0.0702
8	0.0179	0.0009	0.0009	0.0054	0.0250	0.3299	5.0823	0.1273	1.6766
$\sum$								12.596	3.5460

Subject B DFC Imaginary Part Errors									
point i	$(Y_{ij}-\overline{Y}_i)^2$				$\sum(Y_{ij}-\overline{Y}_i)^2$	$4(\hat{Y}_i-\overline{Y}_i)^2$	W_i	$\sum W_i(Y_{ij}-\overline{Y}_i)^2$	$4W_i(\hat{Y}_i-\overline{Y}_i)^2$
1	0.5923	0.1011	0.2566	0.0030	0.9530	0.0099	1.8665	1.7787	0.0186
2	0.0155	0.5145	0.0064	0.2629	0.7993	0.1925	1.9559	1.5634	0.3765
3	0.0544	0.0383	0.1159	0.1428	0.3514	0.0040	3.7940	1.3332	0.0151
4	0.0003	0.2879	0.0002	0.2926	0.5810	0.7599	4.7154	2.7398	3.5831
5	0.8999	0.0829	0.7906	0.1207	1.8941	0.0283	3.3134	6.2758	0.0937
6	1.3439	0.5030	2.1116	0.1725	4.1311	0.0116	3.3285	13.750	0.0388
7	0.0655	0.1959	0.0600	0.0034	0.3248	0.0036	5.6833	1.8457	0.0206
8	0.0551	0.1533	0.1096	0.0872	0.4052	0.0194	5.0823	2.0592	0.0987
$\sum$								31.356	4.2451

Subject B SFC Real Part Errors									
point i	$(Y_{ij}-\overline{Y}_i)^2$				$\sum(Y_{ij}-\overline{Y}_i)^2$	$4(\hat{Y}_i-\overline{Y}_i)^2$	W_i	$\sum W_i(Y_{ij}-\overline{Y}_i)^2$	$4W_i(\hat{Y}_i-\overline{Y}_i)^2$
1	0.0004	0.1098	0.0127	0.0572	0.1801	0.0014	3.1612	0.5693	0.0045
2	0.0021	0.0877	0.0472	0.3131	0.4502	0.0000	4.3958	9.5824	0.0001
3	0.0035	0.0807	0.0040	0.0262	0.1144	0.2030	2.2544	0.2579	0.4575
4	0.1128	0.0125	0.1194	0.0104	0.2552	0.0044	3.2619	0.8324	0.0143
5	0.0000	0.0009	0.0072	0.0033	0.0113	0.0597	6.5829	0.0745	0.3928
$\sum$								11.316	0.8692

Subject B SFC Imaginary Part Errors									
point i	$(Y_{ij}-\overline{Y}_i)^2$				$\sum(Y_{ij}-\overline{Y}_i)^2$	$4(\hat{Y}_i-\overline{Y}_i)^2$	W_i	$\sum W_i(Y_{ij}-\overline{Y}_i)^2$	$4W_i(\hat{Y}_i-\overline{Y}_i)^2$
1	0.0383	0.0022	0.1454	0.0541	0.2400	0.0162	3.1612	0.7586	0.0513
2	0.0021	0.0182	0.0103	0.0796	0.1102	0.0005	4.3958	0.4737	0.0021
3	0.0547	0.0001	0.0016	0.0699	0.1263	0.0220	2.2544	0.2846	0.0497
4	0.0429	0.0172	0.0030	0.1545	0.2177	0.1329	3.2619	0.7100	0.4334
5	0.0000	0.0037	0.0006	0.0075	0.0118	0.1485	6.5829	0.0776	0.9774
$\sum$								2.3045	1.5139

APPENDIX C

C-I The Second Harmonic from the Full-Wave Rectifier

If the rectifier characteristic is approximated by a six degree polynomial

$$N(v) = |v| \approx a_0 + a_2 v^2 + a_4 v^4 + a_6 v^6 \qquad \text{for } |v| \leq 1 \tag{D.1}$$

for a single sinusoid input

$$v(t) = A\sin(\omega t + \phi) \tag{D.2}$$

we have

$$N(v) = N[A\sin(\omega t + \phi)] = AN[\sin(\omega t + \phi)] \tag{D.3}$$

The second term of (D.1) is

$$[\sin(\omega t + \phi)]^2 = \frac{1}{2}[1 - \cos(2\omega t + 2\phi)] = \frac{1}{2} + \frac{1}{2}\sin(2\omega t + 2\phi - \frac{\pi}{2}) \tag{D.4}$$

It is seen, the second harmonic produced by the second term is $\frac{1}{2}\sin(2\omega t + 2\phi - \frac{\pi}{2})$. By further calculation, the second harmonic produced by the fourth and sixth terms are $\frac{1}{2}\sin(2\omega t + 2\phi - \frac{\pi}{2})$ and $\frac{15}{32}\sin(2\omega t + 2\phi - \frac{\pi}{2})$ respectively. Therefore, the amplitude of the second harmonic produced from the rectifier,

$$A_z(2f) = A(\frac{1}{2}a_2 + \frac{1}{2}a_4 + \frac{15}{32}a_6) \tag{D.5}$$

The phase of the second harmonic produced from the rectifier,

$$\phi_z(2f) = 2\phi - \frac{\pi}{2} \tag{D.6}$$

Equations (5.35) and (5.36) hence are proved.

C-II Root Mean Squared Magnitude of Square-Wave Input

Suppose the two-sinusoidal input

$$s_{(sin)}(t) = C_{w(sin)}(\sin\omega_1 t + \sin\omega_2 t) \tag{D.7}$$

and the square wave input

$$s_{(squ)}(t) = \begin{cases} C_{w(squ)} & nT < t \leq (n+1/2)T \\ -C_{w(squ)} & (n+1/2)T < t \leq (n+1)T \end{cases} \quad n = 0, 1, 2, \ldots \qquad (D.8)$$

Both signals possessing equivalent modulation depth in root-mean square sense gives an equality

$$\sqrt{C^2_{w(sin)} + C^2_{w(sin)}}/\sqrt{2} = \lim_{\tau \to \infty} \sqrt{\frac{1}{\tau} \int_0^\tau s^2_{(squ)}(t)dt} = C_{w(sqy)} \qquad \text{(D.9a)}$$

$$\text{or} \qquad C_{w(sin)} = C_{w(squ)} \qquad \text{(D.9b)}$$

REFERENCES

Asselman, P., D. W. Chadwick, and C. D. Marsden. 1975. "Visual Evoked Responses in the Diagnosis and Management of Patients Suspected of Multiple sclerosis." *Brain.* 98: 261–282.

Barlow, H. B. 1969. "Trigger Features, Adaptation and Economy of Impulses." *Information Processing in the Nervous System.* Ed. Leibovic, K. N. New York: Springer Verlar.

Barlow, J. S. 1957. "An Electronic Method for Detecting Evoked Responses of the Brain and for Reproducing Their Average Waveforms," *Electroenceph. Clin. Neurophysiol.* 9: 340–343.

Bartley, S. H., and G. H. Bishop. 1933. "The Cortical Response to Stimulation of the Optic Nerve in the Rabbit." *Am. Journal of Physiology.* 133: 159–172.

Berson, E. L. 1975. "Electrical Phenomena in the Retina," *Adler's Physiology of the Eye.* Ed. Moses. R. A. 6th Edition. St. Louis, Montana: The C. V. Mosky Company. 453–493.

Benerento, L. A.. O. D. Creutzfeldt, and U. Kuhnt. 1972. "Significance of Intracortical Inhibition in the Visual Cortex." *Natual New Biol.* 238: 124–126.

Blakemore, C. B. and F. Vital-Durand. 1981. "Distribution of X- and Y-Cells in the Monkey's Lateral Geniculate Nucleus." *Journal of Physiology.* 320: 179–189.

Bode, H. W. 1945. Network Analysis and Feedback Amplifier Design. Princeton, New Jersey: D. Van Nostrand Co., Inc.

Bodis–Wollner, I., and M. Onofrj. 1982. "System Diseases and Visual Evoked Potential Diagnosis in Neurology." *Changes Due to Synaptic Malfunction.* Ann. N.Y. Acad. Sci. 388: 327–348.

Caceci, M., and W. Cacheris. 1984. "Fitting Curve to Data," *BYTE.* 5: 340–362.

Cobb, W., and C. Morocutti. 1967. "The Evoked Potentials," *Electroenceph. Clin. Neurophysiol.* 26: 218.

Cohen, A. H. 1975. "The Retina and Optic Nerve." *Adler's Physiology of the Eye.* Ed. Moses. R. A.. 6th Edition. St. Louis, Montana: The C. V. Mosky Company. 367–405.

REFERENCES
(Continued)

Creutzfeldt, O. D., A. Rosina, M. Ito, and W. Probst. 1969. "Visual Evoked Response of Single Cells and of the EEG in Primary Visual Area of the Cat." *Journal of Neurophysiology.* 32: 127–139.

Creutzfeldt, O. D., and U. Kuhnt. 1973. "Electrophysiology and Topographical Distribution of Visual Evoked Potentials in Animals." *Handbook of Sensory Physiology* Vol. 7, Part 3. Ed. Jung, R. Berlin: Springer Verlar.

Creutzfeldt, O. D., U. Kuhnt, and L. A. Benevento. 1974. "An Intracellular Analysis of Visual Cortical Neurons to Moving Stimuli: Responses in a Cooperative Neuronal Network." *Exp. Brain Res.* 21: 251–274.

Davis, O. L. and P. L. Goldsmith. 1972. Statistical Method in Research and Production. New York: Hatner Publishing Co., Inc.

Dawson, G. D. 1947. "Cerebral Responses to Electrical Stimulation of Peripheral Nerve in Man." *J. Neurol. Neurolsurg. Psychiat.* 10: 141–162.

———. 1950. "Human Cortical Responses to Stimulation of Peripheral Nerves." *Brit. Med. Bull.* 6: 326–329.

De Monasterio, F. M. and P. Gouras. 1975. "Functional Properties of Ganglion Cells of the Rhesus Monkey Retina." *Journal of Physiology.* 251: 167–195.

Eccles, J. C. 1951. "Interpretation of Action Potentials Evoked in the Cerebral Cortex." *EEG Clin. Neurophysiology.* 3: 449–464.

———. 1961. "The Synaptic Mechanism for Postsynaptic Inhibition." *Nervous Inhibition.* Ed. Florey, E. New York: Pergamon Press Ltd.

Elul, R. 1969. "Ganssian Behavior of the Electroencephalogram: Changes During Performance of Mental Task." *Science.* 164: 328–331.

Enroth-Cugell, C., and J. G. Robson. 1966. "The Contrast Sensitivity of Retinal Ganglion Cells of the Cat." *Journal of Physiology.* 187: 517–552.

Furman, G. G. 1965. "Comparison of Models for Subtractive and Shunting Lateral-Inhibition in Receptor-Neuron Fields." *Bant 2, Heft 6, 10.*

REFERENCES
(Continued)

Gradshteyn, I. S. and I. M. Ryzhik. 1980. Table of Integrals, Series, and Products. San Diego, CA: Academic Press, Inc.

Halliday, A. M., W. I. McDonals, and J. Mushin. 1973a. "Visual Evoked Response in Diagnosis of Multiple Sclerosis." *Br. Med. J.* 4: 661–664.

———. 1973b. "Delayed Pattern-Evoked Response in Optic Neuritis in Relation to Visual Acuity." *Trans. Ophthalmol. Soc. U. K.* 93: 315–324.

Hart, W. M. Ed. 1992. Adler's Physiology of the Eye. 9th Edition. St. Louis, Montana: Mosby-Year Book, Inc.

Heckenlively, J. R. and G. B. Arden. Eds. 1991. Principles and Practice of Clinical Electrophysiology of Vision. St. Louis, Montana: Mosby-Year Book, Inc.

Hubel, D. H., and T. N. Wiesel. 1962. "Receptive Fields, Binocular Interaction, and Functional Architecture in the Cat's Visual Cortex." *Journal of Physiology.* 169: 106–154.

———. 1968. "Receptive Fields and Functional Architecture of Monkey Striate Cortex." *Journal of Physiology.* 195: 215–243.

Jasper, H. H. 1958."The 10-20 Electrode System of the International Federation." *Journal of Electroencephalography and Clinical Neurophysiology.* 10: 371–375.

Kandel, E. R., J. H. Schwartz and T. M. Jessell. Eds. 1991. Principles of Neural Science. 3rd Edition. Norwalk, Conn.: Appleton and Lange.

Kaplan, E., and R. Shaplep. 1982. "X and Y Cells in the Lateral Geniculate Nucleus of Macaque Monkeys." *J. of Physiology.* 330: 125–143.

Kim, Y. C., W. F. Wang, E. J. Powers, and J. R. Roth. 1979. "Extension of the Coherence Function to Quadratic Models." *Proc. IEEE.* 67: 428–429.

Kolb, H., E. V. Famiglietti, and R. Nelson. 1976. "Neural Connections in the Inner Plexiform Layer of the Cat's Retina." *The Structure of the Eye III.* Eds. Yamada, E., and S. Mishims. Tokyo: The Japan Journal of Ophthalmology. 319–332.

REFERENCES
(Continued)

Krnjevic, K., and S. Schwartz. 1967. "The Action of γ-Aminobutyric Acid on Cortical Neurons." *Exp. Brain Res.* 3: 272–283.

Kuffler, S. W. 1952. "Neurons in the Retina: Organization, Inhibition and Excitation Problems." *Cold Spring Harbor Symposium on Quantitative Biology.* 17: 281–292.

———. 1953. "Discharge Patterns and Functional Organization of Mammalian Retina." *Journal of Neurophysiology.* 16: 37–68.

Kuffler, S. W., and J. G. Nicholls. 1976. From Neuron to Brain. Mass.: Sinauer Associates.

Lee, B. B., J. Pokorny, V. C. Smith, P. R. Martin, and A. Valberg. 1990. "Luminance and Chromatic Modulation Sensitivity of Macaque Ganglion Cells and Human Observers." *J. Opt. Sco. Am. A.* 7: 2223–2236.

Lee, Y. W., and M. Schetzen. 1961. "Measurement of the Kernels of a Nonlinear System by Cross Correlation." *Mass. Inst. Tech. Res. Lab. Electron. Quart. Progr. Report.* 60: 118–130.

Lettvin, J. Y. 1962. "Form-Function Relations in Neurons." *Mass. Inst. Tech. Res. Lab. Electron. Quart. Progr. Report.* 66,333: (15, July), 333–335.

Levick, W. R. 1975. "Form and Function of Cat Retina Ganglion Cells." *Nature, Lond..* 254: 659–662.

Livingstone, M. S. and D. Hubel. 1988. "Segregation of Form, Color, Movement, and Depth: Anatomy, Physiology, and Perception." *Science.* 240: 740–749.

Ljung, L. 1987. System Identification: Theory for the User. New Jersey: Prentice-Hall. Inc.

Lopes Da Silva F. H. 1970. "Dynamic Characteristics of Visual Evoked Potentials." *Ph.D. Dissertation.* University of Utrecht.

Lund, J. S. "Orgnization of Neurons in the Visual Cortex, Area 17, of the Monkey (Macaca Mulatta)." *J. Comp. Neurol.* 147: 455–495.

REFERENCES
(Continued)

Maffei, L., and A. Fiorentini. 1973. "The Visual Cortex as a Spatial Frequency Analyser." *Vision Res.* 13: 1255–1267.

Marmarelis, P. Z., and V. Z. Marmarelis. 1978. Analysis Physiological Systems. New York: Plenum Press.

Masland, R. H. 1986. "The Functional Architecture of the Retina." *Scientific American.* 255: 102–112.

Mast, J. and J. D. Victor. 1991. "Fluctuations of Steady-State VEPs: Interactions of Driven Evoked Potentials and the EEG." *Electroencephalography and Clinical Neurophysiology.* 78: 389–401.

Myslobodsky, M. 1976. *Petit Mal Epilepsy.* New York: Academic Press.

Nabet, B., and R. B. Pinter. 1991. Sensory Neural Networks: Lateral Inhibition. Florida: CRC Press.

Pearlman, A. L. 1975. "Anatomy and Physiology of Central Visual Pathways." *Adler's Physiology of the Eye.* Ed. Moses, R. A. 6th Edition. St. Louis, Montana: The C.V. Mosky Co. 420–452.

Purpura, D. P. 1959. "Nature of Electrocortical Potentials and Synaptic Organizations in Cerebral and Cerebellar Cortex." *Int. Rev. Neurobiology.* 1: 147–163.

Purpura, K., D. Tranchina, E. Kaplan, and R. M. Shapley. 1990. "Light Adaptation in the Primate Retina: Analysis of Changes in Gain and Dynamics of Monkey Retinal Ganglion Cells." *Visual Neuroscience.* 4: 75–93.

Ratliff, F. 1965. Mach Bands: Quantitative Studies on Neural Networks in the Retina. San Francisco, CA: Holden-Day Inc.

Ratliff, F., and V. Zemon. 1984. " Visual Evoked Potentials Elicited in Normal Subjects and in Epileptic Patients by Windmill-Dart Board Stimuli." *Evoked Potentials II.* Eds. Nodar, R. H., and C. Barber. Boston, Mass.: Butterworth Publishers.

Regan, D. 1982. "Comparison of Transient and Steady-State Methods." *Ann. N.Y. Academy of Sciences.* 388: 45–71.

REFERENCES
(Continued)

Regan, D. 1989. Human Brain Electrophysiology: Evoked Potentials and Evoked Magnetic Fields in Science and Medicine. New York: Elsevier Science Publishing Co., Inc.

Shapley, R. M., and J. D. Victor. 1978. "The Effect of Contrast on the Transfer Properties of Cat Retina Ganglion Cells." *Journal of Physiology.* 285: 275–298.

———. "The Effect of Contrast on the Non-Linear Response of the Y Cell." *Journal of Physiology.* 302: 535–547.

Shapley, R. M., E. Kaplan, and R. Soodak. 1981. "Spatial Summation and Contrast Sensitivity of X & Y Cells in the Lateral Geniculate Nucleus of the Macaque Nature." *Journal of Physiology.* 292: 543–545.

Shapley, R. M. and J. D. Victor. 1981. "How the Contrast Gain Control Modifies the Frequency Response of Cat Retina Ganglion Cells." *Journal of Physiology.* 318: 161–179.

Shapley, R. M. 1982. "Parallel Pathways in the Mammalian Visual System." *Evoked Potential.* Ann. N.Y. Academy of science. 388: 11–20.

———. 1990. "Visual Sensitivity and Parallel Retinocortical Channels." *Annual Review of Psychology.* 41: 634–658.

So, Y. T. and R. M. Shapley. 1979. "Spatial Properties of X and Y Cells in the Lateral Geniculate Nucleus of the Cat and Conduction Velocities of Their Inputs" *Exp. Brain Research.* 36: 533–550.

Spekreijse, H. 1966. "Analysis of E.E.G. Responses in Man." *Ph.D. Dissertation.* University of Amsterdam.

Spekreijse, H., and H. Oosting. 1970. "Linearizing: a Method for Analyzing and Synthesizing Nonlinear System." *Kybernetik.* 7: 22–31.

Spekreijse, H., and D. Reits. 1982. "Squential Analysis of the Visual Evoked Potential System in Man; Nonlinear Analysis of a Sandwich System." *Evoked Potentials.* Ann. N.Y. Academy of Sciences. 388: 72–97.

REFERENCES
(Continued)

Spitzer, H., and S. Hochstein. 1985a. "Simple- and Complex-Cells Research Dependences on Stimulation Parameters." *Journal of Neurophysiology.* 53: 1244-1265.

———. 1985b. "A Complex-Cell Receptive-Field Model." *Journal of Neurophysiology.* 53: 1266-1286.

Tranchina, D., J. Gordon, R. M. Shapley, and J. Toyoda. 1981."Linear Information Processing in the Retina: A Study of Horizontal Cell Responses." Proc. *Natl. Acad. Sci.* 78: 6540-6542.

Trick, G. L. 1991. "Evoked Potentials in Alzheimer's Disease." *Principles and Practice of Clinical Electrophysiology of Vision.* Eds. Heckenlively, J. R. and G. B. Arden. St. Louis, Montana: Mosby-Year Book, Inc.

Victor, J. D. and R. M. Shapley. 1980. "A Method of Nonlinear Analysis in the Frequency Domain." *Biophys. J.* 29: 459-483.

Victor, J. D. 1981. "Nonlinear Interactions in the Cat Retina." *Theoretical Approaches in Neurobiology.* Eds. Reichardt, W. E., and T. Poggio. Mass.: The MIT Press. 49-59.

———. 1987. "The Dynamics of the Cat Retinal X Cell Centre." *Journal of Physiology.* 386: 219-246.

———. 1988. "The Dynamics of the Cat Retinal Y Cell Subunit" *Journal of Physiology.* 405: 289-320.

Victor, J. D., J. Mast. 1991. "A New Statistic for State-State Evoked Potentials." *Electroencephalography and Clinical Neurophysiology.* 78: 378-388.

Watanabs S., M. Konishi, and O. D. Creutzfeldt. 1966. "Postsynaptic Potentials in the Cat's Visual Cortex Following Electrical Stimulation of Afferent Pathways." *Exp. Brain. Res.* 1: 272-283.

Wiener, N. 1958. Nonlinear Problems in Random Theory. Mass: MIT Press, and New York: John Wiley.

REFERENCES
(Continued)

Zemon, V. 1984. "The VEP: Analysis of Functional Subsystems in the Brain." *Proc. of the IEEE, 6th Annual Conference of the Engineering in Medicine and Biology Society.* 9: 15–17.

Zemon, V., and F. Ratliff. 1984. "Intermodulation Components of the Visual Evoked Potential: Responses to Lateral and Superimposed Stimuli." *Biological Cybernetics.* 50: 401–408.

Zemon, V., M. Conte, L. Jindra, and J. Camisa. 1985. "Evoked Potential Estimates of Temporal Filters in the Human Visual System." *Proc. of the IEEE, 7th Annual Conference on Engineering in Medicine and Biology Society.* 9: 431–436.

Zemon, V., J. Victor. and F. Ratliff. 1986. "Functional Subsystems in the Visual Pathways of Humans Characterized Using Evoked Potentials." *Evoked Potentials.* Eds. Cracco, R. Q., and I. Bodis-Wollner. New York: Alan R. Liss, Inc. 203–210.

Zemon, V., E. Kaplan, and F. Ratliff. 1986. "The Role of GABA-Mediated Intracortical Inhibition in the Generation of Visual Evoked Potentials." *Evoked Potentials.* Eds. Cracco, R. Q., and I. Bodis-Wollner. New York: Alan R. Liss, Inc. 287–295.

Zemon, V., M. Conte, and J. Camisa. 1987. "Effects of Contrast on Temporal Filters in the Human Visual System." *Proc. of the IEEE, 9th Annual Conference of the Engineering in Medicine and Biology Society.* 11: 13–16.

Zemon, V., J. Gordon, and J. Welch. 1988. "Asymmetries in ON and OFF Visual Pathways of Humans Revealed Using Contrast-Evoked Cortical Potentials." *Visual Neuroscience.* 1: 145–150.